

THE FLORIDA STATE UNIVERSITY
COLLEGE OF ARTS AND SCIENCES

THE INFLUENCE OF THERMAL FRONTS UPON THE
SOLUTIONS OF AN ANALYTICAL MODEL OF A
MID-LATITUDE WAVE-CYCLONE

By
RICHARD GROTJAHN

A Dissertation submitted to
the Department of Meteorology
in partial fulfillment of the
requirements for the degree of
Doctor of Philosophy

Approved:

C. G. Leith

Professor co-directing Dissertation

James J. O'Brien

Professor co-directing Dissertation

Prof. Stynes

Albert I. Barilow

Albert I. Barilow

William Hunter

March, 1979

ABSTRACT

The stability and structure of wave-like perturbations imbedded in a zonal flow containing vertical and horizontal shear are examined via an analytical model of a mid-latitude cyclone. The model combines and extends some work by several previous investigators. Perturbation methods are used to formulate and solve this model. The model is continuous in three space dimensions and time. A transformation to geostrophic coordinates is employed that includes some ageostrophic effects, and additional ageostrophic terms are retained after scaling the primitive equations. The model is adiabatic, frictionless, fully compressible and the Coriolis parameter varies linearly. Perturbation series solutions are obtained which incorporate effects from vertical and horizontal shear upon quasi-geostrophic and ageostrophic terms. Normal mode solutions are found which grow due to barotropic and (primarily) baroclinic instability of the zonal flow.

The specific examples of the zonal flow are chosen to model closely conditions observed in the atmosphere during incipient mid-latitude wave-cyclone development. The horizontally averaged profiles of pressure, temperature and density were chosen to fit the corresponding profiles in the U.S. Standard Atmosphere. A meridionally variable temperature gradient is used to model a thermal front such as those observed in the atmosphere. variable temperature gradient is used to model a thermal front such as those observed in the atmosphere.

The stability, structure and energetics of some solutions are discussed. The lowest-order solutions are in basic agreement with several previous studies. The effects of the intensity and vertical structure of the model thermal front are examined in a consistent fashion. As the intensity of the front increases the growth rate increases for most wavenumbers. As the meridional width of the east-west aligned frontal zone diminishes, 1) the most unstable wavelength shifts to shorter wavelengths and 2) the fastest moving wave shifts to longer wavelengths. The structure is changed by the front in two ways: 1) the amplitude is increased in the vicinity of the front and 2) the meridional scale of the eddy is decreased in proportion to the scale of the prescribed front. The phase of the eddy pressure field is changed by the front in two ways: 1) barotropically unstable tilts are introduced and 2) the westward tilt with height is decreased in the upper region and increased in the lowest part by the horizontal shear. Examination of the energy conversions indicates that the two instability mechanisms inhibit each other. The baroclinic conversion $(\overline{A_Z \rightarrow A_E})$ is reduced by the barotropically unstable potential vorticity gradient in the interior. The barotropic conversion $(\overline{K_Z \rightarrow K_E})$ is decreased by the baroclinic vertical shear at the top and bottom through the boundary conditions ($w = 0$) there. The ageostrophic terms 1) introduce meridional asymmetry into the solution, 2) reduce the growth rate and phase speed and 3) tend to form a jet in a mean zonal flow that is initially only a function of height. Like the ageostrophic terms, the nonlinear 3) tend to form a jet in a mean zonal flow that is initially only a function of height. Like the ageostrophic terms, the nonlinear

distortion caused by the coordinate transformation improves the comparison between the model solutions and observed cyclones.

ACKNOWLEDGEMENTS

I wish to thank Dr. Cecil E. Leith and Dr. James J. O'Brien for serving as co-major professors of my doctoral research. I sincerely appreciate the time and effort they expended to help me with this research. Dr. O'Brien's aid, patience and encouragement greatly contributed to the completion of this work.

I would like to thank the other members of my doctoral committee: Dr. Albert Barcilon, Dr. Christopher Hunter and Dr. J.J. Stephens, for their comments and suggestions during the course of my doctoral studies. I thank Dr. Donna Blake for serving on my committee during part of my doctoral research.

I acknowledge the generous correspondence or discussions with Dr. Francis Bretherton, Dr. Brian Hoskins, Dr. Joseph Pedlosky, Dr. Paul Swarztrauber and Dr. Roland Sweet.

This Ph.D. degree work was supported by the National Science Foundation (NSF) through the grant ATM 76-21945. I acknowledge the services and facilities made available to me by the National Center for Atmospheric Research (NCAR). In particular, I wish to thank Kim McKinnon for typing and Ann Modahl for proofreading this manuscript.

TABLE OF CONTENTS

	Page
ABSTRACT	ii
ACKNOWLEDGEMENTS	v
LIST OF ILLUSTRATIONS	viii
LIST OF SYMBOLS	xvii
1. INTRODUCTION	1
2. MODEL DESCRIPTION	9
3. METHOD OF SOLUTION	20
4. FIRST-ORDER SOLUTION	25
5. SECOND-ORDER QUASI-GEOSTROPHIC SOLUTION	42
6. SECOND-ORDER AGEOSTROPHIC SOLUTION	78
7. SYNOPTIC ASPECTS OF THE PRIMARY VARIABLES	87
8. SUMMARY	94
APPENDICES	
A. TOTAL ADJOINT OPERATOR	105
B. NUMERICAL DETERMINATION OF ϕ_1	108
C. THE GEOSTROPHIC CORRECTION TERMS	112
D. THE ORTHOGONALITY CONDITION	114
E. VERTICAL COMPONENT VORTICITY EQUATION	
DERIVATION	116
F. THE STATIC STATE	121
DERIVATION	116
F. THE STATIC STATE	121
G. SCALING	124

	Page
H. SOME MATHEMATICAL DETAILS	127
I. FURTHER FIGURES	131
REFERENCES	146

LIST OF ILLUSTRATIONS

Figure	Page
1. A comparison of the static state used in this model (indicated by the subscript s) with the <u>U.S. Standard Atmosphere</u> (1976) (indicated by the subscript A). The static state was chosen to model closely the <u>U.S. Standard Atmosphere</u> (1976). Profiles for an isothermal atmosphere (indicated by the subscript I) are also included. The variables θ and T are potential temperature and temperature respectively, and $\kappa\epsilon$ is proportional to the static stability. θ and T are in $^{\circ}\text{K}$; Z is scaled by 10 km	12
2. The lowest-order basic state wind profiles, $U_0(Z)$ for $\beta = 0$ ($\Lambda = .8$) and for $\beta = 1$ ($\Lambda = 1.4$). In both cases $a_6 = -1$. The westerly vertical shear increases with height, but reaches a much larger maximum at $Z = 1$ in the $\beta = 1$ case. These profiles are used for the corresponding f-plane or β -plane experiments discussed in the remaining sections of this article	27
3. Growth rate spectra for the two velocity profiles shown in Fig. 1. The parameter α is related to the wavenumber, $k^2 = \epsilon\alpha^2/2$. The maximum growth rate is less for the $\beta = 1$ than for the $\beta = 0$ profile. The variation of the Coriolis parameter also introduces a long-wave cut-off (near $\alpha \sim 1.2$) and the short-wave cut-off (near $\alpha \sim 2.4$) is shifted to a slightly smaller value of α . See the text for a more complete discussion of Figs. 3-6	29
4. Phase speed spectra for the two velocity profiles shown in Fig. 1. The f-plane profile is similar to the result obtained by Eady (1949) as was the growth rate spectrum shown in Fig. 3. The β -plane profile is similar to results obtained by Green (1960). The variable Coriolis formulation reduces the phase speed. Because (18) is quadratic, the phase speed is doubly valued for neutral waves	30
Because (18) is quadratic, the phase speed is doubly valued for neutral waves	30

5. The growth rate spectra for a) $\beta = 0$ and b) $\beta = 1$ versus $U_0(1)$. Only Λ is varied, $a_6 = -1$. Since $U_0(1) = 0$, $U_0(1)$ is a crude measure of the vertical shear. In general, the growth rate increases with $U_0(1)$. As the vertical shear increasingly dominates the β -effect the long-wave cut-off approaches the $\beta = 0$ value 34
6. The phase speed spectra for a) $\beta = 0$ and b) $\beta = 1$ versus $U_0(1)$, see Fig. 5. In general, the phase speed increases with $U_0(1)$. The major exception occurs near the long-wave cut-off and results from its shift to larger wavelengths with $U_0(1)$ 35
7. The magnitude of the perturbation pressure solution at $\alpha = 2.1$ for each velocity profile shown in Fig. 2. The moduli are not symmetric with height because 1) the basic state vertical shear increases with height and 2) compressibility is included 39
8. Cross sections in geostrophic coordinates of the lowest-order eddy amplitude and phase of the pressure field and baroclinic conversion from zonal to eddy available potential energy for $\alpha = 2.0$ and $\beta = 1$. The phase diagram illustrates the meridionally uniform westward tilt with height of the trough and ridge axes. The phase angle is measured positive, eastward, relative to the value at the center top ($Y = 0, Z = 1$). The lowest-order amplitude and baroclinic conversion are largest at the center top 40
9. Cross sections in geostrophic coordinates of the basic state zonal velocity (upper figure) and prescribed potential temperature; θ and temperature; T (lower figure) for the Surface Front case where $\underline{a} = 1.6$. The prescribed thermal front in this case is confined near the bottom and has a width, for this value of \underline{a} , which is close to the Rossby radius of deformation. The letters A, B and C denote the meridional boundaries for $\alpha = 2.0, 1.8$ and 1.6 , respectively 45
10. Similar to Fig. 9 except for the Upper Front case where $\underline{a} = 1.6$. The thermal front in this case is confined near the top 47

11. Cross sections in geostrophic coordinates of the basic state potential vorticity gradient; q_y for the four cases examined in this article with $\underline{a} = 1.6$. The four cases are a) Upper Front case, b) Deep Front case, c) Surface Front case and d) Barotropic case (where U_1 is independent of Z). The four cases are distinguished by their vertical structure, the meridional variation is the same in each case. From (10) $q_y = 0$ at lowest-order, so $q_y = -\mu(U_{1YY} + a_6 \epsilon U_{1Z} + \epsilon U_{1ZZ})$. The large positive values centered about $Y = 0$ are mainly due to the U_{1YY} term 49

12. An illustration of the linear distortion of a regular grid in geostrophic coordinates (upper diagram) by the coordinate transformation into Cartesian coordinates (lower diagram). Only the basic state zonal velocity (for the Surface Front case shown in Fig. 9) is used in this linear form of the coordinate transform. The meridional boundaries for $\alpha = 2.0$ are used in these figures. The transform introduces a poleward tilt with height. In the meridional dimension, the grid is stretched on the equatorward side of the velocity maximum and compressed on the poleward side. From (7c), this figure can be used to deduce how the distributions of several quantities in geostrophic coordinates appear in Cartesian coordinates, when the eddy amplitude is very small 50

13. Second-order growth rate spectra for the Upper Front and Deep Front cases for various α and \underline{a} , where $\beta = 1$. As \underline{a} increases, the intensity of the thermal front increases and its meridional scale decreases. For the middle waves, the growth rate generally increases with \underline{a} with the shorter waves more greatly destabilized by the front. Nearly all waves are destabilized, though the long waves are only weakly unstable. The blank regions are centered about the lowest-order instability cut-offs where (13) is singular. The contour interval in Figs. 13-16 is .1. See text for further interpretation of the second-order growth rates 52

14. Similar to Fig. 13 but for the Surface Front and Barotropic cases. The second-order growth rates for the middle waves in the Barotropic case are negative 54

Figure 14. Sketch of penetrative convection in the upper ocean due to surface cooling by an imposed heat flux Q . In the mixed layer, the mean temperature \bar{T} is almost constant, while the convective heat flux \overline{wT} decreases with depth. In the thermocline, \bar{T} varies sharply, while \overline{wT} increases rapidly. The neutral level is the level where thermals and anti-thermals have the same temperature. The dotted curve is the mean-temperature profile at a later time, showing the cooling in the mixed layer and the heating in the thermocline.

Figure 15. Plots of the coefficients ε and A defined by (50) and (58), ε is the ratio $\bar{T}/(-\Gamma h)$, and A is the ratio $-(\overline{wT})_{-h}/Q$.

Figures 16a and b

(a) Dimensionless vertical velocity variance and (b) dimensionless vertical turbulent flux of vertical heat flux near the surface, for $(1-mD)/\kappa m=5$ and $2m=0.64$. Dots correspond to atmospheric observations presented by Wyngaard, *et al.* (1971).

Figure 17. Vertical profile of the rms vertical velocity, scaled by $-w_{*}$.

Figure 18. Vertical profiles of the vertical-velocity variance, $\overline{w^2}$, scaled by w_{*}^2 . The solid curve is the solution of the present model. The dashed curve is the numerical solution of Zeman and Lumley (1976). The dots represent the data of Willis and Deardorff (1974), run S1.

Figure 19. Vertical profiles of the vertical flux of turbulent kinetic energy, $-\frac{1}{2}\overline{ww^2}$, scaled by w_{*}^3 . The solid curve is the solution of the present model. The dashed curve is the numerical solution of Zeman and Lumley (1976). The dots represent the data of Willis and Deardorff (1974), run S1.

Figure 20. Vertical profiles of the temperature variance, $(T-\bar{T})^2$, scaled by $(u_{*}/Q)^2$. The solid curve is the solution of the present model. The dashed curve is the solution of Zeman and Lumley (1976). The dots represent the data of Willis and Deardorff (1974), run S1.

Figure 21. Vertical profile of the mean temperature, \bar{T} , scaled by Γh .

Figure 21. Vertical profile of the mean temperature, \bar{T} , scaled by Γh .

- Figure 22. Vertical profile of the vertical convective heat flux \overline{wT} , scaled by the surface flux Q . The dots represent the data of Willis and Deardorff (1974), run S1.
- Figure 23. Vertical profile of the eddy heat diffusivity, ν_T , scaled by Q/Γ .
- Figure 24. Dimensionless turbulent kinetic energy budget: release of potential energy (dashed line), transport (solid line), and dissipation (dotted line).
- Figure 25. Same as figure 24, but for run S1 of Willis and Deardorff (1974).
- Figure 26. Vertical profile of the vertical-velocity variance, $\overline{w^2}$, scaled by w_{*i}^2 , as on figure 18 but for $R_i = 45$. The triangles represent the data of Willis and Deardorff (1974), run S2.
- Figure 27. Vertical profile of the vertical flux of turbulent kinetic energy, $-\frac{1}{2}\overline{ww^2}$, scaled by w_{*i}^3 , as figure 19 but for $R_i = 45$. The triangles represent the data of Willis and Deardorff (1974), run S2.
- Figure 28. Vertical profile of the vertical convective heat flux, \overline{wT} , scaled by the surface flux Q , as on figure 20 but for $R_i = 45$. The triangles represent the data of Willis and Deardorff (1974), run S2.
- Figure 29. Imposed wind-stress field.
- Figure 30. Initial buoyancy field.
- Figure 31. Cross-front section of the buoyancy field in the case of convergence, for time $t = 1.60$ and $a = 0.1$.
- Figure 32. Cross-front section of the buoyancy field in the case of convergence, for time $t = 1.60$ and $a = 1.0$.
- Figure 33. Cross-front section of the buoyancy field in the case of convergence, for time $t = 0.16$ and $a = 10$.
- Figure 34. Cross-front variation of the mean buoyancy in the mixed layer in the case of convergence, for three different values of the mixing parameter a . For $a = 0.1$ and 1.0 , values are plotted at time $t = 1.60$. For $a = 10$, values are plotted at time $t = 0.16$. The dashed line represents the initial linear profile. For different values of the mixing parameter a . For $a = 0.1$ and 1.0 , values are plotted at time $t = 1.60$. For $a = 10$, values are plotted at time $t = 0.16$. The dashed line represents the initial linear profile.

- Figure 35. Evolution of the mixed-layer depth on both sides of the front ($y = \pm 0.5$) in the case of convergence, for three different values of the mixing parameter a .
- Figure 36. Cross-front section of the buoyancy field in the case of confluence, for time $t = 1.60$ and $a = 0.1$.
- Figure 37. Cross-front section of the buoyancy field in the case of confluence, for time $t = 1.60$ and $a = 1.0$.
- Figure 38. Cross-front section of the buoyancy field in the case of confluence, for time $t = 0.16$ and $a = 10$.
- Figure 39. Cross-front variation of the mean buoyancy in the mixed layer in the case of confluence, for three different values of the mixing parameter a . For $a = 0.1$ and 1.0 , values are plotted at time $t = 1.60$. For $a = 10$, values are plotted at time $t = 0.16$. The dashed line represents the initial linear profile.
- Figure 40. Evolution of the mixed-layer depth on both sides of the front ($y = \pm 0.5$) in the case of confluence, for three different values of the mixing parameter a .

LIST OF SYMBOLS

Symbol	Meaning	Dim.	Remark
a	Any physical quantity (Chap.2)	-	
	<u>or</u> Mixing parameter (Chap. 5)	1	>0
A	Ratio of heat flux at the bottom of the mixed layer to surface heat flux	1	>0
b	Buoyancy: $b = g(-\alpha T + \beta S)$	LT^{-2}	
b_0	Reference buoyancy	LT^{-2}	constant
b_-	Buoyancy in the stratified fluid	LT^{-2}	
B	Total mixed-layer buoyancy (Chap.3 & 4)	L^2T^{-2}	
	<u>or</u> Scale for $\bar{b} - b_0$ and $b_- - b_0$ (Chap.5)	LT^{-2}	
B	Maximum vertical buoyancy flux	L^2T^{-3}	
c	Any physical quantity	-	
D	Rate of dissipation (Chap.3)	ML^2T^{-3}	
	<u>or</u> Dissipation coefficient (Chap.4)	1	>0
DIM	Dynamic Instability Model	-	
E	Volume exchange (Chap.2)	T^{-1}	>0 or <0
	<u>or</u> Dimensionless rate of entrainment (Chap. 3 & 4)	1	
E_m	Mass exchange	$ML^{-3}T^{-1}$	>0 or <0
f	Fraction of area occupied by thermals to the total area	1	$0 < f < 1$
f_0	Coriolis parameter	T^{-1}	
F_s	TKE flux at the surface	ML^2T^{-3}	
F_h	TKE flux at the bottom of thermocline	ML^2T^{-3}	
g	Acceleration of gravity	LT^{-2}	constant
F_h	TKE flux at the bottom of thermocline	ML^2T^{-3}	
g	Acceleration of gravity	LT^{-2}	constant
h	Mixed-layer depth	L	

h_0	Initial mixed-layer depth	L
\dot{h}	Rate of entrainment of stratified fluid in the mixed layer	LT^{-1}
H	Scale for the mixed-layer depth and z	L
\tilde{k}	Vertical unit vector, pointing upward	1
KE	Total Kinetic Energy	ML^2T^{-2}
ℓ	Monin-Obukov length: $\ell = u_*^3 / \kappa B$	L
L	Horizontal length scale	L
m	$m = \frac{1}{2} (1-2f)(f(1-f))^{\frac{1}{2}}$	1
MKE	Total Mean Kinetic Energy	ML^2T^{-2}
\tilde{n}	Horizontal components of the outward unit normal to Σ	1
n_z	Vertical component of the outward unit vector to Σ	1
N	Brunt-Väisälä frequency in the stratified fluid: $N^2 = \alpha g \Gamma$	T^{-1}
p	Pressure	$ML^{-1}T^{-1}$
PE	Total Potential Energy	ML^2T^{-2}
Q	Kinematic surface heat flux: $Q = \overline{wT} _{\text{surf}}$	KLT^{-1} >0 upward
Ri	Frictional Richardson number $Ri = B/u_*^2$ (Chap.3), $Ri = B/w_*^2$ (Chap.4)	1
Ro	Rossby number: $Ro = V/f_0 L$ (Chap.5)	1
Rv	Overall Richardson number $Rv = B/(U^2 + V^2)$ (Chap.3)	1
S	Sum of contributions to TKE budget (Chap.2) <u>or</u> Salinity (Chap.5)	ML^2T^{-3} S
t	Time variable	T
T	Temperature, as in T', T'', \bar{T}, T	K
t	Time variable	T
T'	Temperature, as in $T', T'', \bar{T}, T_{\text{rms}}$ <u>or</u> Depth-independent part of \bar{T}/Γ	K L

T_o	Reference temperature	K	constant
\tilde{T}	T_{rms}/Γ	L	
TEM	Turbulent Erosion Model	-	
TKE	Total Turbulent Kinetic Energy	ML^2T^{-2}	
u	Horizontal velocity in the x-direction, as in $u', u'', \bar{u}, u_{rms}$	LT^{-1}	
u_*	Friction velocity	LT^{-1}	>0
\tilde{u}	u_{rms}	LT^{-1}	
U	Depth-independent part of \bar{u} (Chap.3)	LT^{-1}	
	<u>or</u> Scale for \bar{u} (Chap.5)	LT^{-1}	
U_*	Scale for u_*	LT^{-1}	
v	Horizontal velocity in the y-direction	LT^{-1}	
\tilde{v}	v_{rms}	LT^{-1}	
V	Total volume of the system (Chap.2)	L^3	
	<u>or</u> Depth-independent part of \bar{v} (Chap.3)	LT^{-1}	
	<u>or</u> Scale for \bar{v} (Chap.5)	LT^{-1}	
w	Vertical velocity, as in $w', w'', \bar{w}, w_{rms}$	LT^{-1}	
w_{Ek}	Ekman vertical velocity in stratum	LT^{-1}	
\tilde{w}	$-w_{rms}$	LT^{-1}	
W	Scale for \bar{w} and w_{Ek}	LT^{-1}	
x	(Long-front) horizontal coordinate	L	
y	(Cross-front) horizontal coordinate	L	
z	Vertical upward coordinate	L	
α	Coefficient of thermal expansion	K^{-1}	
β	Coefficient of salinity contraction	S^{-1}	
α	coefficient of thermal expansion	K^{-1}	
β	Coefficient of salinity contraction	S^{-1}	
Γ	Vertical temperature gradient in the stratified fluid	KL^{-1}	

Γ_2	Initial horizontal buoyancy gradient	T^{-2}	
Γ_3	Initial vertical buoyancy gradient	T^{-2}	
δ	Friction force in the vert. mom. eqn.	LT^{-2}	
$\delta\xi$	Dimensionless thickness of thermocline	1	
ΔT	Temperature jump across the thermocline	K	
$\Delta\rho$	Density jump across the thermocline	ML^{-3}	
$\nabla_{\sim H}$	Two-dimensional gradient operator	L^{-1}	
ϵ	Coefficient of proportionality between T and h: $T=\epsilon h$	1	
η	Similarity coordinate near surface: $\eta=-z/\ell$	1	$\eta \geq 0$
κ	Von Kármán constant	1	constant
ν_T	Eddy heat diffusivity	L^2T^{-1}	
ν_u	Eddy viscosity in the x-direction	L^2T^{-1}	
ν_v	Eddy viscosity in the y-direction	L^2T^{-1}	
ξ	Similarity variable: $\xi=-z/h$	1	$0 \leq \xi \leq 1$
ρ	Density	ML^{-3}	
ρ_0	Reference density	ML^{-3}	constant
Σ	The closed surface bounding the system	-	
τ	Dimensionless τ_x	1	
τ_x	Wind-stress in the x-direction	$ML^{-1}T^{-2}$	
τ_y	Wind-stress in the y-direction	$ML^{-1}T^{-2}$	
(...)'	Quantity referring to thermals	-	
(...)"	Quantity referring to anti-thermals	-	
$\overline{(\dots)}$	Mean quantity	-	
$(\dots)_{rms}$	Root-mean-square fluctuation	-	>0 or <0
(...)	Mean quantity	-	
$(\dots)_{rms}$	Root-mean-square fluctuation	-	>0 or <0

Air-sea interactions cannot be successfully modelled without a deep knowledge of the upper-ocean dynamics and thermodynamics. The currents and variations of temperature and salinity in the upper ocean are induced and controlled by surface atmospheric conditions, oceanic lateral advection, and deep oceanic conditions. The complexity of the situation can, however, be somewhat simplified by classifying the various processes which take place in the upper ocean. They are: turbulent mixing by wind stirring or mean current shear, convection, penetrative convection, entrainment of stratified fluid, and re-stratification. All these processes involve small-scale turbulent motions, in space as well as in time. In this work, the resulting fine structure is studied in order to achieve a better knowledge of the dynamics and thermodynamics in the upper ocean.

Upper-ocean processes can be thought of as the relative motion of two interacting fluids: the sinking fluid parcels generated near the surface and transmitting surface information downward and the rising fluid parcels forming the return flow. The former play the active role in mixing and convection, and are called *thermals*. The latter play the alternate passive role and are called *anti-thermals*. A general theory based on this concept is developed and applied to various cases, including deepening of the wind-mixed layer, penetrative convection due to surface cooling, and upper-ocean frontogenesis due to horizontal advection. Penetrative convection due to surface cooling, and upper-ocean frontogenesis due to horizontal advection.

The work is divided into several chapters (Chapters 2 to 5), each of them being a discrete and independent entity. As an advantage, the reader interested in one specific topic may limit his/her reading to a particular chapter without facing problems understanding symbols or basic ideas. Despite advantages, this presentation leads to some unavoidable repetition, for which the author apologizes.

Chapter two is the development of the general theory of mixing and convection, based on the concept of a two-fluid system. It is an application of the dynamical theory of interacting continua proposed by Kelly (1964), developed by Green and Naghdi (1965), and generalized by Truesdell (1969). The equations are written for two interacting Boussinesq fluids in a rotating frame. Interaction terms are parametrized for the purpose of geophysical situations. Pairs of governing equations are derived for thermals and anti-thermals. Each pair meets an Invariance Principle as a consequence of reciprocity in the roles played by thermals and anti-thermals. Considerable simplification is obtained by assuming that the response time of turbulence is much less than the time scale of evolution of the overall system. This assumption is realized in all geophysical situations. Each pair of governing equations is transformed into an average equation for which interaction terms cancel, combined with a very simple equation linking the two fluid properties. An important parameter of the model is the fraction, f , of area occupied by thermals. Since a closure assumption is needed, a dynamic saturation equilibrium between thermals and anti-thermals is assumed. Since a closure assumption is needed, a dynamic saturation equilibrium between thermals and anti-thermals is assumed. This implies a constant value of f throughout the convective layer.

Chapter three is the application of the theory to the deepening of the wind-mixed layer. In view of simple algebra, the model is one-dimensional, frictionless, and neglects the turbulence production by the mean-flow shear in the thermocline. Hence, the increase in potential energy required for deepening is supplied by the turbulence input at the surface. The analytical treatment of the equations is simplified using the well-known facts that the mixed layer is quasi-homogeneous and that the thermocline is a thin layer of large gradients. The vertical structure throughout the mixed layer and thermocline is given by an analytical solution. Vertical profiles of mean velocity components, mean temperature, and vertical fluxes of momentum and heat are then plotted. The solution also yields bulk formulae predicting the rate of deepening, the thermocline thickness, and the mean surface temperature. As the mixed layer deepens, the thermocline shallows, vertical profiles, therefore do not remain similar to themselves in time. The analytical solution is not self-similar.

Chapter four is the application of the theory to penetrative convection due to surface cooling, as it occurs past mid-fall and during winter. The model is still one-dimensional, but includes dissipation. Wind stirring plays an important role when the convective layer is shallow, but rapidly convection dominates the process. Thermal instability itself supplies the kinetic energy required for stirring and deepening. Wind stirring is therefore ignored in that section. Assuming a quasi-homogeneous mixed layer required for stirring and deepening. Wind stirring is therefore ignored in that section. Assuming a quasi-homogeneous mixed layer and a sharp thermocline, a single non-similar analytical solution is found. Vertical profiles of mean values and vertical fluxes

are plotted for the mixed layer and the thermocline. The solution also yields bulk formulae predicting the rate of deepening, the mean surface temperature, the heat flux at the bottom of the mixed layer and the thermocline thickness. Although the results presented here focus on convection in the upper ocean forced by surface cooling, they also apply directly to convection in the atmospheric boundary layer above a heated ground.

Chapter five is a study of advective effects and their interactions with wind-mixing effects. A case of frontogenesis is chosen in order to include lateral variations in advection and mixing and in order to understand better frontal dynamics of the large-scale oceanic fronts in the central North Pacific. Interactions between advection and mixing result in important cross-front asymmetries in properties such as mixed-layer depth, pycnocline strength, and/or mixed-layer density. Two cases are treated separately: the case of convergence (when the water masses downwell at the front) and the case of confluence (when the water masses form a long-front current).

CHAPTER TWO

A GENERAL THEORY OF MIXING AND CONVECTION:
MODELLING BY TWO BUOYANT INTERACTING FLUIDS

1. INTRODUCTION

Convection may be caused by either an initially unstable situation or by a continuously-applied external forcing. In most geophysical convective situations, convection is of the latter kind and is maintained by a forcing which is almost invariably applied along one boundary rather than within the fluid. The theory developed here attempts to model convection when convective motions are driven under such circumstances. Convection of air above a heated ground, mixing of the upper ocean under the action of wind stress and/or surface cooling, and penetrative convection in stars are some examples.

Along the boundary where the forcing is applied, fluid particles coming from the interior are altered; their velocity components and/or temperature are modified. The same particles thus leave the boundary with new properties. As a consequence of this mechanism, convection can be thought of as the relative motion of two different fluids: the fluid particles coming from the interior toward the boundary, and the altered fluid particles leaving that boundary with different properties. The latter play the active role in convection and will be called *thermals*. This name was adopted by glider pilots for masses of warm air rising from hot ground. Ever since, this word has been widely used in the field of convection. The other fluid parcels play an alternate passive role and will be called *anti-thermals*. The other fluid parcels play an alternate passive role and will be called *anti-thermals*.

The model presented here does not require interpreting thermals and anti-thermals as discrete elements. Particles will not be numbered nor will they be assigned a volume. The two fluids may be considered like plumes, puffs or other forms (Scorer, 1978). However, the terminology of thermals and anti-thermals is used for convenience because discrete elements are more easily perceived. As a formal extension, the word thermal will be even assigned arbitrarily to non-buoyant fluid having an excess of momentum.

Priestley (1959) has shown how one can obtain information about the mean properties and the fluctuations in air over a heated ground by considering it as the superposition of many closely-spaced convecting elements. However, his approach is limited to environmental lapse rate constant with height and does not allow the elements to grow or decrease as they migrate vertically.

The model developed here is an extension of the dynamical theory of interacting continua proposed by Kelly (1964) and Green and Naghdi (1965), and extended by Truesdell (1969). For the present purpose, equations are written for a two-fluid continuum in a rotating frame. The Boussinesq approximations are made (Spiegel and Veronis, 1960), and interaction terms are parametrized in view of geophysical situations.

The forcing along the boundary generates thermals at the expense of anti-thermals, whereas interactions between the two fluids in the interior progressively transform thermals back to anti-thermals. Thermals are directly driven by the external forcing, while anti-thermals are driven by reaction to the thermals

(continuity of mass, conservation of momentum and heat). The two fluids have different properties; their relative motion is thus a mechanism capable of transferring heat, momentum, energy, or any other constituent, through the convective layer.

2. FRACTION OF AREA OCCUPIED BY THERMALS

At a given level, any horizontal surface is crossed by thermals and anti-thermals. At a given time, a given horizontal area A is occupied partly by thermals and partly by anti-thermals (Figure 1). From a hypothetical instant infra-red picture detecting warm and cold regions, one may compute the fraction of area occupied by thermals for that surface at that time. That value inevitably varies in a certain range, and a theoretical ensemble average yields, in a statistical sense, a local instantaneous mean value. If one evokes the hypothesis of ergodicity, this averaging process is equivalent to an average over horizontal distances and time intervals short compared to lateral and temporal scales of variation characterizing the whole system. The resulting quantity, noted as f , is dimensionless, positive and less than unity (Manton, 1975). As a direct result, the fraction of area available to anti-thermals is $(1-f)$. Although it is anticipated that f will be assumed to be a constant, the governing equations derived hereafter are written in a general framework, allowing local and temporal variations of f .

The observed mean value of any quantity is a combination of allowing local and temporal variations of f .

The observed mean value of any quantity is a combination of contributions due to the two fluids in the ratio of their respective

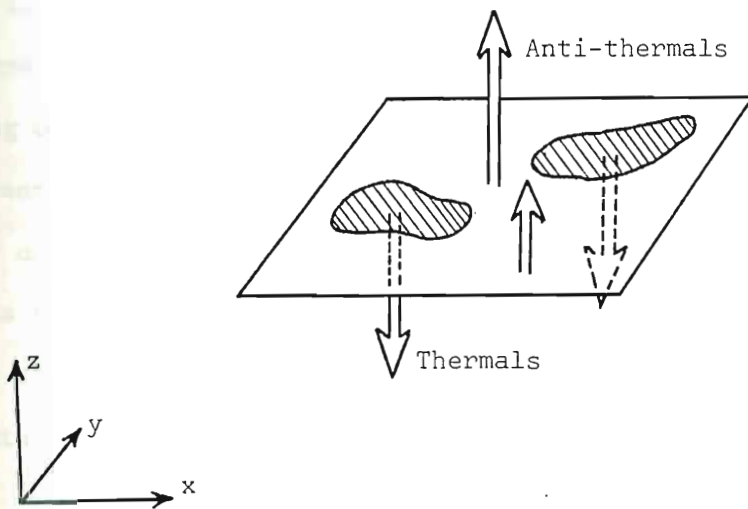


Figure 1. The fraction of area occupied by thermals at any level is the instantaneous local value, averaged over horizontal distances and time intervals short compared to lateral and temporal scales of variation of the overall system. The fraction of area occupied by anti-thermals is the instantaneous local value, averaged over horizontal distances and time intervals short compared to lateral and temporal scales of variation of the overall system.

available areas:

$$\text{horizontal velocity} \quad \bar{u} = fu' + (1-f)u'', \quad (1)$$

$$\bar{v} = fv' + (1-f)v'', \quad (2)$$

$$\text{vertical velocity} \quad \bar{w} = fw' + (1-f)w'', \quad (3)$$

$$\text{pressure} \quad \bar{p} = fp' + (1-f)p'', \quad (4)$$

$$\text{density} \quad \bar{\rho} = f\rho' + (1-f)\rho'', \quad (5)$$

$$\text{temperature} \quad \bar{T} = fT' + (1-f)T'', \quad (6)$$

where primed and double-primed quantities refer to thermals and anti-thermals, respectively. The bar thus represents an operator averaging over short horizontal distances and short time intervals in the sense defined previously. It indirectly assumes that each fluid is characterized by single values rather than by distribution functions of their properties.

The above relations, rather than a definition of mean values, constitute the mathematical expression of the average operator:

$$\bar{a} = fa' + (1-f)a'',$$

where a represents any physical quantity. The application of this operator may also define momentum, heat and energy fluxes. In the context of Boussinesq approximations, the vertical fluxes of horizontal momentum (Reynolds stresses divided by ρ_0 , the reference density) are:

$$-\overline{uw} = -fu'w' - (1-f)u''w'', \quad (7)$$

$$-\overline{vw} = -fv'w' - (1-f)v''w'', \quad (8)$$

$$-\overline{uw} = -fu'w' - (1-f)u''w'', \quad (7)$$

$$-\overline{vw} = -fv'w' - (1-f)v''w'', \quad (8)$$

the kinematic vertical convective heat flux (heat flux divided by $\rho_o C_p$) has the form:

$$\overline{wT} = fw'T' + (1-f)w''T'', \quad (9)$$

and the vertical flux of turbulent kinetic energy reads:

$$\begin{aligned} & \overline{\frac{1}{2} w \left[(u-\bar{u})^2 + (v-\bar{v})^2 + (w-\bar{w})^2 \right]} \\ &= \frac{1}{2} fw' \left[(u'-\bar{u})^2 + (v'-\bar{v})^2 + (w'-\bar{w})^2 \right] \\ &+ \frac{1}{2} (1-f)w'' \left[(u''-\bar{u})^2 + (v''-\bar{v})^2 + (w''-\bar{w})^2 \right]. \end{aligned} \quad (10)$$

Other fluxes may be defined in an analogous way but are not of primary importance to geophysical convection problems.

Finally, the averaging operator may also be used to define root-mean-square (rms) quantities, measuring departures from mean values. If a represents any physical quantity, the rms fluctuation is defined as:

$$a_{\text{rms}} = \pm \overline{(a - \bar{a})^2}^{\frac{1}{2}}, \quad (11)$$

$$\text{i.e., } a_{\text{rms}}^2 = f(a' - \bar{a})^2 + (1-f)(a'' - \bar{a})^2. \quad (12)$$

Simple calculations yield:

$$a_{\text{rms}} = \left(\frac{f}{1-f} \right)^{\frac{1}{2}} (a' - \bar{a}) = - \left(\frac{1-f}{f} \right)^{\frac{1}{2}} (a'' - \bar{a}) \quad (13)$$

$$= [f(1-f)]^{\frac{1}{2}} (a' - a''). \quad (14)$$

The sign is selected as to yield a positive value when the thermals quantity a' exceeds the mean value \bar{a} . The rms fluctuation is directly proportional to the difference between thermals and anti-thermals and exceeds the mean value \bar{a} . The rms fluctuation is directly proportional to the difference between thermals and anti-thermals values, and is zero when these values are equal and do not

differ from the mean.

3. MASS AND VOLUME EXCHANGES BETWEEN THERMALS AND ANTI-THERMALS

Thermals and anti-thermals continuously exchange mass and, consequently, momentum, heat, and energy. At any moment and at any location, either thermals or anti-thermals lose some of their mass to the other. The exchange is controlled by E_m , the *mass* exchange per unit time and total volume of fluid ($\text{kg m}^{-3}\text{s}^{-1}$). However, in the Boussinesq framework, that quantity is advantageously replaced by the *volume* exchange, E , per unit time and total volume (s^{-1}) defined as:

$$E = \frac{E_m}{\rho_0}, \quad (15)$$

where ρ_0 is the reference density close to the actual densities of thermals and anti-thermals, ρ' and ρ'' , respectively. By definition, the mass exchange, E_m , is chosen to be positive if anti-thermals lose mass to thermals and is negative if thermals lose mass to anti-thermals.

In subsequent sections, it will be assumed that heat and momentum are transferred exclusively through this mass exchange, thus excluding transfer by diffusion or collision. However, this assumption may be questionable for highly turbulent clouds, where momentum exchange between air masses can occur without mass exchange, as in a collision.

exchange between air masses can occur without mass exchange, as in a collision.

4. INVARIANCE PRINCIPLE

From a semantic point of view, thermals and anti-thermals play reciprocal roles: what is lost by one is gained by the other. Thermals may be labelled anti-thermals and vice-versa. Their dynamics and thermodynamics are therefore to be governed by corresponding equations and the following Invariance Principle must hold:

Principle: All the governing equations must be invariant under the transformation:

$$\left| \begin{array}{l} \text{primed quantity} \longleftrightarrow \text{double-primed quantity} \\ f \longleftrightarrow 1-f \\ E \longleftrightarrow -E \\ \text{rms fluctuation} \longleftrightarrow -\text{rms fluctuation.} \end{array} \right.$$

It may easily be seen that any mean quantity such as \bar{u} , $-\overline{uw}$, \overline{wT} , ... is invariant under that transformation, and equations for mean values will thus automatically meet the Invariance Principle.

5. GOVERNING EQUATIONS

The dynamics and thermodynamics of two interacting fluids are parts of the mathematical theory of mixtures. This latter theory aims to represent exchanges of mass, momentum, heat, and energy. Particular cases are theories of diffusion and chemical homogeneous reactions and kinetic theories of mass, momentum, heat, and energy. Particular cases are theories of diffusion and chemical homogeneous reactions and kinetic theories of heterogeneous continua. A general framework for all such theories has been laid down by Kelly (1964),

Green and Naghdi (1965), and Truesdell (1969, Lecture 5) so as to include magnetohydrodynamic and other effects. Here, the governing equations are written for a two-fluid Boussinesq rotating continuum. Moreover, interaction terms are parametrized in view of geophysical situations.

a) Preliminary remark:

Thermals and anti-thermals have relatively large vertical velocities. Due to these sinking or rising motions, they do not have time nor do they go far enough laterally to be affected by temporal and horizontal variations in the overall system. As a result, in any equation, operators such as

$$\frac{\partial}{\partial t}(fa'), \frac{\partial}{\partial x}(fu'a'), \frac{\partial}{\partial y}(fv'a'), \frac{\partial}{\partial x}((1-f)u''a''), \dots$$

lead to terms which are negligible compared to those involving the vertical operators applied to the same quantities:

$$\frac{\partial}{\partial z}(fw'a'), \frac{\partial}{\partial z}((1-f)w''a''),$$

i.e., vertical advection is the dominant part of the substantial time derivative. (See Appendix A for a detailed mathematical treatment.)

However, it will be seen in the treatment of the continuity equations that, in the case of zero global vertical motion, w' and w'' almost exactly balance each other, so that, in the equations for average variables, operators such as

$$\frac{\partial}{\partial t} \bar{a}, \frac{\partial}{\partial x}(\overline{ua}), \frac{\partial}{\partial y}(\overline{va})$$

$$\frac{\partial}{\partial t} \bar{a}, \frac{\partial}{\partial x}(\overline{ua}), \frac{\partial}{\partial y}(\overline{va})$$

lead to terms comparable to those yielded by the vertical flux

operator:

$$\frac{\partial}{\partial z} (\overline{wa}) .$$

These conclusions are equivalent to stating that the response time of the two interacting fluids is much less than the time scale of evolution of the overall convective system.

The system is thus characterized by two time scales: time variations of the whole system will be resolved at the long time scale, by assuming a quasi-instantaneous response of the fluctuations at the short time scale.

b) Equation of state:

If salinity or other density variable effects are unimportant, and if density variations do not exceed a few percent, the equation of state may be adequately represented by a linear dependence upon the temperature only:

for thermals:
$$\rho' = \rho_0 (1 - \alpha(T' - T_0)), \quad (16)$$

for anti-thermals:
$$\rho'' = \rho_0 (1 - \alpha(T'' - T_0)), \quad (17)$$

where α is the coefficient of thermal expansion ($\alpha = 3.5 \times 10^{-3} \text{ } ^\circ\text{C}^{-1}$ for air at 15°C , $\alpha = 10^{-4} \text{ } ^\circ\text{C}^{-1}$ for pure water at 10°C), and T_0 is the reference temperature. The mean density is related to the mean temperature by:

$$\bar{\rho} = \rho_0 (1 - \alpha(\bar{T} - T_0)). \quad (18)$$

$$\bar{\rho} = \rho_0 (1 - \alpha(\bar{T} - T_0)). \quad (18)$$

This latter result is obtained simply by summing (16) and (17) pre-

multiplied by f and $(1-f)$, respectively. (If density is a linear function of salinity, an equation similar to (18) may be derived.)

c) Continuity equation:

In the Boussinesq framework, the variations of density are small, and the continuity equation is equivalent to the law of conservation of volume (Spiegel and Veronis, 1960). The equations become:

for thermals:

$$\frac{\partial}{\partial t} f + \frac{\partial}{\partial x}(fu') + \frac{\partial}{\partial y}(fv') + \frac{\partial}{\partial z}(fw') = E, \quad (19)$$

for anti-thermals:

$$\frac{\partial}{\partial t}(1-f) + \frac{\partial}{\partial x}((1-f)u'') + \frac{\partial}{\partial y}((1-f)v'') + \frac{\partial}{\partial z}((1-f)w'') = -E, \quad (20)$$

where E is the volume exchange between the two fluids, per unit time and volume, and is positive if anti-thermals lose mass to thermals (positive divergence of the thermals velocity field). It may be easily shown that the above two equations meet the Invariance Principle.

Summing (19) and (20), an averaged continuity equation is obtained:

$$\frac{\partial}{\partial x} \bar{u} + \frac{\partial}{\partial y} \bar{v} + \frac{\partial}{\partial z} \bar{w} = 0. \quad (21)$$

As stated in the preliminary remark, the term $\partial \bar{w} / \partial z$ of this equation is the sum of the dominant terms in the left-hand sides of (19) and (20). The two other terms, $\partial \bar{u} / \partial x$ and $\partial \bar{v} / \partial y$, are the sum of negligible terms. Therefore, the two contributions to $\partial \bar{w} / \partial z$ almost cancel each other, and one may write:

$$\overline{\frac{\partial w}{\partial z}} = 0,$$

i.e., the mean vertical velocity is z-independent. Since, in most cases, there is no mean upwelling or downwelling, this mean velocity ought to be zero everywhere, leading to a relationship between w' and w'' :

$$\overline{w} = fw' + (1-f)w'' = 0. \quad (22)$$

To the same level of approximations, equations (19) and (20) reduce to:

$$E = \frac{\partial}{\partial z}(fw') = - \frac{\partial}{\partial z}((1-f)w''). \quad (23)$$

In the regions where variations of f are unimportant, $E=f\partial w'/\partial z$, i.e., thermals grow ($E > 0$) when they accelerate ($\partial w'/\partial z > 0$), and decrease in size ($E < 0$) when they decelerate ($\partial w'/\partial z < 0$). Note that E has not been parametrized in any manner.

d) Heat conservation equation:

In the context of Boussinesq approximations, the heat conservation equations are:

for thermals:

$$\frac{\partial}{\partial t}(fT') + \frac{\partial}{\partial x}(fu'T') + \frac{\partial}{\partial y}(fv'T') + \frac{\partial}{\partial z}(fw'T') = \frac{1}{2} E(T'+T''), \quad (24)$$

for anti-thermals:

$$\begin{aligned} \frac{\partial}{\partial t}((1-f)T'') + \frac{\partial}{\partial x}((1-f)u''T'') + \frac{\partial}{\partial y}((1-f)v''T'') + \frac{\partial}{\partial z}((1-f)w''T'') \\ = -\frac{1}{2} E(T'+T''), \quad (25) \end{aligned}$$

where molecular diffusivity and internal source of heat are neglected, $= -\frac{1}{2} E(T'+T'')$, (25)

where molecular diffusivity and internal source of heat are neglected, since they are unimportant for most geophysical convective situ-

ations. The heat exchange between thermals and anti-thermals is modelled by a transfer of mass at the mean temperature $(T'+T'')/2$. A justification of this parametrization and a discussion of a more general formulation is presented in Appendix B.

The above equations, which meet the Invariance Principle, could also have been written in terms of the buoyancies

$$b' = -\alpha g(T' - T_0), \quad b'' = -\alpha g(T'' - T_0).$$

The sum of equations (24) and (25) yields the global heat conservation equation:

$$\frac{\partial}{\partial t} \bar{T} + \frac{\partial}{\partial x} \overline{uT} + \frac{\partial}{\partial y} \overline{vT} + \frac{\partial}{\partial z} \overline{wT} = 0, \quad (26)$$

which expresses that the time rate of change of the mean temperature \bar{T} is equal to the negative of the divergence of the convective heat flux. In the case of horizontal homogeneity on scales much larger than the one of thermals, the reduced equation is:

$$\frac{\partial}{\partial t} \bar{T} = - \frac{\partial}{\partial z} \overline{wT}, \quad (27)$$

where the vertical convective heat flux \overline{wT} is defined by (9).

Subtracting from (24) and (25) the continuity equations (19) and (20) pre-multiplied by T' and T'' , respectively, and assuming that thermals and anti-thermals do not have time to see lateral and temporal variations (preliminary remark), one obtains:

$$fw' \frac{\partial T'}{\partial z} = \frac{1}{2} E(T'' - T'), \quad (28)$$

$$(1-f)w'' \frac{\partial T''}{\partial z} = \frac{1}{2} E(T'' - T'), \quad (29)$$

$$fw' \frac{\partial T'}{\partial z} = \frac{1}{2} E(T'' - T'), \quad (28)$$

$$(1-f)w'' \frac{\partial T''}{\partial z} = \frac{1}{2} E(T'' - T'). \quad (29)$$

By use of (22), the difference of these two equations leads to:

$$\frac{\partial}{\partial z} (T' + T'') = 0, \quad (30)$$

stating that vertical variations of temperatures are inversely correlated. This last equation is remarkable by its simplicity. As one may expect, similar results will be obtained from the treatment of the horizontal momentum equations, and these will greatly facilitate further computations.

e) Horizontal momentum equation:

In the context of Boussinesq approximations, the horizontal momentum equations on a rotating f_0 -plane are:

for thermals:

$$\begin{aligned} & \frac{\partial}{\partial t}(fu') + \frac{\partial}{\partial x}(fu'u') + \frac{\partial}{\partial y}(fv'u') + \frac{\partial}{\partial z}(fw'u') + ff_0 k \times u' \\ & = -\frac{1}{\rho_0} \nabla_H (fp') + \frac{1}{2} E(u'+u'') + \frac{1}{2}(1-2f)E(u'-u''), \end{aligned} \quad (31)$$

for anti-thermals:

$$\begin{aligned} & \frac{\partial}{\partial t}((1-f)u'') + \frac{\partial}{\partial x}((1-f)u''u'') + \frac{\partial}{\partial y}((1-f)v''u'') + \frac{\partial}{\partial z}((1-f)w''u'') \\ & + (1-f)f_0 k \times u'' = -\frac{1}{\rho_0} \nabla_H ((1-f)p'') - \frac{1}{2} E(u'+u'') - \frac{1}{2}(1-2f)E(u'-u''), \end{aligned} \quad (32)$$

where $u'=(u',v',0)$, $u''=(u'',v'',0)$ are the horizontal velocity components of thermals and anti-thermals, respectively, $k=(0,0,1)$ the vertical unit vector pointing upward, ∇_H the two-dimensional gradient operator $(\frac{\partial}{\partial x}, \frac{\partial}{\partial y}, 0)$, and f_0 is the Coriolis parameter.

Thermals and anti-thermals are subjected to two different pressures (Truesdell, 1969). Viscous forces are neglected since they are unimportant for most geophysical convective situations. The exchange of momentum is modelled by a transfer of mass at the mean

horizontal velocity $(\underline{u}' + \underline{u}'')/2$, analogous to the heat transfer. It may be shown that this form of exchange is the only one that conserves total kinetic energy in the horizontal motion. The last term of each equation represents a kinetic energy exchange, which is converted to kinetic energy in the vertical motion (See section about energetics). Finally, it may be seen that the pair of equations meets the Invariance Principle.

The sum of equations (31) and (32) yields an equation governing the mean horizontal momentum $\bar{\underline{u}} = (\bar{u}, \bar{v}, 0)$:

$$\frac{\partial}{\partial t} \bar{\underline{u}} + \frac{\partial}{\partial x} \overline{u\underline{u}} + \frac{\partial}{\partial y} \overline{v\underline{u}} + \frac{\partial}{\partial z} \overline{w\underline{u}} + f_o \underline{k} \times \bar{\underline{u}} = - \frac{1}{\rho_o} \nabla_H \bar{p}. \quad (33)$$

In the particular case of horizontal homogeneity at large scales, the two components of equation (33) reduce to:

$$\frac{\partial \bar{u}}{\partial t} - f_o \bar{v} = - \frac{\partial}{\partial z} \overline{uw}, \quad (34)$$

$$\frac{\partial \bar{v}}{\partial t} + f_o \bar{u} = - \frac{\partial}{\partial z} \overline{vw}, \quad (35)$$

where the Reynolds stresses \overline{uw} and \overline{vw} are defined by (7) and (8).

Subtracting from (31) and (32) the continuity equations (19) and (20) pre-multiplied by \underline{u}' and \underline{u}'' , respectively, and assuming that the vertical advection terms dominate (preliminary remark), one obtains:

$$w' \frac{\partial}{\partial z} \underline{u}' = E(\underline{u}'' - \underline{u}'), \quad (36)$$

$$w'' \frac{\partial}{\partial z} \underline{u}'' = E(\underline{u}'' - \underline{u}'). \quad (37)$$

$$w'' \frac{\partial}{\partial z} \underline{u}'' = E(\underline{u}'' - \underline{u}'). \quad (37)$$

By use of (22), the difference of these two equations leads to:

$$(1-f)\frac{\partial}{\partial z} u' + f\frac{\partial}{\partial z} u'' = 0, \quad (38)$$

which is comparable to (30).

f) Vertical momentum equation:

In the context of Boussinesq approximations (Spiegel and Veronis, 1960), densities may be approximated by the reference density ρ_0 everywhere except in the buoyancy terms where actual values have to be kept. For two interacting fluids, the vertical momentum equations are:

for thermals:

$$\begin{aligned} & \frac{\partial}{\partial t}(fw') + \frac{\partial}{\partial x}(fu'w') + \frac{\partial}{\partial y}(fv'w') + \frac{\partial}{\partial z}(fw'w') \\ & = -\frac{1}{\rho_0}\frac{\partial}{\partial z}(fp') - \frac{g}{\rho_0}f\rho' + \frac{1}{2}E(w'+w''), \end{aligned} \quad (39)$$

for anti-thermals:

$$\begin{aligned} & \frac{\partial}{\partial t}((1-f)w'') + \frac{\partial}{\partial x}((1-f)u''w'') + \frac{\partial}{\partial y}((1-f)v''w'') + \frac{\partial}{\partial z}((1-f)w''w'') \\ & = -\frac{1}{\rho_0}\frac{\partial}{\partial z}((1-f)p'') - \frac{g}{\rho_0}(1-f)\rho'' - \frac{1}{2}E(w'+w''). \end{aligned} \quad (40)$$

The sum of these two equations yields an equation for mean quantities:

$$\frac{\partial}{\partial t} \overline{w} + \frac{\partial}{\partial x} \overline{uw} + \frac{\partial}{\partial y} \overline{vw} + \frac{\partial}{\partial z} \overline{ww} = -\frac{1}{\rho_0} \frac{\partial \overline{p}}{\partial z} - \frac{g}{\rho_0} \overline{\rho}. \quad (41)$$

The main balance consists of the terms on the right-hand side, i.e., the hydrostatic balance. The fourth term dominates the left-hand side, because w' and w'' do not cancel their effect in the correlation \overline{ww} and vertical advection dominates. Using (13) and (22), the same, because w' and w'' do not cancel their effect in the correlation \overline{ww} and vertical advection dominates. Using (13) and (22), the Reynolds stress \overline{ww} is found to be equal to w_{rms}^2 , and (41) may be

rewritten as:

$$\frac{1}{\rho_0} \frac{\partial \bar{p}}{\partial z} = -\frac{g}{\rho_0} \bar{\rho} - \frac{\partial}{\partial z} w_{rms}^2, \quad (42)$$

which simply is the hydrostatic relation corrected by the Reynolds stress divergence. To obtain an equation governing the vertical motions, this equation will be subtracted from (39), and this correction will become of the same order as the remaining terms.

A vertical velocity equation is needed in order to predict vertical motions through the convective layer. That equation, obtained by subtracting (42) multiplied by f from equation (39), using (13), (22), (23), and assuming once again that vertical advection is the dominant term of the total time derivative (preliminary remark), is:

$$\begin{aligned} & 3m w_{rms} \frac{\partial w_{rms}}{\partial z} + \frac{2m}{1-2f} \left(\frac{\bar{p} + m\bar{p}}{\rho_0} - (1+m^2) w_{rms}^2 \right) \frac{\partial f}{\partial z} \\ & = \alpha g T_{rms} - \frac{1}{\rho_0} \frac{\partial}{\partial z} p_{rms}, \end{aligned} \quad (43)$$

where m is a coefficient dependent on f only, defined by:

$$m = \frac{1-2f}{2[f(1-f)]^{1/2}}. \quad (44)$$

This diagnostic equation controls the vertical motion of thermals and anti-thermals. It relates the vertical acceleration to the buoyancy. The pressure term allows an exchange of kinetic energy between horizontal and vertical motions. The equation finally includes a correction term due to eventual changes in f .

includes a correction term due to eventual changes in f .

g) Need for a closure hypothesis:

In the above set of governing equations, the unknown variables are u' , u'' , \bar{u} , v' , v'' , \bar{v} , w' , w'' , \bar{w} , T' , T'' , \bar{T} , p' , p'' , \bar{p} , f , and E . There are thus 17 variables for which 17 equations are needed.

The definitions of mean values \bar{u} , \bar{v} , \bar{w} , \bar{T} , and \bar{p} [(1), (2), (3), (4), and (6)] yield 5 equations. The two continuity equations (19) and (20) may be equivalently replaced by (22) and (23). The heat conservation equations (24) and (25) may be replaced by (26) and (30), the horizontal momentum equations (31) and (32) by (33) and (38), the vertical momentum equations (39) and (40) by (42) and (43). Since the horizontal momentum are two-dimensional, there are $5+2+2+4+2 = 15$ independent definitions and governing equations. One needs thus two extra equations to solve the problem for the 17 variables. A closure hypothesis will provide the first one, while an examination of the energetics will provide the second one.

6. CONSERVATION OF FRACTION OF AREA OCCUPIED BY THERMALS

Where thermals accelerate, they tend to separate vertically and to grow by entraining surrounding fluid (Turner, 1973, Chap. 6 and 7; Scorer, 1978, Chap. 8). Isolated thermals may grow freely, but in presence of many others, they grow until they feel a strong return flow more and more confined to a reduced fraction of area. This return flow will tend to erode the thermals, preventing them from growing any further, and a saturation equilibrium takes place. This return flow will tend to erode the thermals, preventing them from growing any further, and a saturation equilibrium takes place. Inversely, the same equilibrium state does occur in regions where

Expand ϕ and ψ in powers of μ .

$$\begin{aligned}\phi &= \mu\phi_0 + \mu^2\phi_1 + \dots \\ \psi &= \psi_0 + \mu\psi_1.\end{aligned}\tag{9}$$

The horizontal shear in the basic state is included in ψ_1 ; if it were in ψ_0 the problem would not be separable. We chose ψ_0 so that $q_{0Y} = 0$, where q_{0Y} is the lowest-order part of a quantity related to the meridional gradient of Ertel potential vorticity (see Charney and Stern, 1962). For convenience, the quantity q will be referred to as the potential vorticity.

$$q_{0Y} = \beta - U_{0XX} - U_{0YY} - \epsilon U_{0ZZ} - a_6 \epsilon U_{0Z} = 0,\tag{10}$$

where $U_0 = -\psi_{0Y}$.

Assume the solution has a wave-like form

$$\phi = \text{Re} \left\{ \hat{\phi}(Y, Z) \exp(ik(X - CT)) \right\}.\tag{11a}$$

This form is consistent with the X boundary conditions. The complex phase speed C is the eigenvalue in this problem so it is also expanded.

$$C = C_0 + \mu C_1 + \mu^2 C_2 \dots\tag{11b}$$

Substitute (9) - (11) into (8) and equate like powers in μ . At the $i + 1$ order in μ , a complex two-dimensional Poisson equation for $\hat{\phi}_i$ is obtained. The problem can be expressed as the $i + 1$ order in μ , a complex two-dimensional Poisson equation for $\hat{\phi}_i$ is obtained. The problem can be expressed as

$$\mathcal{L}(\hat{\phi}_i) \equiv \epsilon \hat{\phi}_{iZZ} + a_6 \epsilon \hat{\phi}_{iZ} - k^2 \hat{\phi}_i + \hat{\phi}_{iYY} = F_i,\tag{12a}$$

$$\mathbb{D}(\hat{\phi}_i) \equiv \hat{\phi}_{iZ} - \frac{U_0 Z}{U_0 - C_0} \hat{\phi}_i = B_i \quad \text{at } Z = 0, 1 \quad (12b)$$

$$\hat{\phi}_i = 0 \quad \text{at } Y = \pm Y_b. \quad (12c)$$

The differential operators \mathbb{L} and \mathbb{D} are defined by (12), where the "vertical" boundary conditions, $w = 0$ at the top and bottom, (12b) have been expressed using the adiabatic equation (5c). The meridional boundaries are located at $\pm Y_b$.

The lowest-order problem is homogeneous, that is, $F_0 = B_0 = 0$, and is solved in a fashion analogous to that used by Eady (1949). A Y dependence of $\hat{\phi}$ is chosen which satisfies (12c), reducing (12a) to an ordinary differential equation for the Z dependence of $\hat{\phi}$. The vertical boundary conditions (12b) provide the constant that links the two solutions of (12a) and prescribe C_0 .

A $\cos(mY)$ dependence upon Y will be chosen for the first-order solution; further, the meridional and zonal wavenumbers will be set equal, $m = k$. In order to satisfy the conditions (12c), the boundaries $\pm Y_b$ are placed where $\cos(mY)$ vanishes. Therefore, the position of the meridional boundaries is a function of wavelength.

To second- and higher-order, the Poisson equation and vertical boundary conditions are, in general, heterogeneous. The same differential operator appears on the left-hand sides of (12) at each order in μ , and it has a nontrivial homogeneous solution. Thus, the heterogeneous terms must satisfy an orthogonality condition in order to find a solution at the second and higher orders. Specifically, the heterogeneous terms must satisfy an orthogonality condition in order to find a solution at the second and higher orders. Specifically, the heterogeneous terms must be orthogonal to ϕ^* , the homogeneous solution

of the conjugate of the "total adjoint operator." The total adjoint operator includes the boundary and interior differential operations and is described in Appendix A. For this problem, the heterogeneous terms must be orthogonal to

$$\phi^* = \exp[a_0 Z] \hat{\phi}_0 .$$

The orthogonality condition is used to specify C_i for $i > 0$ and can be expressed as (see Appendix D):

$$C_i = \frac{\iint \phi^* F_i dY dZ - \int_{Z=0}^{Z=1} [\phi^* B_i^*] dY}{\left[\frac{U_{0Z}}{(U_0 - C_0)^2} \int_{Z=0}^{Z=1} \phi^* \hat{\phi}_0 dY \right]} , \quad (13)$$

where $B_i^* = B_i - \hat{\phi}_{0Z} C_i / (U_0 - C_0)$.

When C_0 is purely real, special care must be taken when evaluating (13). First, F_i will have a singular point along the Z integration path at the critical level where $U_0 = C_0$. Evaluating the singular integral by using the Cauchy Principal Value is apparently not appropriate. However, since we are interested in the growing modes and in order to avoid the singular point, we deform the contour of integration as if C_0 had a small positive imaginary part. The integrand is analytic and we deform the contour to the $\text{Im}(Z) < 0$ side of the pole. The justifications for this procedure are discussed in detail by McIntyre (1970). Second, where C_0 is purely real two solutions of different phase speed and vertical structure occur at lowest-order. In evaluating (13), we chose the slower moving of the two solutions since it is probably more relevant to this study. This

point is treated by Green (1960, p. 243). Note that the regions of the spectrum where C_0 is purely real will not be important and are not emphasized in this report.

Once C_i is obtained, $\hat{\phi}_i$ can be calculated. McIntyre (1970) solved the quasi-geostrophic form of the heterogeneous (12) in Cartesian coordinates by using Generalized Green's Functions for the Z dependence and employing an infinite transcendental function series for the Y dependence. In this study, direct numerical techniques are used which are computationally much faster and yet still highly accurate. This approach allows us to choose almost any reasonable profile for ψ , and to include the $O(\mu)$ ageostrophic terms with ease. The details of the numerical procedure are discussed in Appendix B.

Many of the results are presented here in nondimensional form. However, it is useful to mention the magnitudes of the scaling parameters used. From the static state we determine that $\kappa = .14$, $a_6 = -1$ and $H = 8.32$ km. The Rossby radius of deformation is chosen for the horizontal length scale, L . It can be determined⁴ by setting $\epsilon = 1$. If we choose a vertical scale $D = 10$ km and a mean Coriolis parameter $f_0 = 10^{-4} \text{ sec}^{-1}$ (which corresponds to a central latitude of 43.25° on the earth), then $L \approx 1100$ km. An appropriate length scale for a wave is the quarterwavelength, hence the model is suitable for describing waves of ~ 4500 km wavelength. A reasonable choice of β for this L and f_0 is $\beta = 1$. We choose a velocity scale $V = 22$ m/sec so that the Rossby number $\mu = .2$.

~~with D and f_0 is $\beta = 1$. We choose a velocity scale $v = 22$ m/sec so that the Rossby number $\mu = .2$.~~

⁴Note that ϵ is inversely proportional to the Richardson number. Define $Ri = gDK/V^2$ then $\epsilon^{-1} = Ri\mu^2 = 1$, thus $\epsilon = 1$ can be used to define the Rossby radius of deformation.

4. FIRST-ORDER SOLUTION

The solution of the lowest order form of (12) is discussed in this section. It is similar to a result obtained by Eady (1949) with modifications caused by the variable Coriolis parameter, compressibility and the geostrophic coordinates transformation.

If we assume that the Y dependence of ϕ_0 is given by $\cos(mY)$ and define

$$\hat{\phi}_0(Y, Z) = \cos(mY) \tilde{\phi}_0(Z)$$

then the first-order part of (12a) reduces to:

$$\tilde{\phi}_{0ZZ} + a_6 \tilde{\phi}_{0Z} - \alpha^2 \tilde{\phi}_0 = 0 \quad (14)$$

where $\alpha^2 = (m^2 + k^2)/\epsilon = 2k^2/\epsilon$ since we have set $m = k$. It is convenient to write the solution of (14) in the form

$$\tilde{\phi}_0 = e^{A_2 Z} \left[\cosh(A_1 Z) + A \cdot \sinh(A_1 Z) \right], \quad (15)$$

where $A_1 = 1/2(a_6^2 + 4\alpha^2)^{1/2}$ and $A_2 = -a_6/2$.

The solution (15) is valid up to an arbitrary multiplicative constant since (14) is linear; the remaining complex constants A and C_0 are determined from the vertical boundary condition:

$$\tilde{\phi}_{0Z} - \left[\frac{U_{0Z}}{U_0 - C_0} \right] \tilde{\phi}_0 = 0 \quad \text{at } Z = 0, 1. \quad (16)$$

$$\tilde{\phi}_{0Z} - \left[\frac{U_{0Z}}{U_0 - C_0} \right] \tilde{\phi}_0 = 0 \quad \text{at } Z = 0, 1. \quad (16)$$

From (15) and (16) evaluated at $Z = 0$,

$$A = \frac{-U_{oZ}(0)}{C_o A_1} - \frac{A_2}{A_1}. \quad (17)$$

Recall that the corresponding Eady (1949) result is $A = -U_o(0)/C_o \alpha$.

Using (15), (17) and (16) at $Z = 1$ the complex phase speed is found.

$$C_o = \frac{-b \pm (b^2 - 4ae)^{1/2}}{2a} \quad (18)$$

$$\text{where } a = \left(\frac{A_2^2}{A_1} - A_1 \right) \sinh(A_1)$$

$$b = \left[U_{oZ}(0) - U_{oZ}(1) \right] \cosh(A_1) + \left[U_o(1) \left(A_1 - \frac{A_2^2}{A_1} \right) + \frac{A_2}{A_1} (U_{oZ}(0) + U_{oZ}(1)) \right] \sinh(A_1)$$

$$e = -U_{oZ}(0) U_o(1) \cosh(A_1) - \left[\frac{U_{oZ}(0)}{A_1} (A_2 U_o(1) - U_{oZ}(1)) \right] \sinh(A_1)$$

While β does not appear explicitly in (14) - (18), it does appear implicitly in the definition of U_o .

$$U_o = \Lambda \left(e^{-a_6 Z} - 1 \right) + \frac{\beta Z}{a_6 \epsilon}. \quad (19)$$

This profile of U_o satisfies (10). It has westerly vertical shear that increases with height for the values of Λ chosen in this study. This profile of U_o satisfies (10). It has westerly vertical shear that increases with height for the values of Λ chosen in this study.

Fig. 2 shows two profiles of U_o , one for $\beta = 0$ ($\Lambda = .8$) and the other

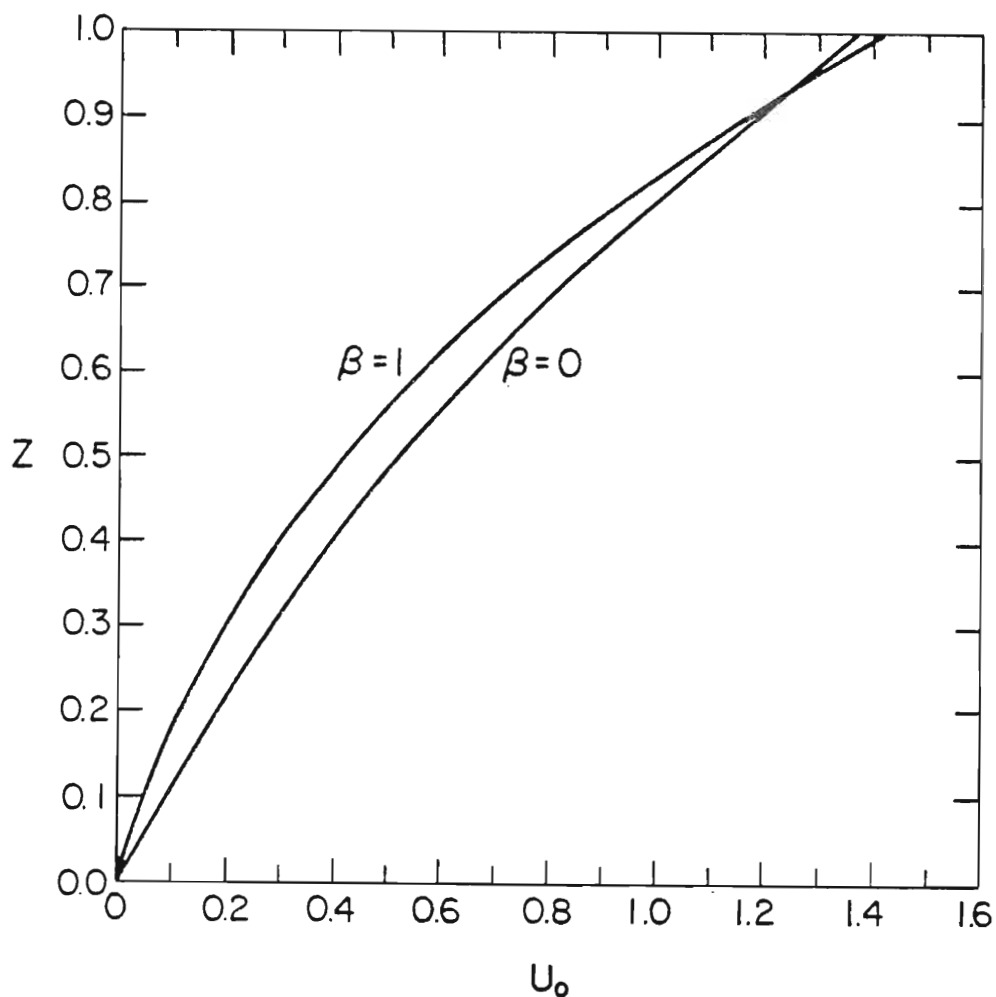


Fig. 2 The lowest-order basic state wind profiles, $U_0(Z)$ for $\beta = 0$ ($\Lambda = .8$) and for $\beta = 1$ ($\Lambda = 1.4$). In both cases $a_0 = -1$. The westerly vertical shear increases with height, but reaches a much larger maximum at $Z = 1$ in the $\beta = 1$ case. These profiles are used for the corresponding f -plane or β -plane experiments discussed in the remaining sections of this article.

cle.

for $\beta = 1$ ($\Lambda = 1.4$). These profiles will be used for the calculations of the second-order solutions when $\beta = 0$ or 1 , respectively.

The first-order growth rate and phase speed spectra for the basic state velocities shown in Fig. 2 are presented in Figs. 3 and 4, respectively. Since (18) is quadratic there are two modes. When C_0 is complex the two modes have the same phase speed and form an amplifying/decaying conjugate pair. The decaying mode is not considered. When C_0 is pure real the phase speeds differ. The solutions for $\beta = 0$ are analogous to the results of Eady (1949); the relatively minor differences for C_0 are due to the inclusion of compressibility. The inclusion of the variable Coriolis parameter induces two major effects. First, the amplitude of the phase speed and growth rate are diminished. Second, a long-wave cut-off to the instability is introduced. While β does not explicitly appear in (14) it does enter into (16) through (19). (Due to (10) and (12c), the solution is forced by the vertical boundaries.) The results for $\beta = 1$ are cognate with Green (1960, Fig. 2) except that critical layer instability as interpreted by Bretherton (1966b) is not possible, so a short-wave cut-off is also present at lowest order. As in Green, the low rigid lid makes β stabilize the solutions (see Lindzen et al., 1979).

The reduced propagation speed due to the nonzero β can be understood from the geopotential tendency equation. For $\beta \neq 0$ we have a nonvanishing planetary vorticity advection term. This term is positive east of the trough and negative west of the trough, which have a nonvanishing planetary vorticity advection term. This term is positive east of the trough and negative west of the trough, which is opposite to the contribution by the relative vorticity advection

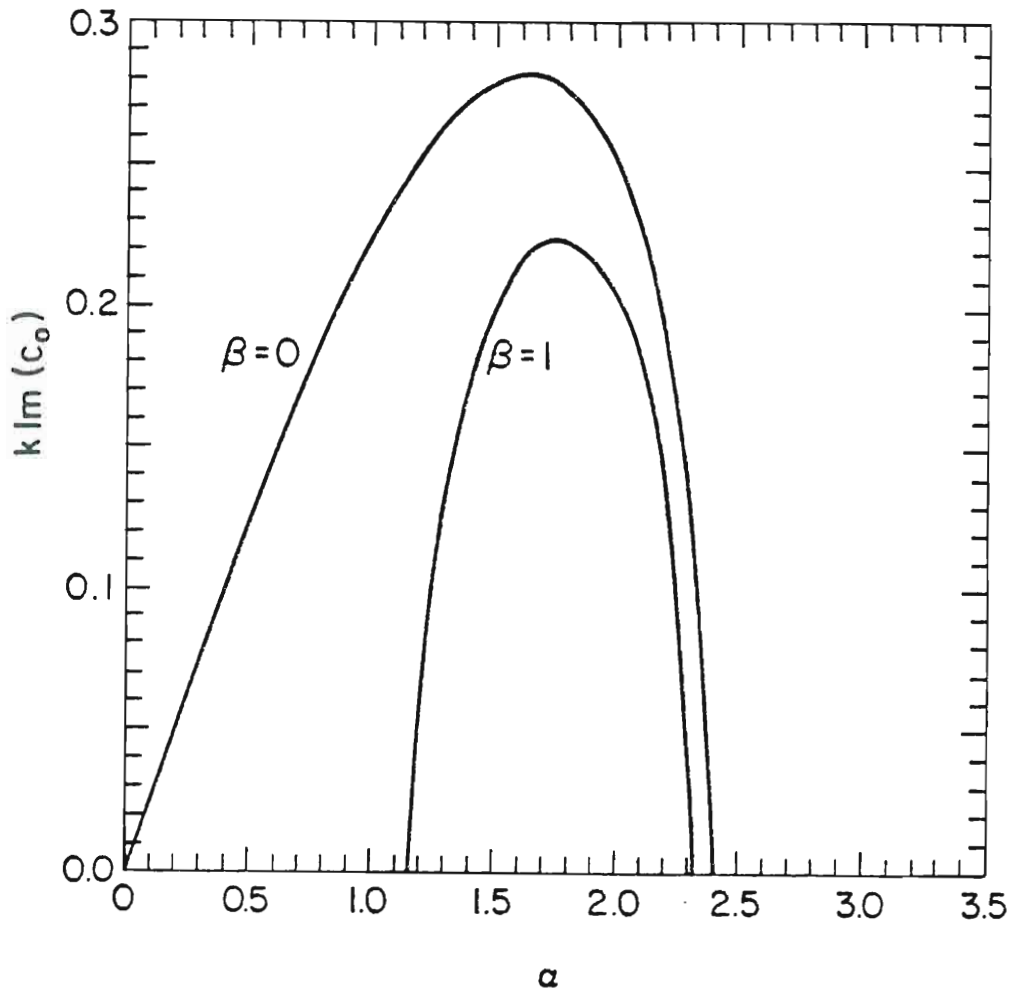


Fig. 3 Growth rate spectra for the two velocity profiles shown in Fig. 1. The parameter α is related to the wavenumber, $k^2 = \epsilon\alpha^2/2$. The maximum growth rate is less for the $\beta = 1$ than for the $\beta = 0$ profile. The variation of the Coriolis parameter also introduces a long-wave cut-off (near $\alpha \sim 1.2$) and the short-wave cut-off (near $\alpha \sim 2.4$) is shifted to a slightly smaller value of α . See the text for a more complete discussion of Figs. 3 - 6.

slightly smaller value of α . See the text for a more complete discussion of Figs. 3 - 6.

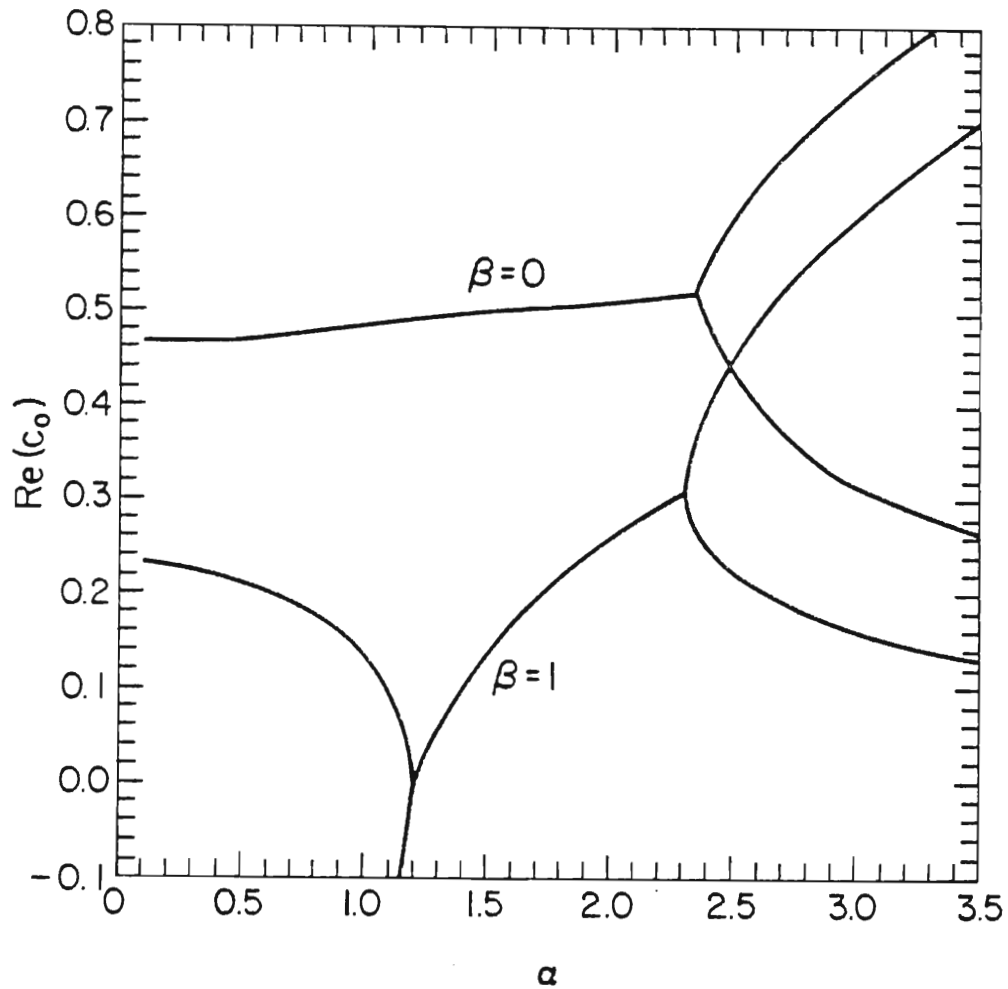


Fig. 4 Phase speed spectra for the two velocity profiles shown in Fig. 1. The f -plane profile is similar to the result obtained by Eady (1949) as was the growth rate spectrum shown in Fig. 3. The β -plane profile is similar to results obtained by Green (1960). The variable Coriolis formulation reduces the phase speed. Because (18) is quadratic, the phase speed is doubly valued for neutral waves.

obtained by Green (1960). The variable Coriolis formulation reduces the phase speed. Because (18) is quadratic, the phase speed is doubly valued for neutral waves.

term, indicating an input of retrograde motion. Since the relative vorticity decreases with wavenumber for a sinusoidal eddy, it is clear that this β -effect becomes more marked as the wavenumber decreases.

The medium-scale waves, those between the long- and short-wave cut-offs, have phase speeds and growth rates which are compatible with Green (1960). For $\beta = 1$, the most unstable wave, at $\alpha = 1.7$, has dimensional wavelength of ~ 5700 km, phase speed of ~ 4.5 m/sec and doubling time of ~ 1.8 days. Green's maximum growth rate was nearly unchanged by the inclusion of $\beta = 1$, which implies that the reduction of the maximum growth rate found here may be due primarily to the use of different velocity profiles. However, the presence of critical layer instability in Green's study may be masking a diminution of the growth rate caused by the nonzero β . In this model the planetary vorticity gradient stabilizes the long waves and it will be argued later that this stabilization extends to the middle waves, though the importance of the effect decreases with wavelength.

For the long waves, those longer than the long-wave cut-off, there are two neutral modes when $\beta \neq 0$. One solution moves swiftly retrograde and is comparable to the neutral Rossby wave found by Green in this range of α . The other long-wave mode corresponds to the weakly amplifying/decaying pair of slow-moving solutions found by Green (1960). Apparently, his solutions were unstable due to weak critical layer instability which is not possible to lowest-order here. Since we are interested in amplifying solutions, the slow-moving solution will be

used for the second-order computations where critical layer instability may occur.

Critical layer instability requires the presence of a basic state potential vorticity gradient, q_y , at a "critical level" defined as where $U_0(z) = \text{Re}(C_0)$. This condition is not satisfied at lowest-order because of (10). Bretherton (1966a) visualized the instability as follows. First, consider the meridional flux of basic state q to be a generation term for perturbation potential vorticity. Next, it can be shown that for an infinitesimal perturbation the flux is unbounded at a level where the eddy propagation speed equals the basic state flow. The total potential vorticity is conserved, so the critical layer flux must be balanced by a general growth of the disturbance, whose structure emphasizes a region where the potential vorticity gradient is of opposite sign. Within the mathematical construct of this type of perturbation problem, such an analysis seems appropriate; however, a different analysis may be required for a nonlinear problem. This question arises again in the next section.

For the short waves, those shorter than the short-wave cut-off, there are again two neutral modes which relate to the two solutions obtained by Eady (1949). The critical layer instability argument shows that only one of these two solutions is physically realizable for a given basic state with nonzero q_y . The predominant sign of the critical layer potential vorticity flux determines which solution is appropriate to conserve total potential vorticity. In this study, critical layer potential vorticity flux determines which solution is appropriate to conserve total potential vorticity. In this study, the potential vorticity gradient for the higher-order problem will be

primarily positive in the interior; thus only the slower solution can balance the critical layer flux. Green (1960) investigated an analogous situation. In his experiments the mean potential vorticity gradient was uniformly positive and he found an amplifying/decaying pair of modes which coincided with this slower mode. This slower mode will be used in the second-order calculations.

The growth rates and phase speeds are also presented as a function of $U_0(1)$ in Figs. 5 and 6, respectively. The values of β and a_6 are fixed in each figure, only Λ is varied. Since $U_0(0) = 0$, the magnitude of $U_0(1)$ is a gross estimate of the vertical shear. In general, as $U_0(1)$ increases, so do the growth rates and phase speeds as one would expect. We see that as the vertical shear increases, the long-wave cut-off is shifted to longer wavelengths for fixed β . There is also a minimum value of $U_0(1)$ below which all waves are stable when $\beta \neq 0$. For $\beta = 1$, the wavelength of maximum instability shifts to longer wavelengths as $U_0(1)$ increases in magnitude and asymptotically approaches the most unstable wavelength found for $\beta = 0$. The position of the short-wave cut-off is altered only when $\beta \neq 0$. When $\beta \neq 0$ the short-wave cut-off is asymptotically approached as the shear dominates the β -effect. All of these features of the growth rates (Fig. 5) are in qualitative agreement with the classical neutral stability curves derived from 2-layer models (e.g., Phillips, 1951) or with continuous models (e.g., Charney, 1974).

The mathematical reasons for the long- and short-wave cut-offs models (e.g., Charney, 1974).

The mathematical reasons for the long- and short-wave cut-offs are not easily deduced from this formulation. This is because the compressibility and variation of the Coriolis parameter enter into the

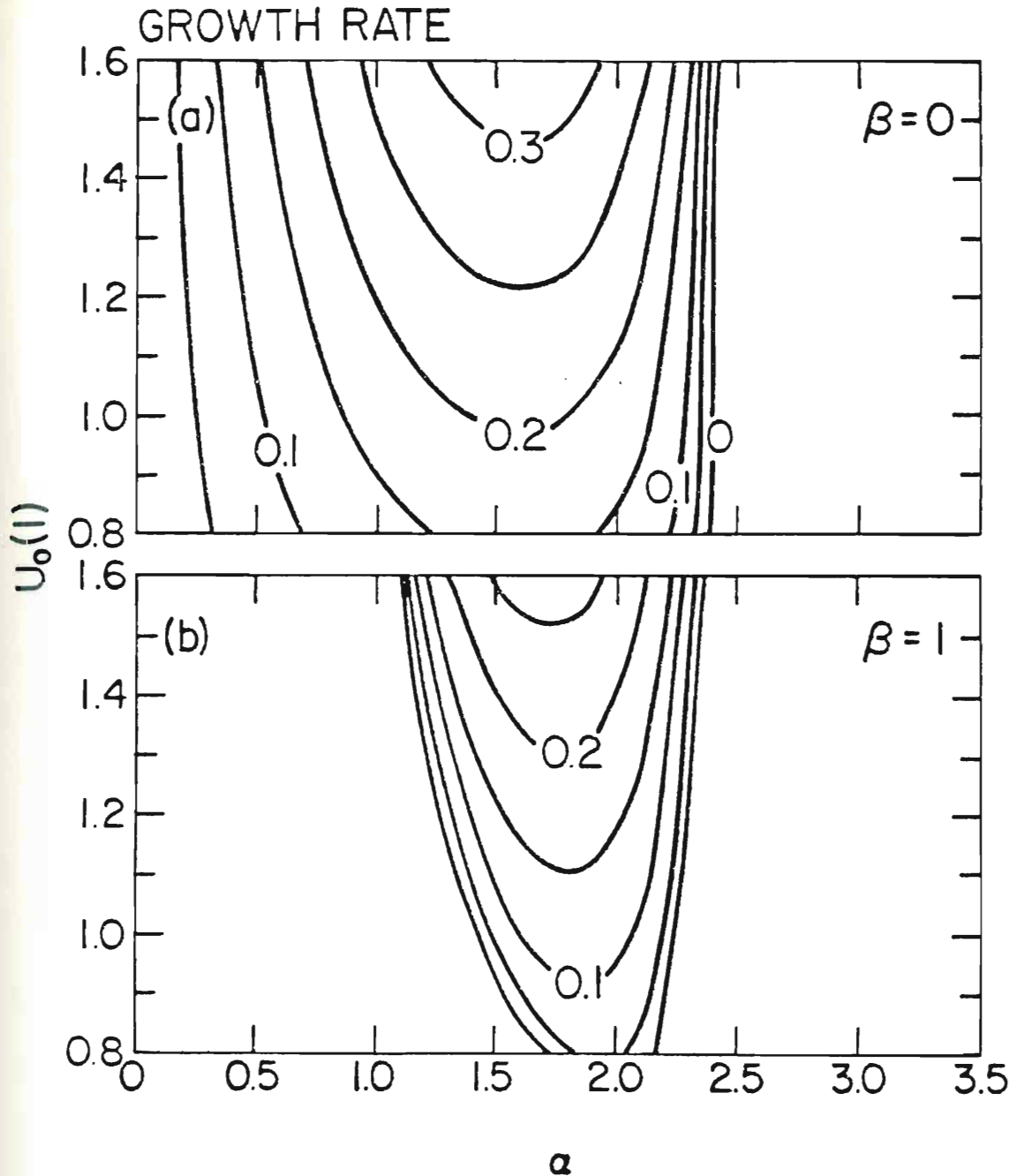


Fig. 5 The growth rate spectra for a) $\beta = 0$ and b) $\beta = 1$ versus $U_0(1)$. Only Λ is varied, $a_6 = -1$. Since $U_0(0) = 0$, $U_0(1)$ is a crude measure of the vertical shear. In general, the growth rate increases with $U_0(1)$. As the vertical shear increasingly dominates the β -effect the long-wave cut-off shifts to longer wavelengths and the short-wave cut-off approaches the $\beta = 0$ value.

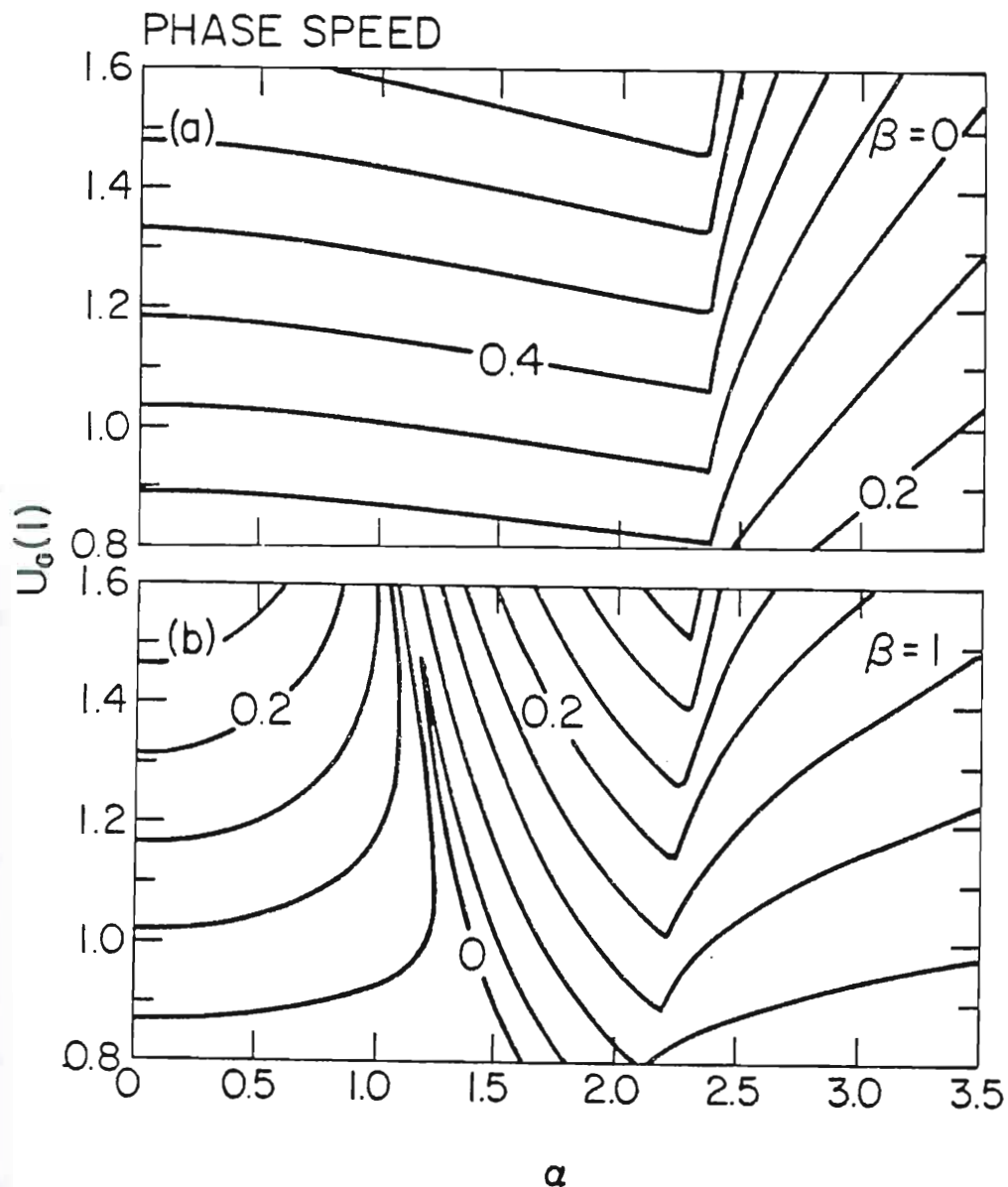


Fig. 6 The phase speed spectra for a) $\beta = 0$ and b) $\beta = 1$ versus $U_0(1)$, see Fig. 5. In general, the phase speed increases with $U_0(1)$. The major exception occurs near the long-wave cut-off and results from its shift to larger wavelengths with $U_0(1)$.

with $U_0(1)$. The major exception occurs near the long-wave cut-off and results from its shift to larger wavelengths with $U_0(1)$.

problem in a complicated fashion. Simpler previous investigations have succeeded in defining relations which describe the positions of similar cut-offs. These relations agree qualitatively with the behavior exhibited by the lowest-order solution. For example, Fjørtoft (1951) was able to determine a formula for the position of a correlative long-wave cut-off in his vertically continuous model. An expression for the short-wave cut-off is easily deduced for the 2-layer model (when $\beta = 0$) and a similar relation can be obtained here. Define L_c as the wavelength of the short-wave cut-off at $\alpha = \alpha_c$ so that $k = 2\pi L/L_c$. Then, using the definitions of α and ϵ , for $m = k$ and $\beta = 0$,

$$L_c = \frac{2\pi (2g\kappa D)^{1/2}}{\alpha_c f_0} \approx \frac{\pi (2g\kappa D)^{1/2}}{1.2 f_0} \quad (20)$$

which is quite similar to the 2-layer result. The critical wavelength increases with increasing static stability or decreasing mean planetary vorticity. But, observe from Fig. 5 that increasing β shifts the short-wave cut-off to longer wavelengths.

The physical reasons for the two cut-offs are qualitatively understood. The so-called advective theory of baroclinic instability (Fjørtoft, 1951) attempted to explain the short-wave cut-off in terms of parcel trajectories. The assumption was made that the horizontal scale of the disturbance becomes too small relative to the vertical, so that the slope of the trajectories exceeds the slope of the prescribed isotherms. Therefore, the eddy is unable to feed upon the so that the slope of the trajectories exceeds the slope of the prescribed isotherms. Therefore, the eddy is unable to feed upon the potential energy of the prescribed flow. However, this theory is

inadequate on several grounds. First, the position of the short-wave cut-off (for $\beta = 0$) is independent of the slope of the mean isotherms (see Fig. 5a). Second, as pointed out by Bretherton (1966b), the vertical structure changes for the short waves. This change compensates the decreasing horizontal scale by decreasing the vertical. A descriptive explanation of the short-wave cut-off has been inferred from 2-layer models (e.g., Holton, 1972, p. 190). Associated with a growing disturbance is differential vorticity advection which must increase with wavenumber for a given amplitude. This advection induces a so-called secondary circulation, whose vertical motions must also increase with wavenumber. But, the static stability resists these motions implying that sufficiently short waves will be stabilized. This stabilizing influence of static stability is evident in (20). By similar reasoning the inverse dependence of L_c upon f_0 in (20) results from the definition of the geostrophic velocities. Since the geostrophic velocities for a given geopotential field are less for larger f_0 , the thermal advection is less and so from the "omega" equation the induced vertical velocities are less. Since a weaker secondary circulation is present the cut-off is shifted to higher wavenumbers. The stabilizing effect of the planetary vorticity gradient, which introduces the long-wave cut-off and shifts the short-wave cut-off, can also be explained using the "omega" equation. However, this effect for non-zero β does not cause stability by itself, but instead occurs when instability is already present. Since However, this effect for non-zero β does not cause stability by itself, but instead occurs when instability is already present. Since the unstable waves tilt with height, there is differential planetary vorticity advection when β is nonzero, which increases the required

strength of the vertical velocities of the secondary circulation. Again, since the vertical motion is resisted, the result is a stabilizing effect. For this wave-like eddy the relative vorticity gradient varies as the wavenumber cubed, whereas β is constant; thus the planetary vorticity contribution to the "omega" equation dominates for the long waves. As β increases, the positions of the long- and short-wave cut-offs must shift since the slowest growing waves are most easily neutralized by the β -effect. Therefore, the short-wave cut-off shifts to longer waves and the long-wave cut-off shifts to shorter waves as β increases. The opposite shift occurs in Fig. 5b (where β is fixed and $U_0(1)$ increases) because the changing thermal field, associated with increasing Λ , alters the vertical structure of the eddy in a way which diminishes the importance of the planetary vorticity gradient.

The vertical structures of the transform pressure amplitudes are shown in Fig. 7 for the two velocity distributions of Fig. 2. The addition of compressibility and the consequent increase with height of the prescribed vertical shear cause the asymmetric distribution of pressure modulus. The vertical shears are about 3 and 7 times greater at the top than at the bottom for the $\beta = 0$ and $\beta = 1$ zonal flows, respectively. When C_0 is complex $\hat{\phi}_0$ is complex. The imaginary portion causes the vertical tilt of the trough and ridge axes toward the west with height. This tilt and the meridional structure are illustrated in Fig. 8 for $\alpha = 2.0$ and $\beta = 1$. west with height. This tilt and the meridional structure are illustrated in Fig. 8 for $\alpha = 2.0$ and $\beta = 1$.

Only baroclinic energy transformations are possible at lowest-order. The conversion from the basic state available potential energy

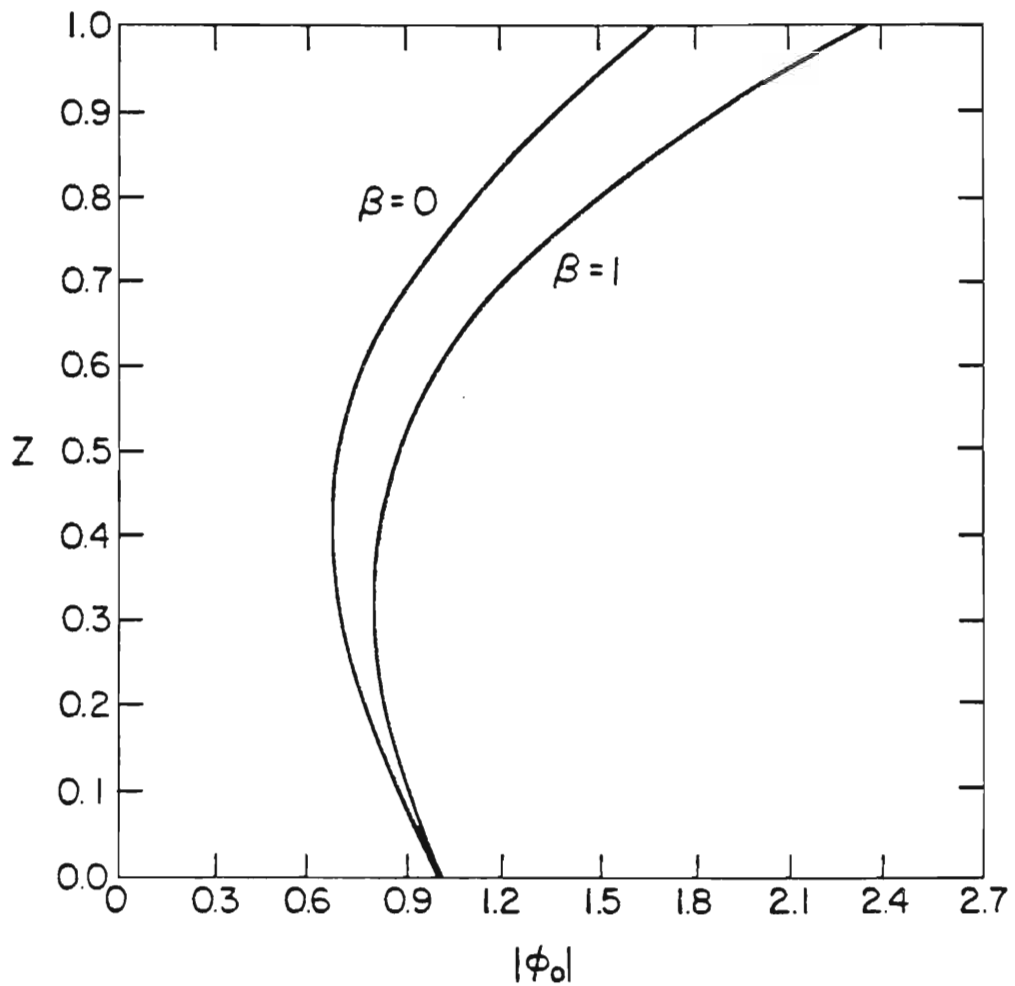


Fig. 7 The magnitude of the perturbation pressure solution at $\alpha = 2.1$ for each velocity profile shown in Fig. 2. The moduli are not symmetric with height because 1) the basic state vertical shear increases with height and 2) compressibility is included.

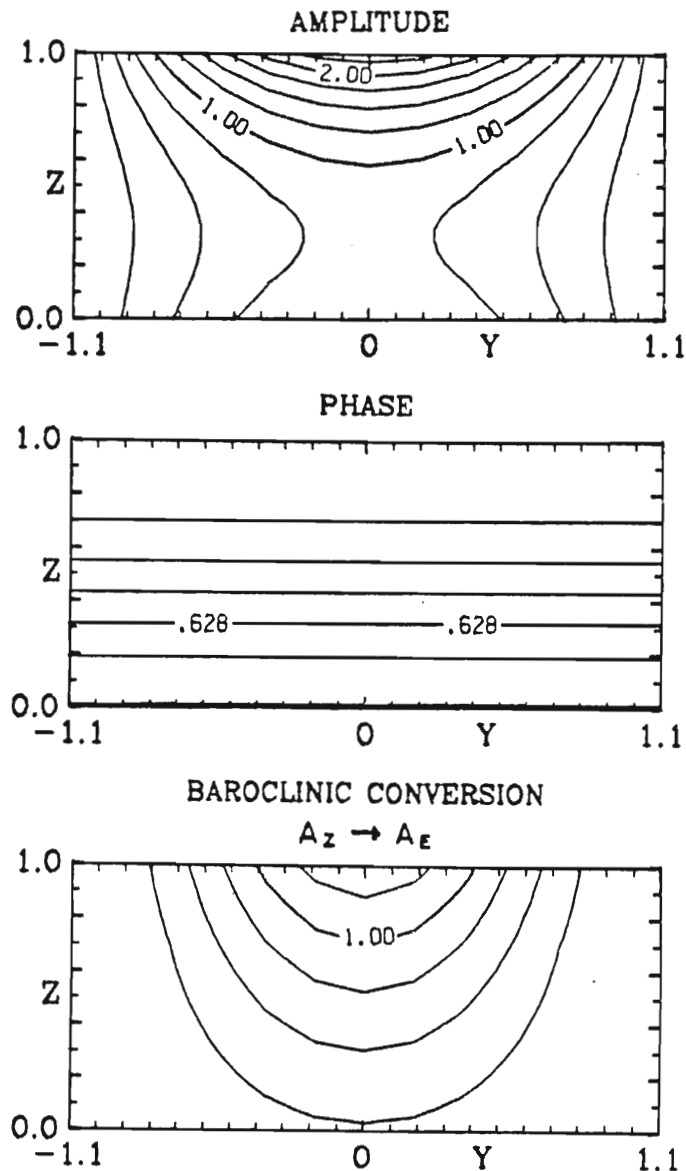


Fig. 8 Cross sections in geostrophic coordinates of the lowest-order eddy amplitude and phase of the pressure field and baroclinic conversion from zonal to eddy available potential energy for $\alpha = 2.0$ and $\beta = 1$. The phase diagram illustrates the meridionally uniform westward tilt with height of the trough and ridge axes. The phase angle is measured positive, eastward, relative to the value at the center top ($Y = 0$, $Z = 1$). The lowest-order amplitude and baroclinic conversion are largest at the center top. The lowest-order amplitude and baroclinic conversion illustrate the meridionally uniform westward tilt with height of the trough and ridge axes. The phase angle is measured positive, eastward, relative to the value at the center top ($Y = 0$, $Z = 1$). The lowest-order amplitude and baroclinic conversion are largest at the center top.

to the eddy available potential energy ($\overline{A_Z \rightarrow A_E}$) is also included in Fig. 8. This conversion is related to the poleward heat flux multiplied by the vertical shear of the zonal flow. At lowest-order the maximum occurs at the center top of the domain in geostrophic coordinates. The energy conversions will be discussed more thoroughly in the next section in reference to the energetics of the second-order quasi-geostrophic solutions.

In summary, compressibility has only a minor effect upon the quasi-geostrophic phase speed and growth rate as evidenced by the comparison of the $\beta = 0$ mode and Eady's (1949) result. However, it can have a significant impact upon the vertical structure of the disturbance. The variation of the Coriolis parameter has the large effects of reducing the phase speed and stabilizing the eddy. The stabilizing increases with the wavelength to such an extent that a long-wave cut-off of the instability is introduced. Because of the lack of critical layer instability, this formulation reproduces the short-wave cut-off found by Eady (1949). All these effects are evident in previous studies and are well-recognized if not well-understood.

5. SECOND-ORDER QUASI-GEOSTROPHIC SOLUTION

The stability, structure and associated energy conversions of the second-order quasi-geostrophic solutions are discussed in this section. The nonlinear distortion of the eddy by the transformation back to Cartesian coordinates is also examined. Solutions are considered for four basic state profiles with identical meridional structure but differing vertical variation.

The quasi-geostrophic system of equations is composed of the lowest-order terms in (8) and its boundary conditions. The ageostrophic effects that arise from the remaining terms in (8) and its vertical boundary conditions are described in the next section. The system of equations, (12), is no longer homogeneous but contains the forcing terms

$$F_1 = \hat{\phi}_0 \left\{ \epsilon \psi_{1ZZY} + a_6 \epsilon \psi_{1ZY} + \psi_{1YYY} \right\} / (C_0 - U_0) \quad (21)$$

in (12a) and

$$B_1 = \left\{ (C_1 + \psi_{1Y}) \hat{\phi}_{0Z} - \hat{\phi}_0 \psi_{1YZ} \right\} / (U_0 - C_0) \quad (22)$$

in (12b).

Four different $O(\mu)$ basic state profiles are used in this study.

The meridional dependence is the same for each profile:

The meridional dependence is the same for each profile:

$$\Theta_1 = G_Z(Z) \left\{ \lambda \tanh \left(\frac{aY}{\lambda} \right) - b_1 Y - b_2 Y^3 \right\} \quad (23a)$$

$$\psi_1 = G(Z) \left\{ \lambda \tanh(\underline{a}Y) - b_1 Y - b_2 Y^3 \right\} \quad (23a)$$

and

$$U_1 = G(Z) \left\{ \underline{a}\lambda(1 - \tanh^2(\underline{a}Y)) - b_1 - 3b_2 Y^2 \right\}$$

where $\lambda = T_{\max} / \tanh(\underline{a}Y_{\max})$. In three of the cases a maximum in the meridional gradient of the potential temperature field is present at $Y = 0$. This distribution, arising from the \tanh term in (24a), attempts to model a thermal front. For convenience, we will refer to this feature as a front. But it should be kept in mind that observed atmospheric thermal fronts are often more intense and of smaller width than can be treated with this analytic model. The intensity of the front is defined by the maximum value of the meridional gradient of potential temperature. The intensity and meridional scale of the frontal zone can be changed in a systematic fashion by varying the parameter \underline{a} . As \underline{a} increases the intensity increases and the width decreases. The parameter λ serves to normalize the Y dependence so that the value of θ_1 at a large distance ($\pm Y_{\max}$) from the center of the domain is independent of \underline{a} . Thus, increasing \underline{a} represents adiabatic compression of the isotherms in the meridional dimension. The b_1 and b_2 terms act to control the magnitude of the $O(\mu)$ addition to the basic state. In the examples detailed here $T_{\max} = 2$, $Y_{\max} = 2.25$ (this $Y_{\max} \approx Y_b$ for $\alpha = 1.0$), $b_1 = 1.1$ and $b_2 = .03$. The vertical structure, given by $G(Z)$, distinguishes the four cases. In one case the basic state thermal front is confined to $\rho_2 = .03$. The vertical structure, given by $G(Z)$, distinguishes the four cases. In one case the basic state thermal front is confined to the lower portion of the domain. This case is labelled the "Surface Front" case. In another case, the front is independent of height;

this case is referred to as the "Deep Front" case. The third case has a front in the upper part of the domain and is called the "Upper Front" case. Finally, there is the "Barotropic" case where the U_1 wind field is independent of height and thus does not arise from a potential temperature field. In each case the velocity field is symmetric in Y with maximum value at $Y = 0, Z = 1$. The specific vertical prescriptions for the four basic state profiles are

$$\begin{aligned}
 G(Z) &= Z^2 && \text{(Upper Front Case)} \\
 G(Z) &= Z && \text{(Deep Front Case)} \\
 G(Z) &= 2Z - Z^2 && \text{(Surface Front Case)} \\
 G(Z) &= 1 && \text{(Barotropic Case)}
 \end{aligned}
 \tag{23b}$$

Note that $U_1(Z)$ for the Barotropic case is equivalent to $U_1(1)$ in the other cases. The vertical structures in (23b) are chosen so that $G(0)$ and $G(1)$ are independent of the three cases where a front is present. In summary, these specifications mean that differences between the basic states, for the three front cases and for various choices of \underline{a} , result from adiabatic stretching or compressing of the same large-scale potential temperature field in the vertical and horizontal, respectively.

The Surface Front case total prescribed velocity and thermal fields for $\underline{a} = 1.6$ and $\beta = 1$ are shown in Fig. 9. The vertical shear in U_1 is largest in the lower portion of the domain, associated with the limitation of the front to that region. These features are characteristic of the polar jet structure often observed near incipient wave-cyclone development in the atmosphere. Strong frontal zones extending through the entire troposphere, at least in some instances,

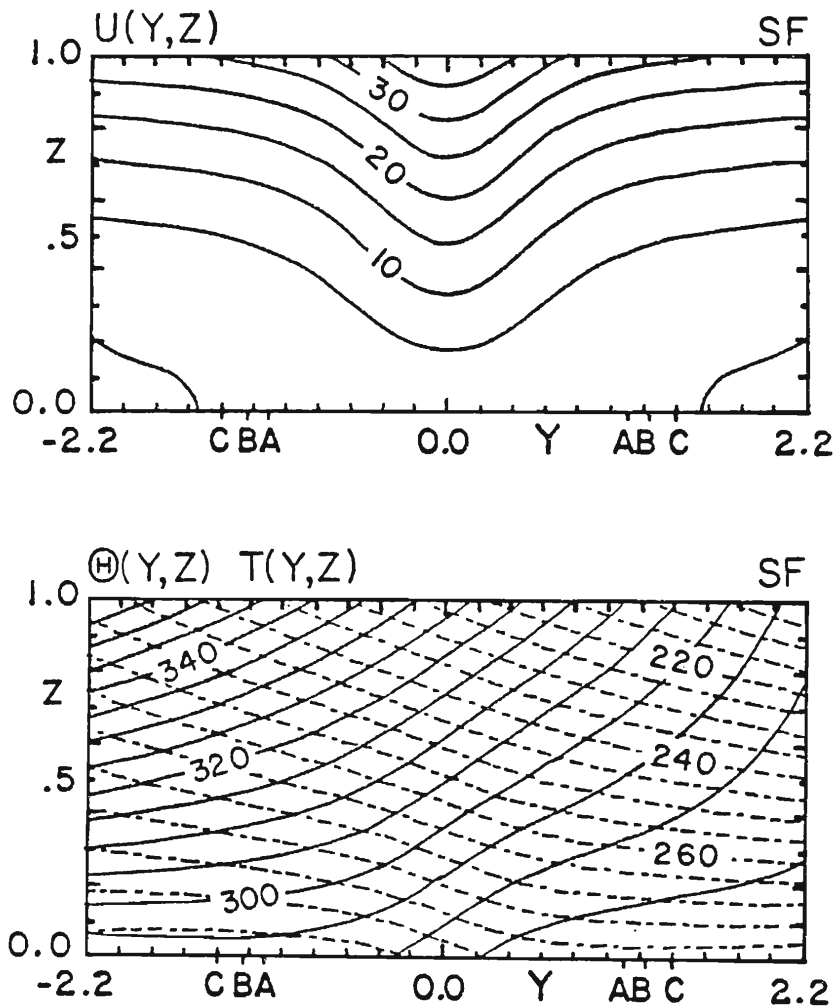


Fig. 9 Cross sections in geostrophic coordinates of the basic state zonal velocity (upper figure) and prescribed potential temperature; θ and temperature; T (lower figure) for the Surface Front case where $a = 1.6$. The prescribed thermal front in this case is confined near the bottom and has a width, for this value of a , which is close to the Rossby radius of deformation. The letters A, B and C denote the meridional boundaries for $\alpha = 2.0, 1.8$ and 1.6 , respectively.

boundaries for $\alpha = 2.0, 1.8$ and 1.6 , respectively.

form during rather than before cyclone development (e.g., Palmén and Newton, 1969, p. 338). The maximum velocity (40 m/sec) is also comparable in magnitude to that observed in the polar jet. The width of the frontal region for $\underline{a} = 1.6$ is approximately the Rossby radius of deformation. For $\underline{a} = .8$ the width is about twice this value. A significantly smaller scale cannot be handled by the model in its present form so solutions will be shown for the range $0 \leq \underline{a} \leq 2.0$. Those solutions at $\underline{a} = 1.6$ will receive primary attention.

The Upper Front case total prescribed velocity and thermal fields for $\underline{a} = 1.6$ and $\beta = 1$ are shown in Fig. 10. Here, the front is confined near the upper part of the domain where the basic state vertical shear is correspondingly largest. These features are characteristic of the subtropical jet under which wave-cyclones occasionally develop. The upper front is not as clearly visible as the surface front because of the exponential increase of U_0 with height. The Deep Front case, where the front is independent of height, is intermediate to Figs. 9 and 10.

In these experiments the basic state is independent of α , although the positions of the meridional boundaries change as indicated in Fig. 9. This is in contrast to Brown (1969a,b), who also examined flows with both vertical and horizontal shear but tied the meridional structure of his prescribed velocity field to the meridional wavelength of his solutions. He also used the procedure of fixing the available potential energy while varying the kinetic energy of the basic flow, his solutions. He also used the procedure of fixing the available potential energy while varying the kinetic energy of the basic flow, and vice versa. Here the temperature field at a large meridional distance is fixed and the adiabatic compression of the isotherms

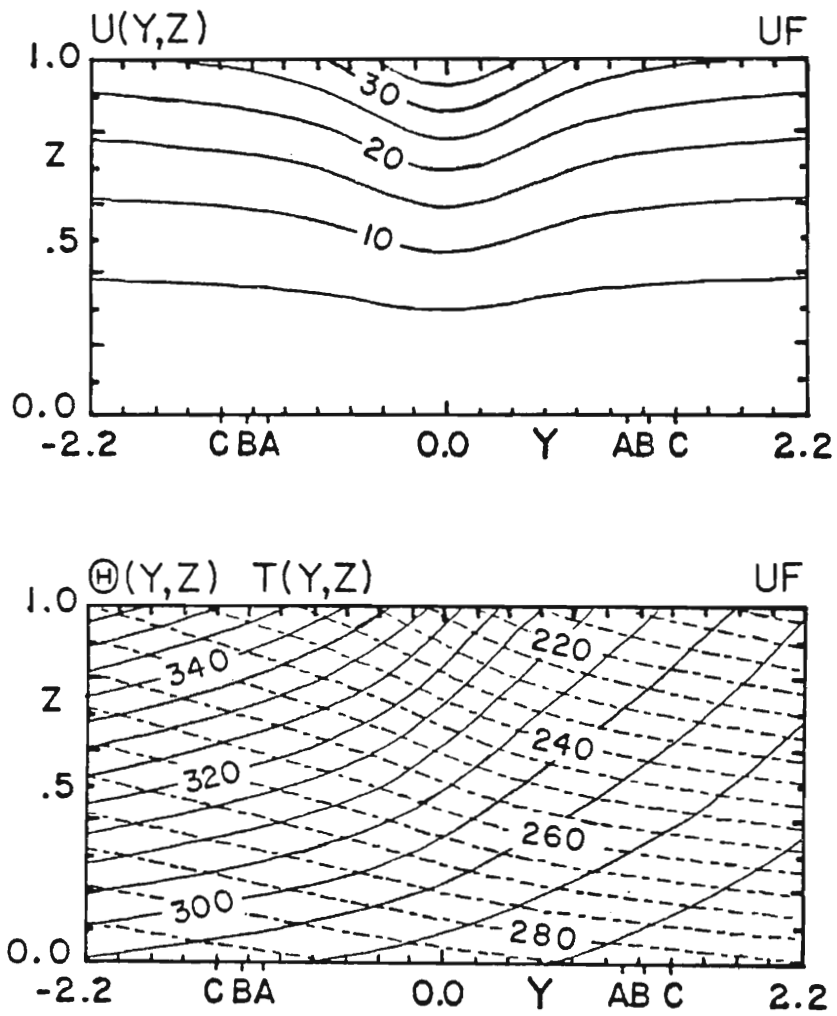


Fig. 10 Similar to Fig. 9 except for the Upper Front case where $\underline{a} = 1.6$. The thermal front in this case is confined near the top.

in Y and Z is varied. Like Brown (1969a,b), we chose flows which are presumed, by inspection of the potential vorticity gradient, to be barotropically unstable.

McIntyre (1970) discusses in some detail a solution derived from a barotropically unstable basic state. As a check upon the method of solution used in this model, a calculation was made using the same basic state profile discussed by McIntyre (1970). The two solutions were quite similar. The type of solution for this basic current will be examined again in connection with Fig. 21. (See Appendix I.)

The meridional potential vorticity gradient for each of the four basic states is presented in Fig. 11 for $\underline{a} = 1.6$ and $\beta = 1$. Because of (10), this gradient arises slowly from the $O(\mu)$ part of the basic state.

Fig. 12 displays the linear distortion by the coordinate transformation for the Surface Front case wind field shown in Fig. 9. Since there is no prescribed v field, the basic state only modifies the meridional dimension. A vertical feature in geostrophic coordinates acquires a poleward tilt with height when transformed back to Cartesian coordinates. Additionally, meridional asymmetry is introduced. The grid is stretched on the equatorward side and compressed on the poleward side of the velocity maximum. This implies that the relative vorticity is decreased on the equatorward side and increased on the poleward side. Such a change in the vorticity field induces a solenoidal circulation which would produce a poleward tilt of the velocity poleward side. Such a change in the vorticity field induces a solenoidal circulation which would produce a poleward tilt of the velocity maximum with height. This tilt is observed in the atmosphere for amplifying fronts. For an infinitesimal perturbation, the coordinate

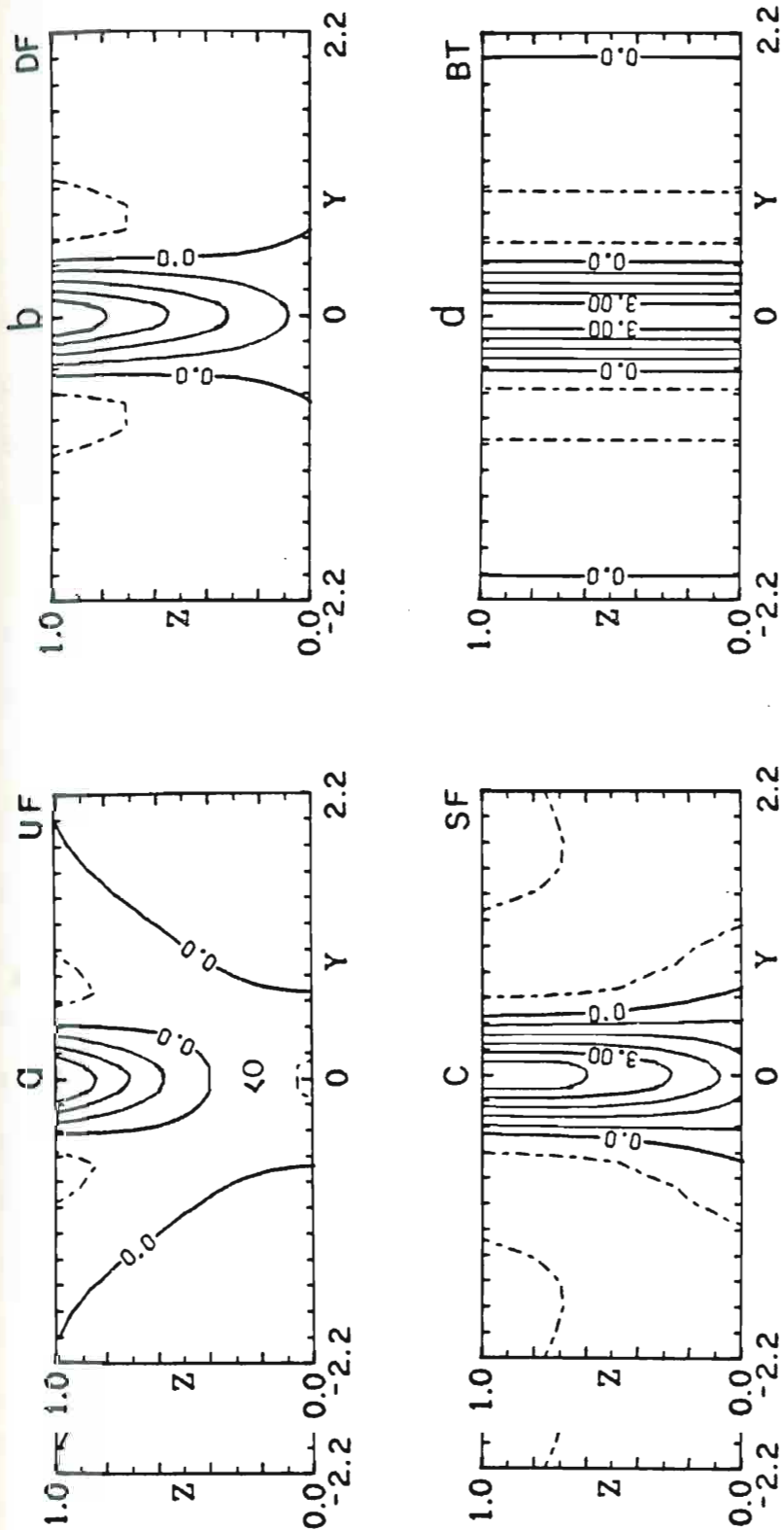


Fig. 11 Cross sections in geostrophic coordinates of the basic state potential vorticity gradient; q_y for the four cases examined in this article with $a = 1.6$. The four cases are a) Upper Front case case, b) Deep Front case, c) Surface Front case and d) Barotropic case (where U_1 is independent of Z). The four cases are distinguished by their vertical structure, the meridional variation is the same in each case. From (10) $q_y = 0$ at lowest-order, so $q_y = -\mu(U_{1YY} + a_6 \epsilon U_{1Z} + \epsilon U_{1ZZ})$. The large positive values centered about $Y = 0$ are mainly due to the U_{1YY} term.

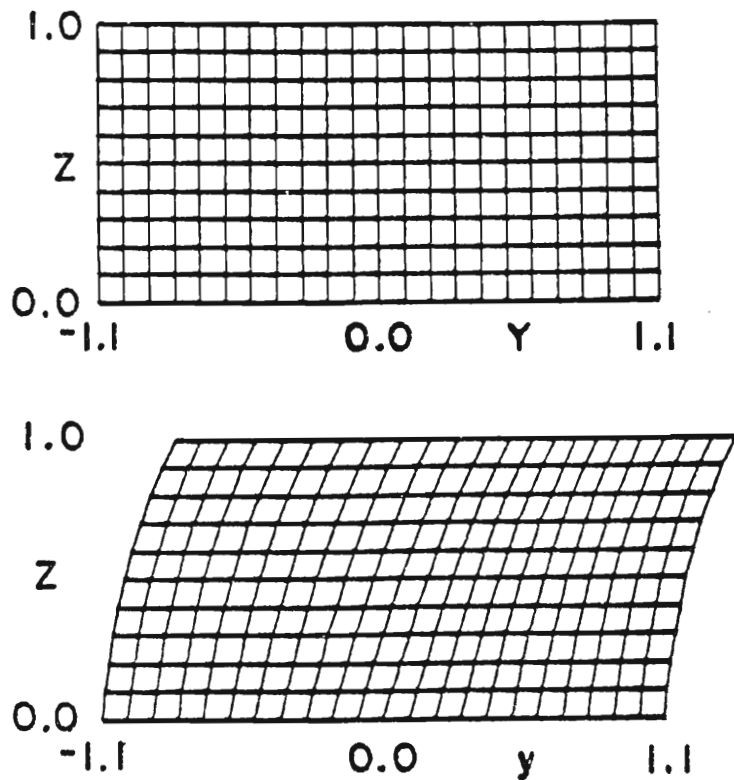


Fig. 12 An illustration of the linear distortion of a regular grid in geostrophic coordinates (upper diagram) by the coordinate transformation into Cartesian coordinates (lower diagram). Only the basic state zonal velocity (for the Surface Front case shown in Fig. 9) is used in this linear form of the coordinate transform. The meridional boundaries for $\alpha = 2.0$ are used in these figures. The transform introduces a poleward tilt with height. In the meridional dimension, the grid is stretched on the equatorward side of the velocity maximum and compressed on the poleward side. From (7c), this figure can be used to deduce how the distributions of several quantities in geostrophic coordinates appear in Cartesian coordinates when the eddy amplitude is very small.

several quantities in geostrophic coordinates appear in Cartesian coordinates when the eddy amplitude is very small.

transformation would be dominated by the basic state. This, along with (7c), means that Fig. 12 will be useful in interpreting the results of this chapter that are presented in geostrophic coordinates.

The remaining figures of the growth rates and phase speeds are divided into three regions according to the long- and short-wave cut-offs. The blank regions centered about those cut-offs are necessary because the denominator in (13) vanishes at the cut-offs. To obtain values at the cut-offs a different expansion procedure must be employed (see McIntyre, 1970). L'Hospital's rule is used to define U_1 and the ψ_1 terms in (21) and (22) for $\underline{a} = 0$.

The growth rates for the Upper Front and Deep Front profiles for $\beta = 1$ are presented in Fig. 13 as a function of α and \underline{a} . Nearly all the wavelengths are now unstable. Even the long waves are weakly unstable, in qualitative agreement with Green (1960). For the middle waves, the growth rates are negative for small values of \underline{a} . This damping is due to the b_1 term in (32a); for example, if $b_1 = .5$ is used instead of $b_1 = 1.1$, all the middle waves amplify over the entire range of \underline{a} . The growth rate for each wavenumber increases asymptotically to a specific value as \underline{a} increases. This behavior is more pronounced at smaller values of \underline{a} for smaller values of α . In addition, the shorter of the middle waves are more greatly destabilized than the longer of the middle waves. The net effect is a shift of the most unstable wave to shorter wavelengths as \underline{a} increases. The growth rates when $\beta = 0$ (not shown) are compatible, except that there is no unstable wave to shorter wavelengths as \underline{a} increases. The growth rates when $\beta = 0$ (not shown) are compatible, except that there is no long-wave cut-off, so features of the middle waves are "stretched" in α and extend into the long-wave portion of the spectrum.

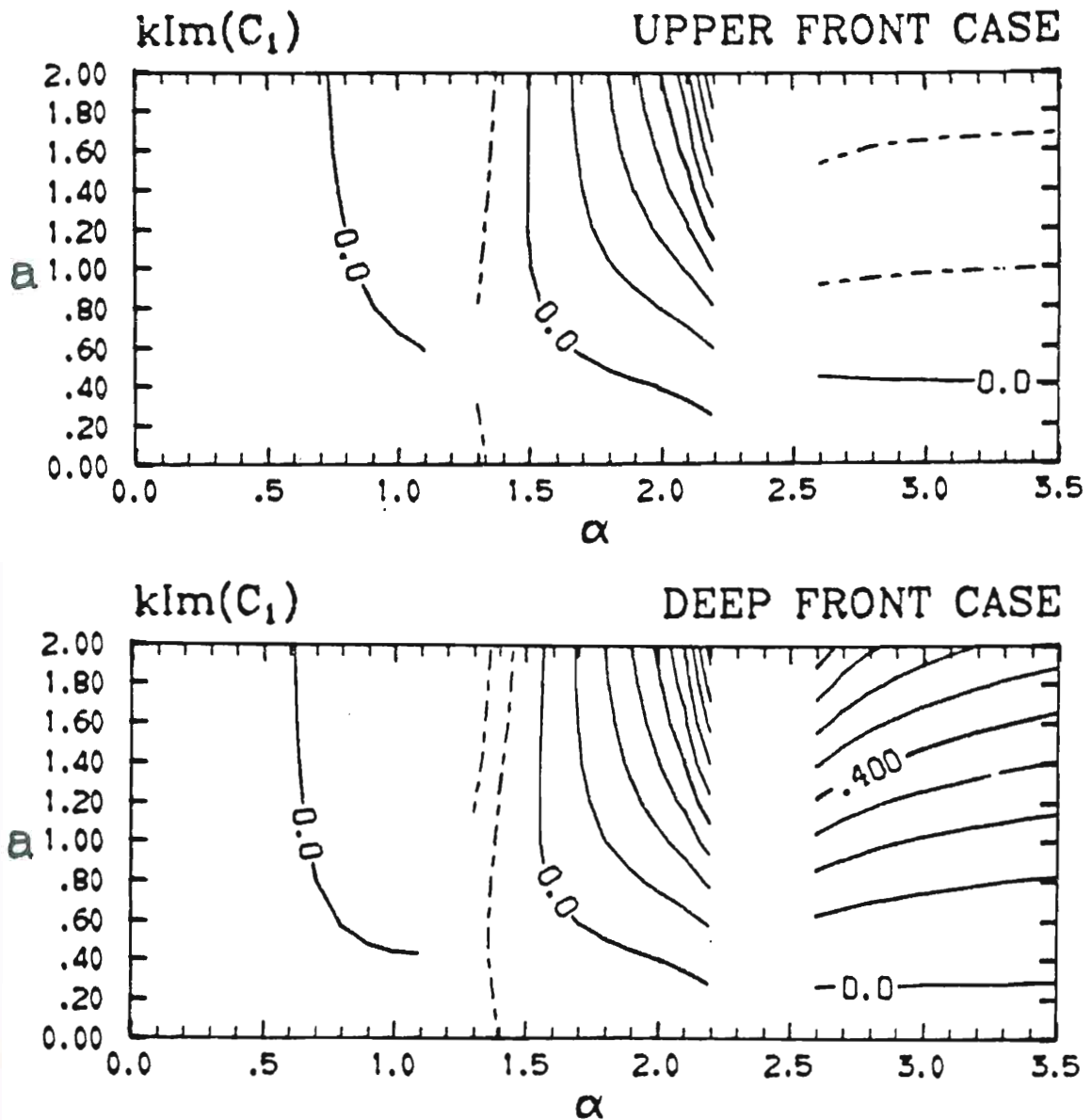


Fig. 13 Second-order growth rate spectra for the Upper Front and Deep Front cases for various α and \underline{a} , where $\beta = 1$. As \underline{a} increases, the intensity of the thermal front increases and its meridional scale decreases. For the middle waves, the growth rate generally increases with \underline{a} with the shorter waves more greatly destabilized by the front. Nearly all waves are destabilized, though the long waves are only weakly unstable. The blank regions are centered about the lowest-order instability cut-offs where (13) is singular. The contour interval in Figs. 13-16 is .1. See text for further interpretation of the second-order growth rates.

The growth rates for the Surface Front and Barotropic cases for $\beta = 1$ are presented in Fig. 14 as a function of α and \underline{a} . The Surface Front growth rates are consistent with the Upper Front and Deep Front results. However, the Barotropic case growth rates for the middle waves are dramatically different. The middle waves in the Barotropic case are all damped; and further, the damping increases with \underline{a} . This result seems odd because analysis of q_{1Y} indicates that the Barotropic case U_1 field should generally produce growth via the barotropic mechanism, and that the instability should increase with \underline{a} . This apparent dichotomy will be resolved when the energy conversions are examined later in this chapter.

The phase speeds for the Upper Front and Deep Front profiles when $\beta = 1$ are depicted in Fig. 15 as a function of α and \underline{a} . The phase speed spectra for the Surface Front and Barotropic cases are shown in Fig. 16. For the phase speed there is a definite trend between the four cases: from the Upper Front to the Barotropic. In general, for the middle waves the phase speed is negative, and the magnitude at first decreases then increases with \underline{a} .

The calculation of C_1 includes boundary and interior terms in (13). The real part of C_1 for the long and short waves is dominated by the boundary terms contribution.⁵ But, for the middle waves the interior terms contribution is of nearly equal magnitude and often of opposite sign. The negative values of the phase speed for small \underline{a} arise primarily from the boundary terms. As \underline{a} increases these terms of opposite sign. The negative values of the phase speed for small \underline{a} arise primarily from the boundary terms. As \underline{a} increases these terms

⁵The boundary terms contribution to the phase speeds and growth rates for these four cases are presented in Appendix I.

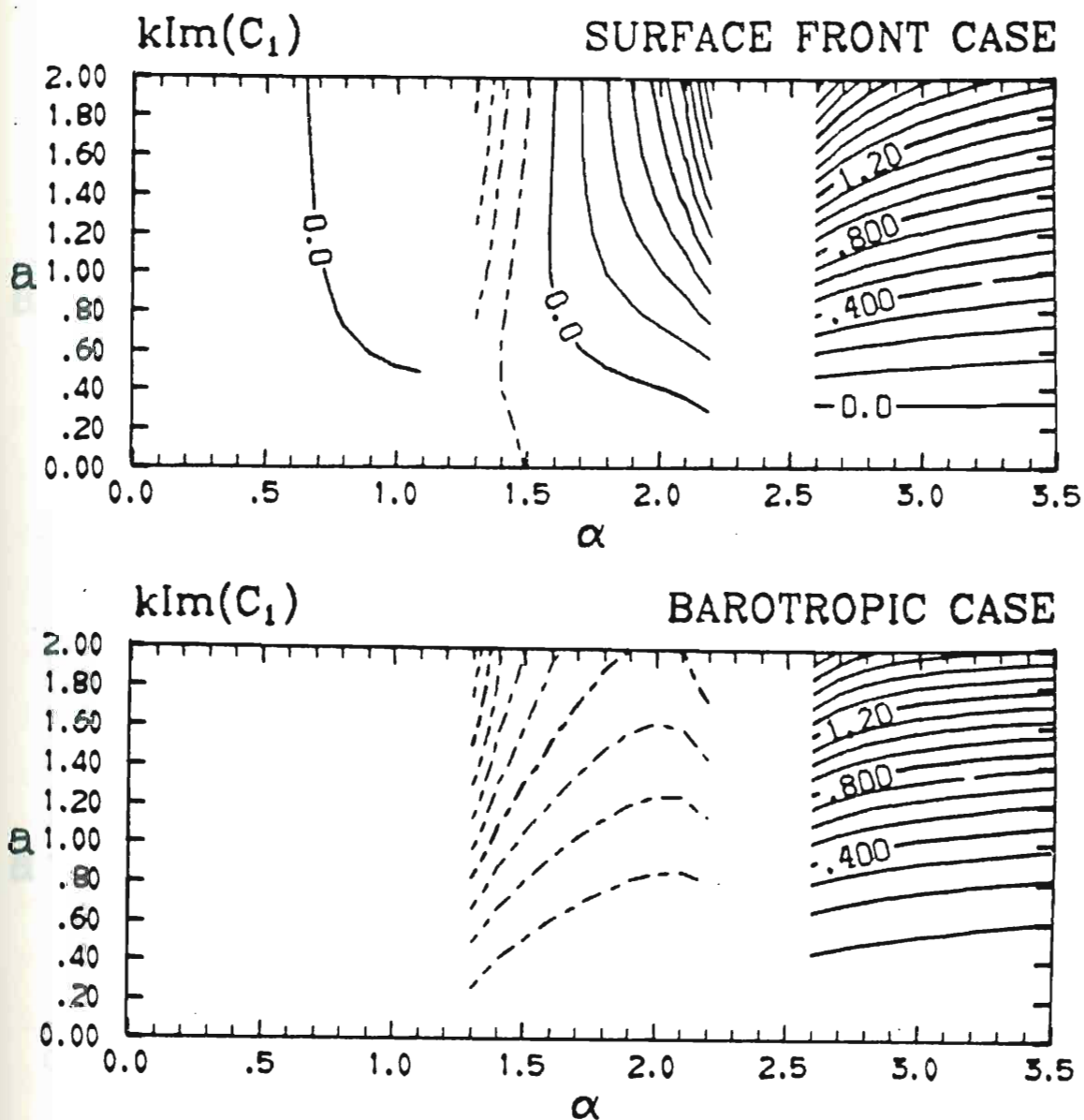


Fig. 14 Similar to Fig. 13 but for the Surface Front and Barotropic cases. The second-order growth rates for the middle waves in the Barotropic case are negative.

in the Barotropic case are negative.

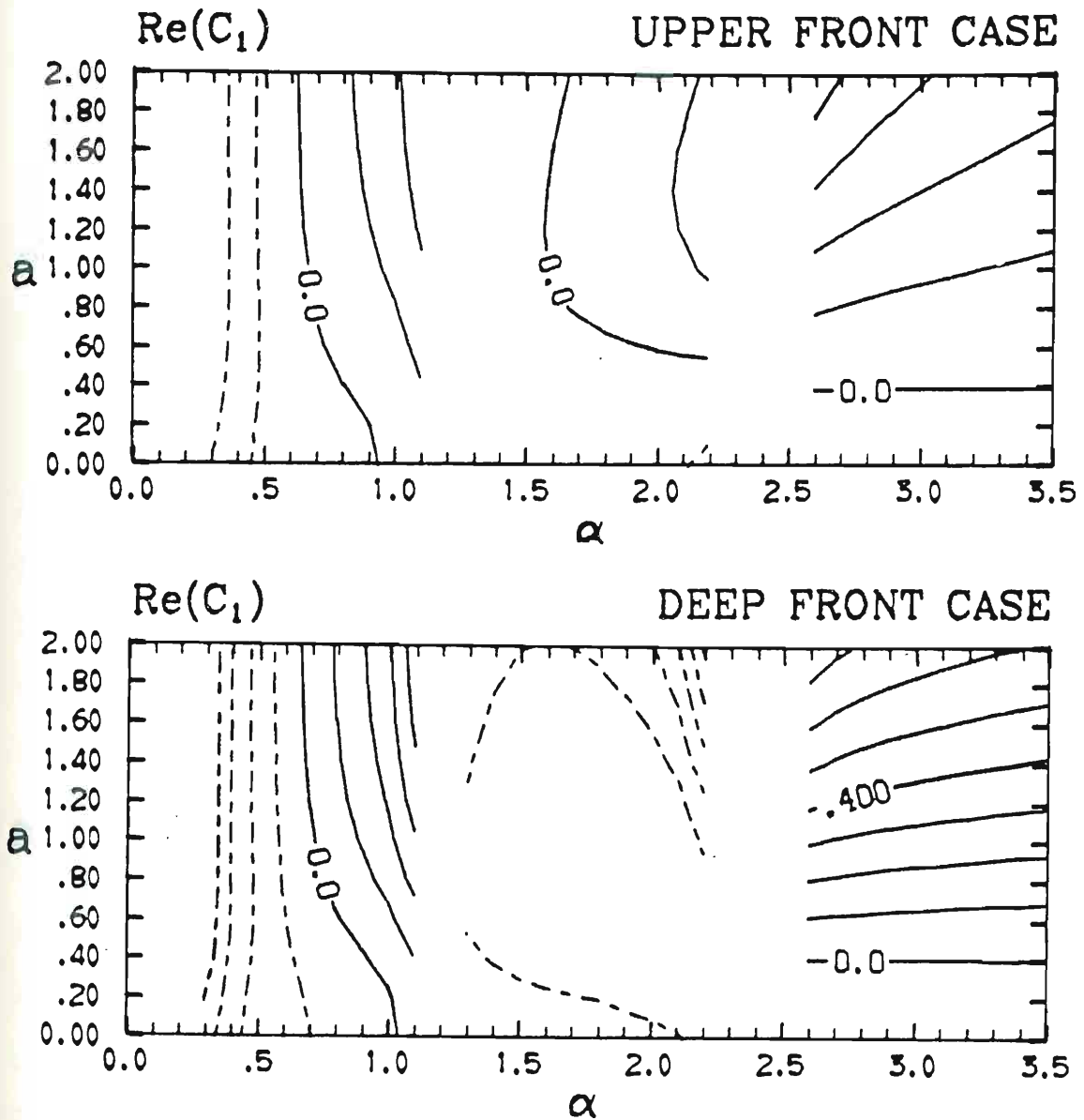


Fig. 15 Second-order phase speed spectra for the Upper Front and Deep Front cases. For the middle waves, the second-order phase speed is generally positive in the Upper Front case and negative in the other three. See text for further discussion of the second-order phase speed. For the middle waves, the second-order phase speed is generally positive in the Upper Front case and negative in the other three. See text for further discussion of the second-order phase speed.

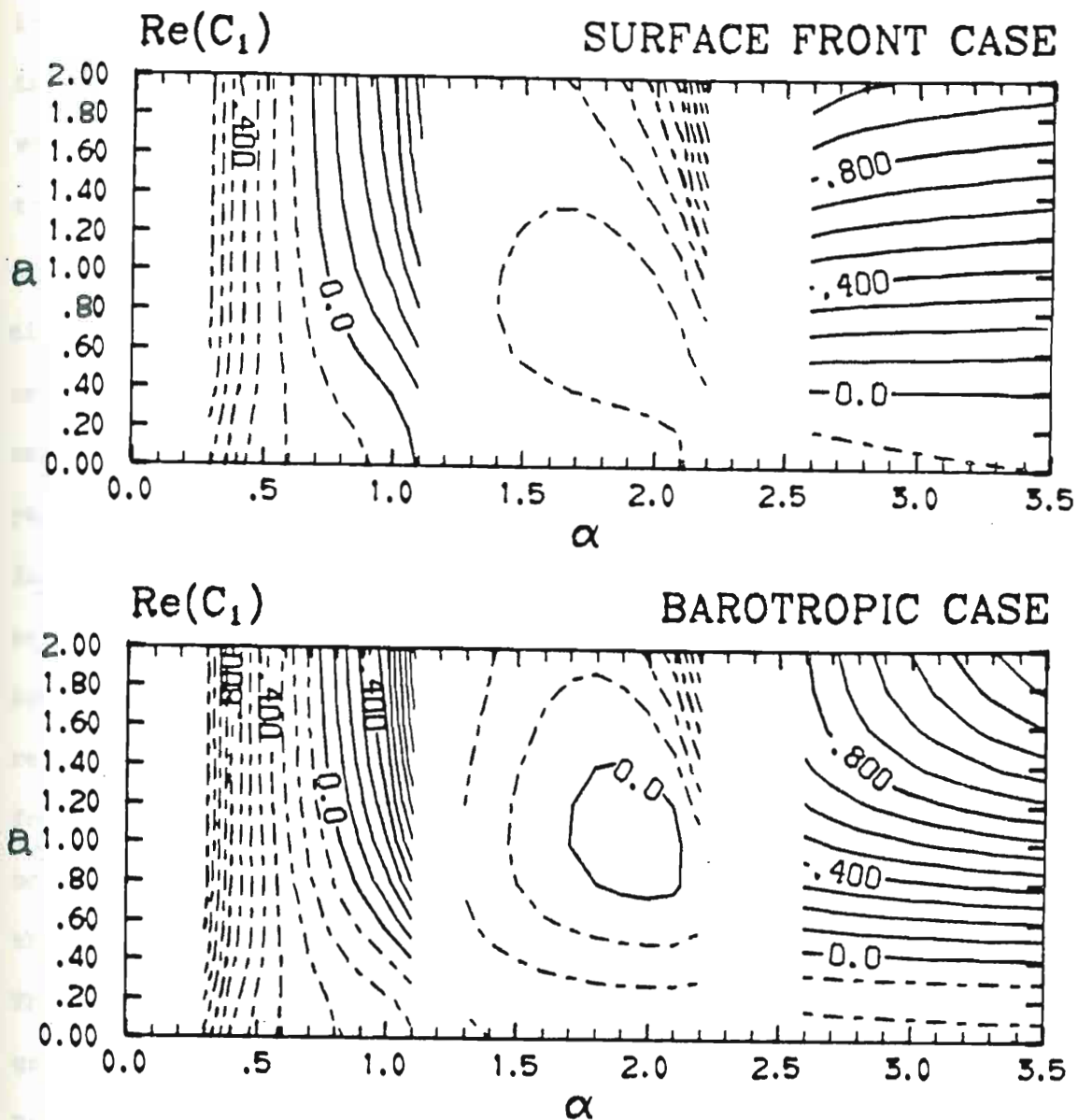


Fig. 16 Similar to Fig. 15 except for the Surface Front and Barotropic cases. There is a clear progression in the phase speed spectra from the Upper Front case to the Barotropic case.

fig. 16 Similar to Fig. 15 except for the Surface Front and Barotropic cases. There is a clear progression in the phase speed spectra from the Upper Front case to the Barotropic case.

become large and positive and also the interior terms become more important, especially the U_{1YY} portion. The positive values of the interior potential vorticity gradient (like the positive planetary vorticity gradient) act to reduce the total phase speed. The potential vorticity gradient in (22) is integrated over Y and Z in (13), so by inspection of Fig. 11 it is clear that the interior contribution is largest for the Barotropic case and least for the Upper Front case. Yet, the boundary terms contribution also becomes larger in complementary fashion. An analogous situation occurs for the growth rates. For the middle waves, the growth rates are almost the same for the three frontal cases, which might imply that the vertical structure of the front does not appreciably alter the stability of the eddy. In general, this is probably a specious conclusion since it relies upon the questionable vertical boundary condition at $Z = 1.$, for example. The boundary terms and interior terms in (13) each vary considerably between the four cases, but for the three frontal cases they fortuitously combine for the middle waves into similar spectra. The variation of the interior terms is exemplified by the short waves growth rates, to which the boundary terms do not contribute. In the Barotropic case only the U_{1YY} interior term contributes to the growth rate; the boundary terms happen to cancel for the middle waves. This term can cause damping for the middle waves and amplification for the short waves because the lowest-order vertical structures of the two classes of waves are different. This point will be treated more specifically when the energy conversions are examined.

A qualitative interpretation of the growth rate spectra for the short waves and, in particular, the negative growth rates for the Upper Front case, may be deduced from Bretherton (1966a). In essence, Bretherton shows that the potential vorticity, at a critical level, determines the instability of the short waves. Presumably, he defines the critical level as where $U(Y,Z) - \text{Re}(C)$ vanishes, where $U(Y,Z)$ is the total basic state velocity field and $\text{Re}(C)$ is the total phase speed. Mathematically, we can see that the interior integrand in (13) would tend to be largest at the height where $U_0 - C_0$ is very small. The critical level defined in this latter way is between $Z = .3$ and $Z = .15$ for the short waves and $\beta = 1$. By inspection of the basic state potential vorticity gradients in Fig. 11 we can qualitatively explain the growth rates calculated for the short waves. The contour of Z integration is the same in all cases, so the short waves in the Upper Front case are damped since the basic state potential vorticity gradient is predominantly negative near the critical level. In the other cases the gradient is primarily positive at the critical level. If we define the critical level as Bretherton did, then it is less certain that the calculated growth rates can be explained in this way.

The total growth rates and phase speeds are approximated by truncating their respective perturbation series after two terms. These approximate total values for the Surface Front case are shown in Fig. 17. To justify this approximation, some quick calculations of the third term in the series were made for a few key values of α and \underline{a} . 17. To justify this approximation, some quick calculations of the third term in the series were made for a few key values of α and \underline{a} . The results of these computations suggest that the general features of the total complex phase speed shown in Fig. 17 are unchanged by the

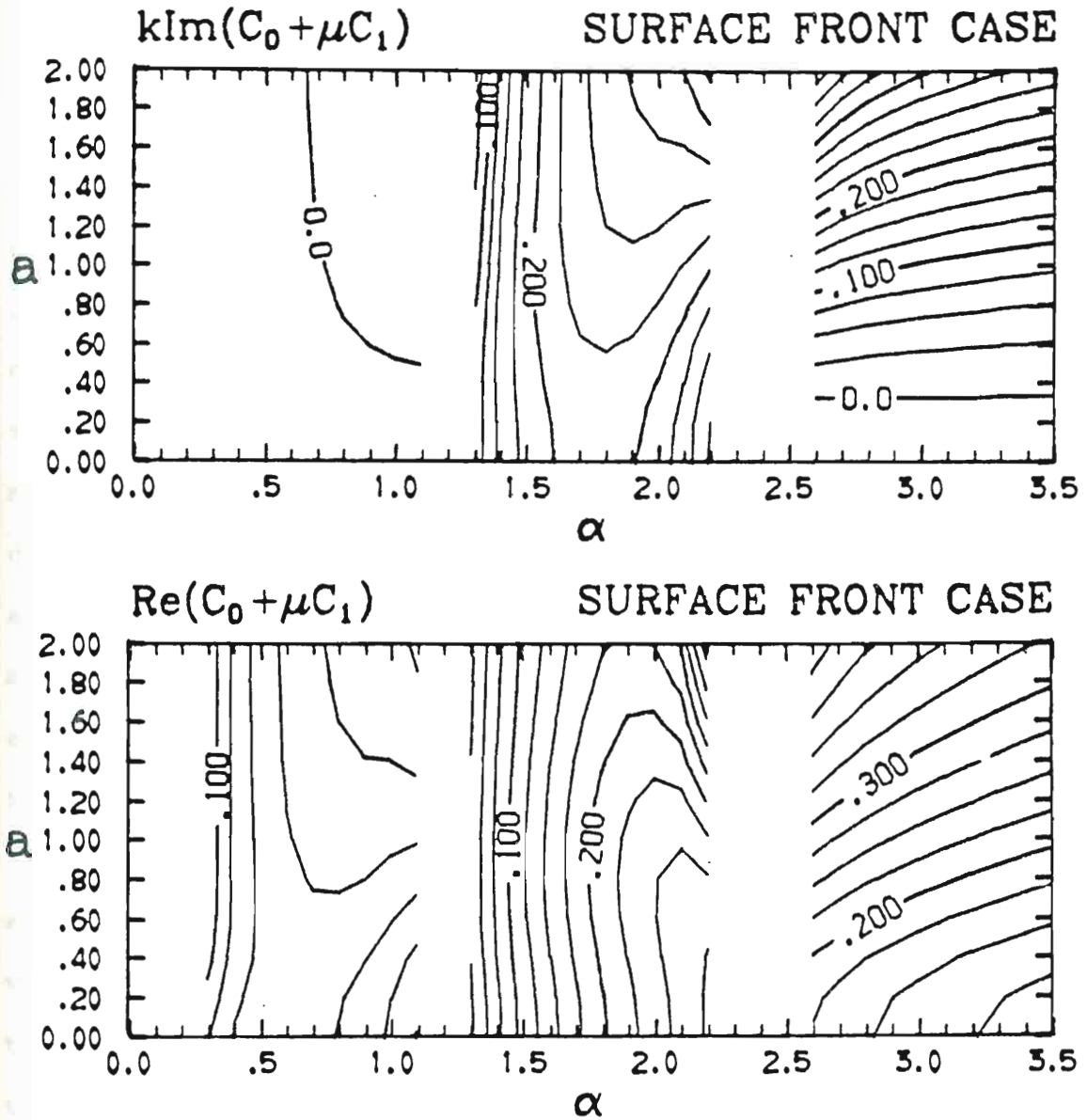


Fig. 17 The total growth rate (upper figure) and phase speed spectra (lower figure) for the Surface Front case. The shift of the most unstable wave to shorter waves as the meridional scale of the prescribed frontal zone decreases (as a increases) is evident in the upper diagram. As a increases, the fastest moving wave shifts to longer wavelengths.

higher-order terms.⁶ The shift of the most unstable wave to shorter wavelength as the meridional width of the frontal zone decreases is more clearly visible in this figure. The shift implies a convenient explanation for a discrepancy between the lowest-order solution and observed mid-latitude wave-cyclones. One presumes that the most unstable wavelength should roughly correspond with the observed wavelength of most cyclones. However, the most unstable wave at lowest-order has a wavelength of ~ 5700 km whereas atmospheric cyclones are typically 3-4000 km in wavelength. The ostensible link between the most unstable wavelength and the scale of the front suggests that this difference arises in part because a thermal front is present in the atmosphere, but not present to lowest-order in this model. For the middle waves, the total phase speed at first increases then decreases and the fastest moving wave has a longer wavelength as \underline{a} increases. Similar results are obtained for $\beta = 0$.

As for the most unstable wavelength, the meridional scale of the eddy also responds to the scale of the basic state front. It is convenient to define the meridional scale of the eddy in terms of the positions of the eddy zonal velocity maxima. These maxima are indicated by the + symbols in Fig. 18. This figure shows the surface eddy zonal velocity fields for the lowest-order solution and two total solutions computed for different values of \underline{a} . (In this treatise, the "total"

⁶ If anything, these calculations corroborate the effects introduced by the addition of the second term in the series to the first. The third term strengthens the phase speed maximum and the shift of the

⁶ If anything, these calculations corroborate the effects introduced by the addition of the second term in the series to the first. The third term strengthens the phase speed maximum and the shift of the most unstable wavelength.

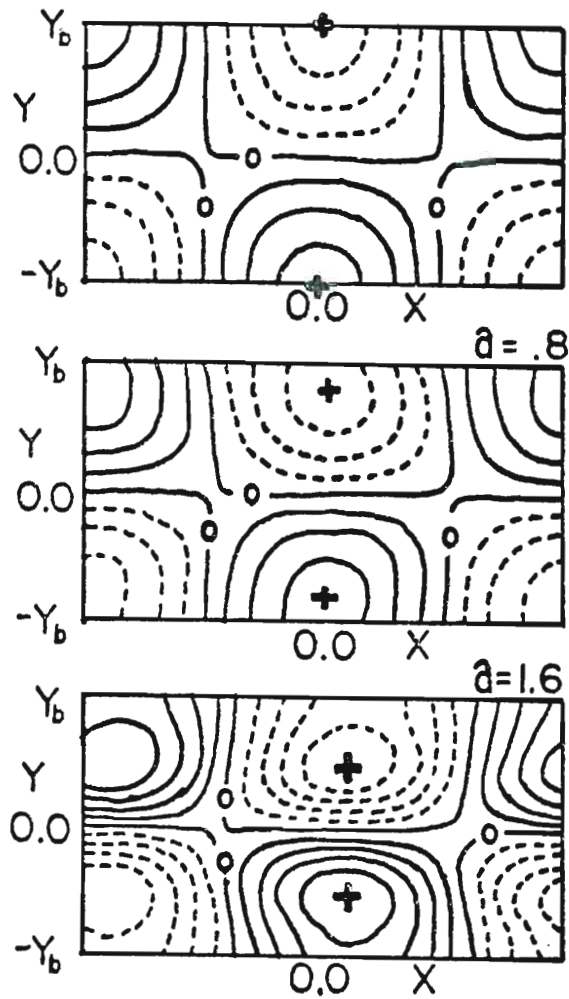


Fig. 18 Eddy zonal velocity fields at the surface for the lowest-order solution (top) and total Surface Front case solutions for $\underline{a} = .8$ (middle) and $\underline{a} = 1.6$ (bottom), where $\alpha = 2.0$ and $\pm Y_b$ are the meridional boundaries chosen for this value of α in geostrophic coordinates. The meridional scale of the prescribed front when $\underline{a} = .8$ is about twice that for $\underline{a} = 1.6$. The extrema of the eddy zonal velocity field (indicated by + symbols) provide a convenient measure of the meridional scale of the eddy. This figure shows that the meridional scale of the eddy solution is linked to the scale of the basic state front.

solution will be approximated by summing the first two terms in the perturbation series solution.) Unless otherwise stated, the exponential time amplification factor in (11a) equals one, by setting $T = 0$. To lowest-order there is no meridional scale to the basic state flow so the eddy zonal velocity maxima are at the boundaries. It is useful to define the frontal scale in terms of the latitudes where U_{YY} vanishes. The meridional positions where U_{YY} vanishes (see Fig. 11d for an example) are quite close to the latitudes of the eddy zonal velocity maxima shown in Fig. 18. This correspondence implies that the meridional scale of the wave is related to the meridional scale of the mean zonal current, a conclusion supported in an article by Simmons (1974), for example.

The moduli of the total pressure fields for the four cases are shown in Fig. 19. These solutions, where $\alpha = 2.0$, $\underline{a} = 1.6$ and $\beta = 1$, will be emphasized in the remainder of this chapter. The second-order contribution to the modulus can be deduced by comparing these plots with Fig. 8. In general, the magnitude of the pressure is increased in the vicinity of the strongest thermal gradients. One consequence is the reduction of the meridional scale mentioned earlier. Changes occur in the vertical structure as well. In the Upper Front case the amplitude is increased near the top of the domain and slightly reduced near the bottom. The opposite changes occur in the Surface Front case: the amplitude is increased near the surface and slightly diminished near the top.

case: the amplitude is increased near the surface and slightly diminished near the top.

The phase of the total pressure field is illustrated in Fig. 20 for the four cases. The phase angles in these cross sections are

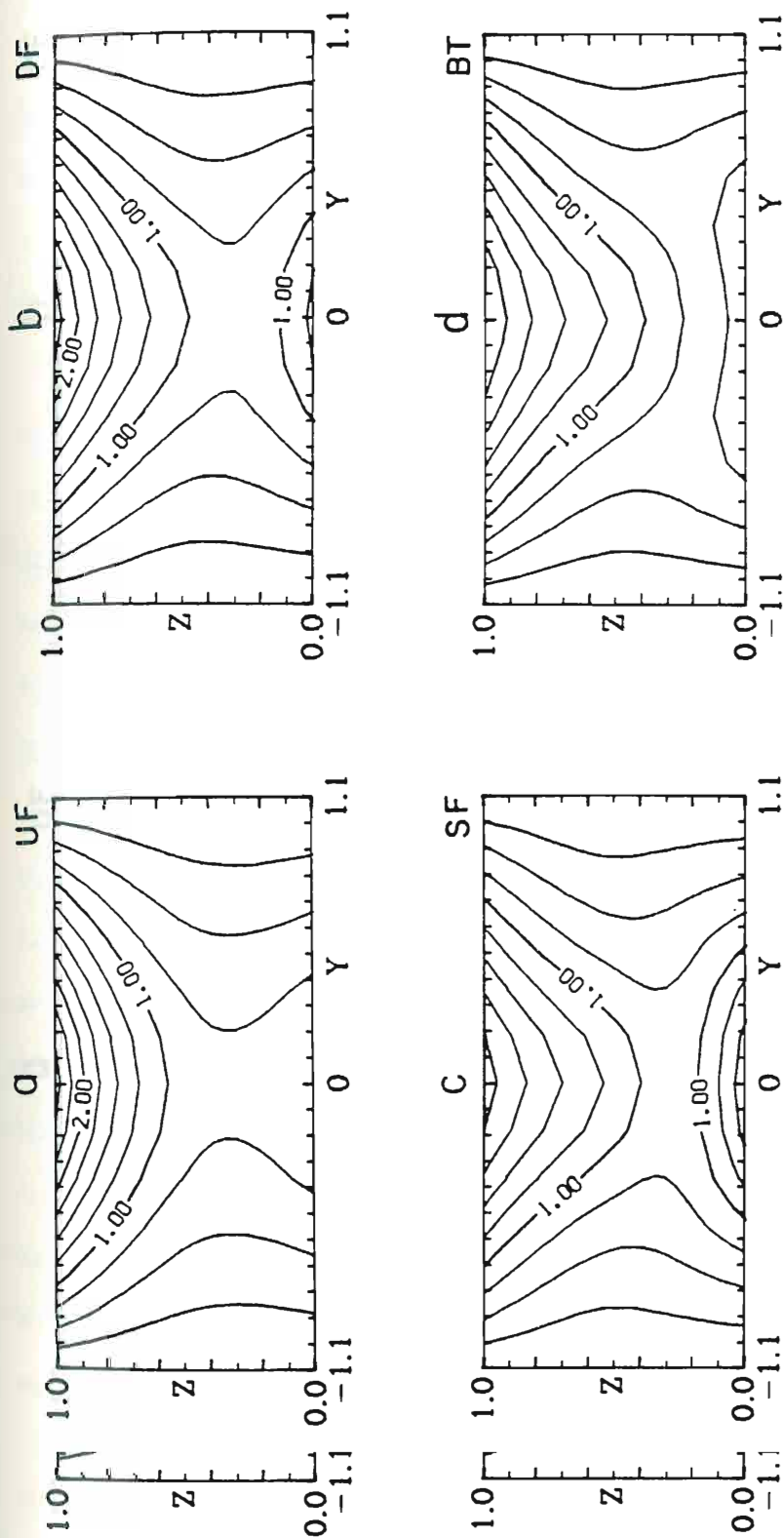


Fig. 19 Cross sections in geostrophic coordinates of the total pressure modulus for the four cases, where $\alpha = 2.0$, $\beta = 1.6$ and $\beta = 1$. The cases are a) Upper Front case, b) Deep Front case, c) Surface Front case and d) Barotropic case. The amplitude is generally increased in the vicinity of the thermal front (recall the lowest-order profile shown in Fig. 8).

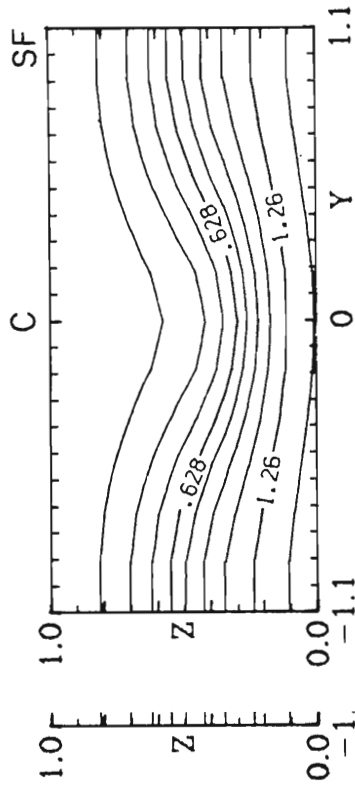
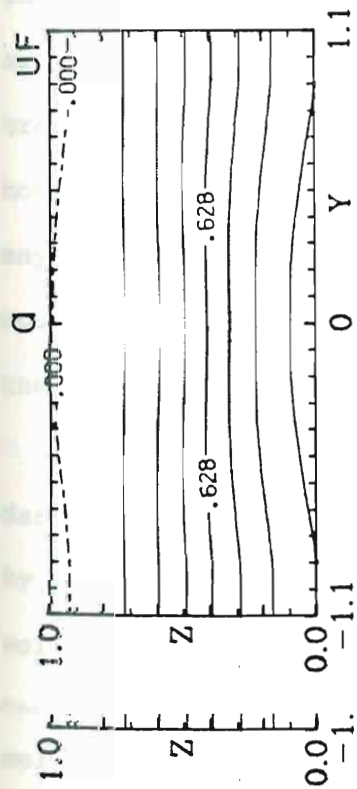
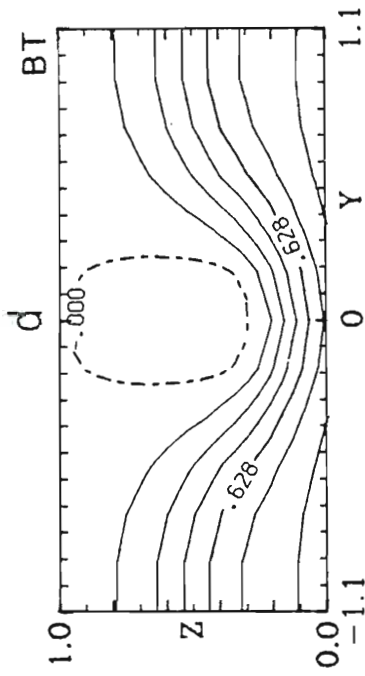
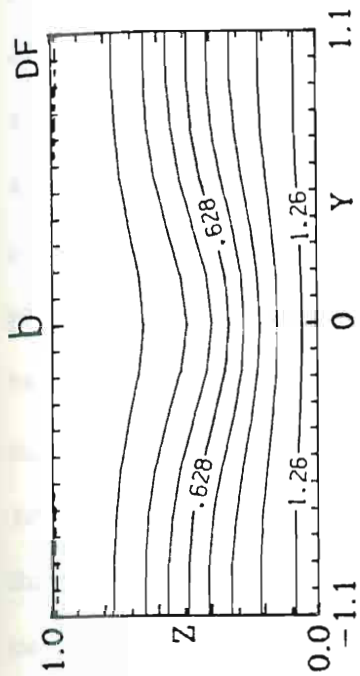


Fig. 20 Cross sections of the phase for the four cases shown in Fig. 19. Contours that dip down in the middle represent barotropically unstable horizontal tilts (southeast-northwest for $Y < 0$, southwest-northeast for $Y > 0$). These tilts arise from the horizontal shear associated with the prescribed thermal front. The westward tilt with height was generally increased at low levels and decreased at high levels by the second term in the perturbation series solution. See Fig. 26 for an alternate depiction of the tilts shown in Fig. 20c.

calculated relative to the phase at the center top. A positive value means that the feature is east of the corresponding feature at the center top. Generally, there is still westward tilt with height. But there are two major changes in the phase caused by the second-order solution. First, the westward tilt with height is increased slightly in the lower portion of the domain and greatly reduced in the upper portion. This latter effect becomes more prominent as the depth of the region of strong horizontal shear increases. In the Barotropic case for $\underline{a} = 1.6$ there is actually a slight eastward tilt near the top and center to second order. Second, horizontal tilts are introduced by the second-order solution. Contours that dip down at the center indicate that, at a given height, the trough and ridge axes tilt southeast-northwest for $Y < 0$ and southwest-northeast for $Y > 0$. These tilts are characteristic of barotropically unstable growth and are clearly visible in three of the cases. Also, these tilts are greatest near the middle and lower portions of the domain. The horizontal tilts are very weak in the Upper Front case and, if anything, indicate a slight barotropic damping near the vertical boundaries. The significance of these tilts is elucidated by examining the energy conversions.

An equation for the total perturbation energy can be easily derived (e.g., see Pedlosky, 1964a) from (7) and (5c). Multiply (7) by $\rho_s \phi$ and (5c) by $\epsilon \rho_s \phi_z$, where ϕ is the total perturbation pressure solution. Integrate both equations over the volume of the domain. Combine the resulting equations to obtain a solution. Integrate both equations over the volume of the domain. Combine the resulting equations to obtain:

$$\frac{\partial}{\partial T} \iiint \frac{\rho_s}{2} (\phi_x^2 + \phi_y^2) + \frac{\epsilon \rho_s}{2} \phi_z^2 dx dy dz = \quad (24)$$

$$- \iiint \rho_s U (\phi_x \phi_y)_y dx dy dz + \iiint \epsilon \rho_s U_z \phi_x \phi_z dx dy dz.$$

The left-hand side of (24) is the time rate of change of the total energy of the quasi-geostrophic eddy in geostrophic coordinates. The first term on the right-hand side is a barotropic generation term which converts zonal kinetic energy of the basic state into eddy kinetic energy. The integrand of this term is related to the eddy horizontal momentum convergence and is represented symbolically as $K_Z \rightarrow K_E$. The last term is a baroclinic generation term and converts available potential energy. This term is related to the eddy poleward heat flux and is represented symbolically as $A_Z \rightarrow A_E$. These two energy conversions will provide the nexus between the properties of the basic state and the stability and structure of the perturbation solution.

The zonally averaged barotropic energy conversion ($\overline{K_Z \rightarrow K_E}$) for each of the four cases is presented in Fig. 21. At first glance, the patterns of the energy conversion more or less agree with one's expectations from classical potential vorticity arguments. For an amplifying purely barotropic wave, the region of positive barotropic energy conversion occurs where $\beta - U_{yy}$ is positive, if the phase speed is between the minimum and maximum velocities of the zonal flow and if there are points in the domain where $\beta - U_{yy}$ vanishes. The regions of positive barotropic conversion in Fig. 21 correspond rather well with the regions where there are points in the domain where $\beta - U_{yy}$ vanishes. The regions of positive barotropic conversion in Fig. 21 correspond rather well with the regions of positive potential vorticity gradient in Fig. 11, even

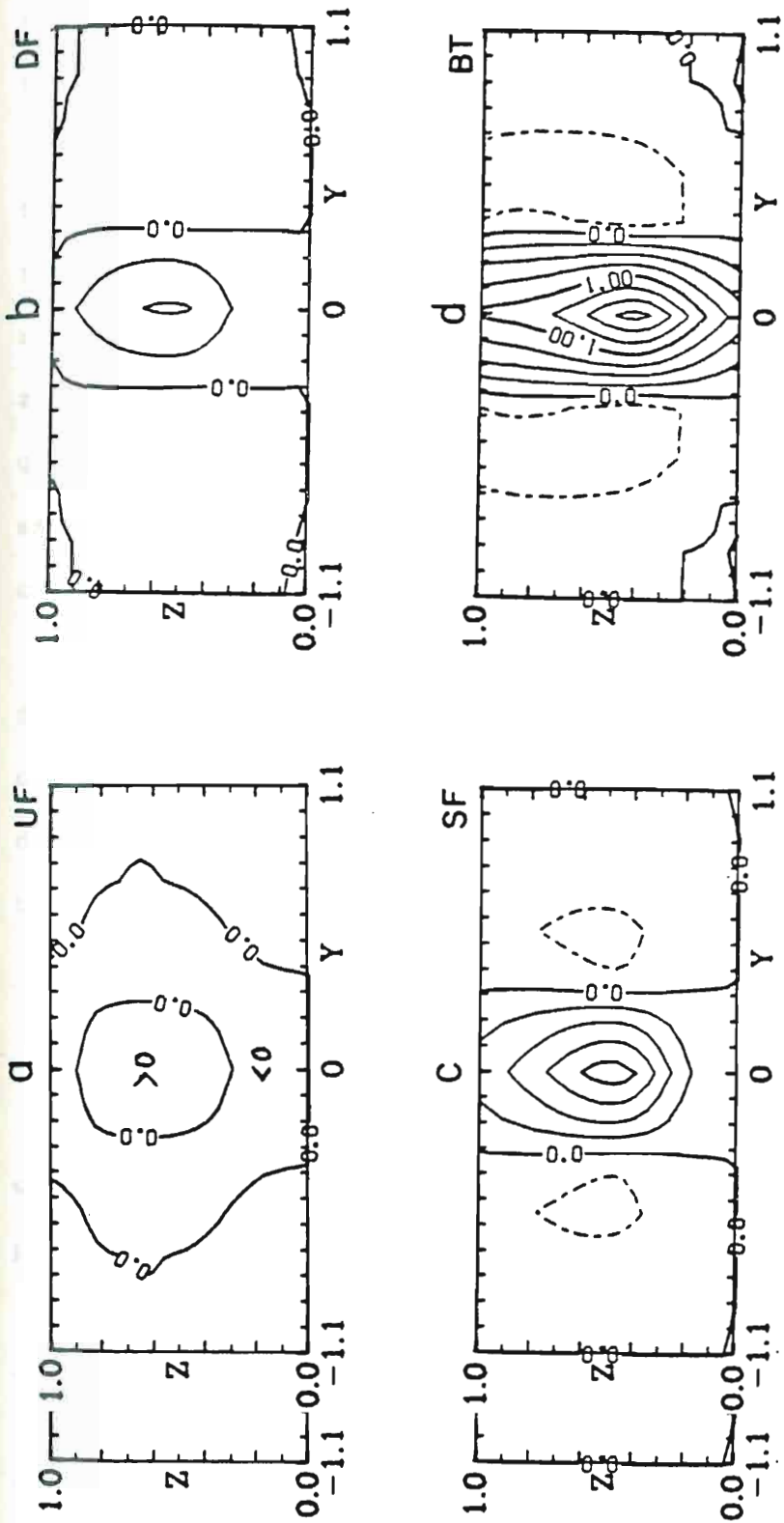


Fig. 21 Cross sections of the zonal average barotropic energy conversion ($\overline{K_Z + K_E}$) for the four cases shown in Fig. 19 in geostrophic coordinates. The areas of positive conversion correspond fairly well with the regions of positive q_y (compare with Fig. 11). The correspondence would be exact, according to the classical theory for a purely barotropic basic flow. It is not exact because the vertical shear in the basic flow, through the vertical boundary conditions, opposes the purely barotropic result. The magnitude of the positive conversion increases as the depth of the unstable horizontal shear increases. The maximum conversion occurs near the middle of the domain in all four cases partly due to the ρU_S term in (24). The contour interval is .25 in all four diagrams.

though q_y has vertical as well as meridional structure. This is a result that was anticipated by Kuo (1949, p. 118) many years ago, based upon the similarity of the model equations. The vertical position of the maximum is only slightly different in the four cases and is determined in part by the $\rho_s U$ factor. Not surprisingly, the barotropic conversion is weakest for the Upper Front case and strongest for the Barotropic. However, there is a discrepancy between these results and classical barotropic instability theory. The lines of zero conversion in Fig. 21 do not coincide with the zero contours of q_y in Fig. 11. In fact, the regions of positive conversion are smaller than the corresponding regions of positive q_y in three of the cases. The Upper Front case appears to be an exception to this rule.

This deviation from pure barotropic instability theory arises from the boundary conditions at the top and bottom and has been described mathematically by Held (1975). A similar relation can be derived for this model. The density-weighted vertical and zonal average total horizontal momentum convergence can be expressed as⁷

$$\int_0^1 M dz = \frac{kc_i}{2} \exp(2kc_i T) \left\{ \int_0^1 \frac{\mu \rho_s q_{1Y} |\hat{\phi}|^2}{|U - C|^2} dz + \frac{\rho_s \epsilon U_Z |\hat{\phi}|^2}{|U - C|^2} \Big|_{Z=0}^{Z=1} \right\} \quad (25)$$

where $M = -\rho_s \overline{\hat{\phi}_x \hat{\phi}_{yy}}$, C_i is the imaginary part of C and all the perturbation series have been summed. The lowest-order part of (25) is easily obtained. However, the individual higher-order parts are quite messy due to the perturbation expansion procedure and do not is easily obtained. However, the individual higher-order parts are quite messy due to the perturbation expansion procedure and do not

⁷A brief derivation of (25) is included in Appendix H.

further illuminate the effects shown succinctly in (25). The first term on the right-hand side is the well-known (e.g., Green, 1970) barotropic response. The last term shows the effect of having baroclinicity in the problem. At lowest-order this term sums to zero, but at higher orders it alters the momentum convergence and therefore the barotropic energy conversion. The sign of this term depends upon the relative magnitudes of its top and bottom boundary components and upon the sign of U_z . In the Surface Front case the value of the last term is decreased at the top and increased dramatically at the bottom by the second-order solution causing a net reduction in the momentum convergence. In the Upper Front case the opposite changes occur, though smaller in magnitude, and produce a slight increase in the momentum convergence. These changes explain the differences between these results and pure barotropic theory.

It is worth noting that the opposite barotropic conversion is obtained for the basic state profile discussed in detail by McIntyre (1970). That is, the region of positive q_y is associated with negative barotropic energy conversion. (See Appendix I.) The reason for this occurrence may be deduced from Brown (1969a). Brown (1969a, Figs. 2 and 3) found a demarcation between barotropically damped, short wavelength solutions and longer wavelength, barotropically amplified solutions for a basic current with vertical and horizontal shear. This result may be the analogue, for combined barotropic-baroclinic instability, of a result obtained by Kuo (1949). Kuo (1949) found that waves longer than the neutral wave were amplified while the shorter waves were damped, and that this condition was

related to the increase of the phase speed with wavenumber. The phase speed also increased with wavenumber in Brown's (1969a) solutions. In addition, he found that when the magnitude of the phase speed spectrum was increased, the wavelength of the demarcation also increased. McIntyre (1970) formulated his model on an f -plane so his phase speeds are about twice as large as they are on a β -plane. Apparently, the wave is short and fast enough, so that McIntyre's (1970) solution belongs to the barotropically damped class of waves found by Brown (1969a). The results detailed here, for the middle waves on a β -plane, ostensibly belong to the longer, barotropically amplified class of waves.

Since the last term in (25) arises from the baroclinic nature of the zonal flow and generally opposes the barotropic term, it follows that the presence of baroclinic vertical shear can inhibit the barotropic instability mechanism. This statement must be tempered somewhat since it is based upon the vertical boundary conditions. At the end of Chapter 2 a conceptual deficiency of the $W = 0$ boundary condition at $Z = 1$ was suggested. In (25) we can see some additional problems with relating this result to the atmosphere. For example, assume for the sake of argument that the form of the $Z = 1$ boundary term appropriately describes the effect of the tropopause. In this model it has been convenient to let U increase monotonically with height, whereas in the atmosphere the zonal flow typically reaches a maximum at the tropopause and may decrease with height above it. The U_z factor in the atmosphere the zonal flow typically reaches a maximum at the tropopause and may decrease with height above it. The U_z factor was large and positive at $Z = 1$ in this model but in the atmosphere the "appropriate" U_z might be small or even negative. Yet, the

damping effect arises from the quite reasonable boundary condition at $z = 0$. These arguments suggest that the inhibition of the barotropic conversion in the atmosphere might be even greater than what these calculations infer.

The effect of the barotropically unstable horizontal shear upon the baroclinic energy conversion is less ambiguous. The zonally averaged baroclinic conversion ($\overline{A_Z \rightarrow A_E}$) for each of the four cases is depicted in Fig. 22. For clarity, the lowest-order portion of this energy conversion, shown in Fig. 8, has been removed. In the three cases where a basic state front is present, we see how the poleward heat flux responds to the amplitude of the wave. In the Upper Front case the wave is of large amplitude primarily in the upper levels and that is where the heat flux is largest. In the Surface Front case, the wave amplitude is large near the bottom and so is the heat flux. The wave amplitude is large near the top, but the conversion is weak in the Upper Front case. Another feature of these plots is the occurrence of negative values at the upper levels in three of the cases. Indeed, the negative values dominate in the Barotropic case.

Both of these features tie together a number of the results presented above. The increase of the westward tilt with height near the bottom in the Deep and Surface Front cases increases the poleward heat flux there. The negative values of the baroclinic energy conversion near the top arise from the reduction of the westward tilt there. The growth rates are positive in the three frontal cases because the ~~conversion near the top arise from the reduction of the westward tilt there.~~ The growth rates are positive in the three frontal cases because the volume average of the baroclinic conversion is positive. The volume-averaged barotropic conversion is also positive, but it is smaller.

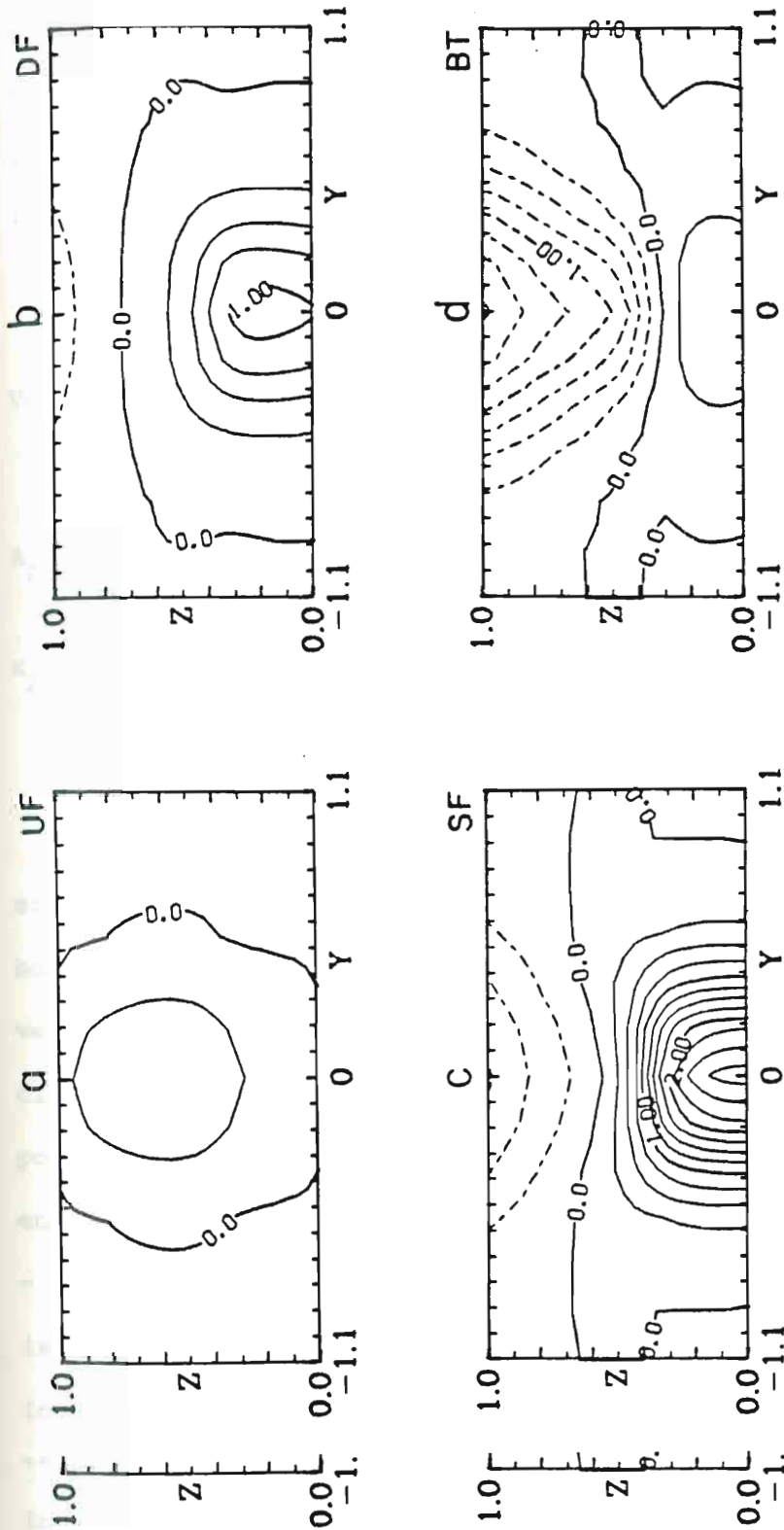


Fig. 22 Cross sections of the zonal average baroclinic energy conversion ($A_Z + A_E$) in geostrophic coordinates for the four cases shown in Fig. 19. The lowest-order conversion, shown in Fig. 8, has been removed to show the higher-order changes more clearly. In general, the poleward heat flux is largest in the vicinity of the basic state front; however it is difficult to obtain large values of this conversion at high levels due to the q_{ly} term in (26). Hence, the conversion is weak in the Upper Front case and strong in the Surface Front case. The negative values at high levels correlate with the reduced westward tilt noted in Fig. 20 and came from the presence of the horizontal shear. Thus, in the Barotropic case, where U_1 is independent of height, large negative values of the baroclinic conversion are produced because the barotropic instability mechanism is also operating. The contour interval is .25.

(The smaller magnitude is probably not caused by the vertical walls at $Y = \pm Y_D$ (see Kuo, 1949 and Brown, 1969b) at least for the middle waves.) The growth rates are negative in the Barotropic case because the baroclinic energy conversion was predominantly negative and exceeded the positive value of the barotropic conversion.

TABLE 1

Volume-Averaged Energy Conversions for the Four Cases ($a = 1.6, \alpha = 2.0$)

	Upper Front	Deep Front	Surface Front	Barotropic
$A_Z \rightarrow A_E$.070	.124	.241	-.202
$K_Z \rightarrow K_E$	-.001	.010	.030	.077

The source of these effects lies in the structure of the basic state. In the three cases where a front is added to the lowest-order basic state, the frontal temperature gradients introduce additional vertical shear. This additional vertical shear increases the baroclinicity of the zonal flow and is mainly responsible for the positive poleward heat fluxes visible in Fig. 22. The negative values of the energy conversion come from the horizontal shear and especially the $-U_{YY}$ term in q_Y . For the tanh profiles used in this study, this term is positive in the center of the domain, the same sign as the β term. Indeed, the q_Y term acts much like the nonzero β term did in the lowest-order solution. That is, it reduces the growth rate and phase speed of the wave. The westward phase tilt reduction and consequent

negative baroclinic energy conversion are greatest at the top because the effect of the q_Y term increases with height. This can be seen by deriving an equation for the heat flux h , similar in format to (25) and like that derived by Charney and Stern (1962).⁸

$$h(Z) = -\frac{kc_i}{2} \exp(2kc_i T) \int_0^Z \frac{\mu \rho_s q_{1Y} |\hat{\phi}|^2}{|U - c|^2} dz - \int_0^Z \rho_s \hat{\phi}_X \hat{\phi}_{YY} dz \quad (26)$$

where $h = \rho_s \overline{\hat{\phi}_X \hat{\phi}_Z}$. This relation shows that the damping effect caused by the positive values of q_Y accumulates with height. In the Barotropic case, large positive values of q_Y extend down to the surface, making this term quite large. There is no compensating additional vertical shear, as there was for the other cases, so the net effect is the predominately negative energy conversion and consequently negative second-order growth rates. Since the positive values of q_Y are associated with the horizontal shear in these cases, it follows that the barotropically unstable horizontal shear inhibits the baroclinic energy conversion mechanism.

The concept of a delta function in the potential vorticity at the vertical boundaries discussed by Bretherton (1966b) can be applied to (26). Using this line of reasoning we can understand how there was positive baroclinic conversion at lowest-order, even though both integrands on the right side of (25) vanish in the interior (except perhaps at a critical level). The same concept may explain the small positive values of the energy conversion near the surface in (perhaps at a critical level). The same concept may explain the small positive values of the energy conversion near the surface in

⁸

Note the sign error in the first equation on page 170 in that paper.

the Barotropic case. The special boundary values of q_y apparently create the shallow region of strong westward tilt with height in Fig. 20d. The resultant poleward heat flux in the lower third of the domain slightly exceeds the strong equatorward flux from the $-U_{1yy}$ term.

Some interesting aspects of the solutions are evident when the energy conversions are calculated in Cartesian coordinates. The transformation of coordinates is nonlinear because it involves the perturbation solution as well as the basic state. If the eddy is infinitesimally small, Fig. 12 and relations (7) can be used to deduce the linear changes produced by the transform. Crude calculations of the energy conversions for the Surface Front case are shown in Fig. 23, including the zonal average conversion from eddy available potential energy to eddy kinetic energy, $(\overline{A_E \rightarrow K_E})$. The lowest-order contribution is now included in these diagrams and the amplitude of the solution shown in Fig. 19c is used. The most obvious change in these plots is the poleward tilt with height introduced by the transform. This linear phenomenon was discussed earlier in this section in connection with Fig. 12. The $(\overline{A_E \rightarrow K_E})$ conversion, which is related to the vertical heat flux, has a maximum in the lower center of the domain. As expected, this maximum is somewhat higher in the Deep and Upper Front cases.⁹ The volume average of this conversion is between one quarter and one half the volume average of the

⁹ Energy conversion diagrams in Cartesian coordinates for the other cases are presented in Appendix I.

⁹ Energy conversion diagrams in Cartesian coordinates for the other cases are presented in Appendix I.

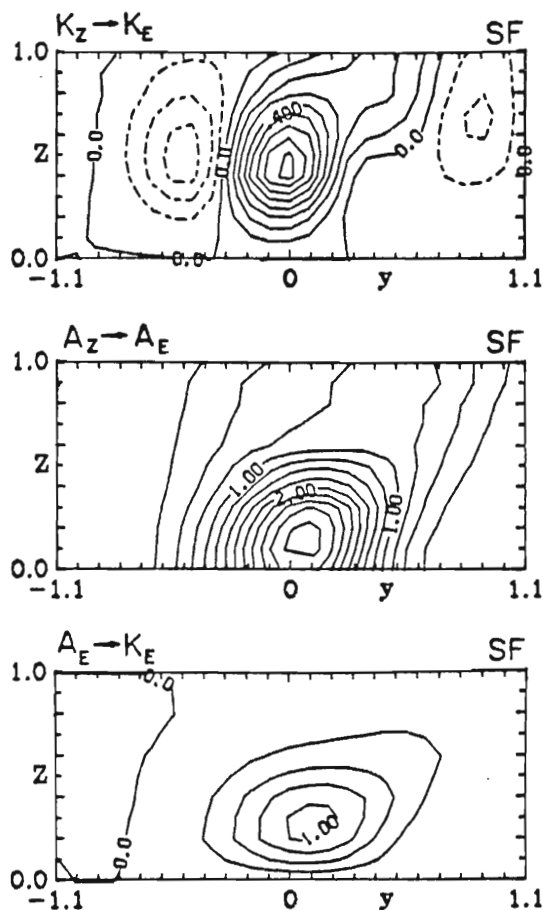


Fig. 23 Cross sections in Cartesian coordinates of the three zonal average energy conversions ($K_Z \rightarrow K_E$), ($A_Z \rightarrow A_E$) and ($A_E \rightarrow K_E$) for the Surface Front case where $\alpha = 2.0$, $\bar{a} = 1.6$ and $\beta = 1$. The transform was made using the finite eddy amplitude presented in Fig. 19c. The upper and middle diagrams may be compared with Figs. 20c and 21c, respectively. The coordinate transform introduces a poleward tilt with height as mentioned in connection with Fig. 12. The finite amplitude (nonlinear) transform causes little additional modification of the energy conversions. The nonlinear transform shifts the maximum barotropic conversion slightly south of the axis of mean zonal velocity maximum. The opposite shift occurs of the energy conversions. The nonlinear transform shifts the maximum barotropic conversion slightly south of the axis of mean zonal velocity maximum. The opposite shift occurs for infinitesimal eddy amplitude. The contour interval in the upper figure is .1 and .25 in the middle and lower diagrams.

$(A_Z \rightarrow K_E)$ conversion. Thus, both components of the eddy total energy are built up by the baroclinic instability mechanism.

The magnitude of the barotropic conversion $(\overline{K_Z \rightarrow K_E})$ is also about the same as its value in geostrophic coordinates. The coordinate transform does not alter the growth rate, so since it did not significantly change the baroclinic conversion, one would not expect the volume-averaged barotropic conversion to be appreciably altered either. The maximum is shifted to the equatorial side of the mean zonal velocity maximum. This change may be due, in part, to the crude manner in which the figure was calculated. The large positive conversion is produced in the areas just west of the high and low centers of the eddy pressure field. As mentioned previously, the coordinate transform is one of two sources of ageostrophy in this model; the other is the subject of the next chapter.

6. SECOND-ORDER AGEOSTROPHIC SOLUTION

In the previous chapter the quasi-geostrophic portion of the second-order solution was discussed. In addition, the ageostrophic and nonlinear modifications of this solution by the coordinate transform were briefly described. In this chapter, the higher-order terms in the interior equation (8) and the vertical boundary conditions are examined. Since these terms are neglected in the quasi-geostrophic equations, their contribution is labelled an "ageostrophic" effect. Recall that the perturbation solution has Y variation, which Phillips (1964) suggests is necessary to examine properly the non-geostrophic effect. The many terms from (8), that do not vanish at second order, are classified into five groups according to origin. These groups can be examined separately as well as together because the model equations are linear in geostrophic coordinates. These terms can only respond to the leading-order, purely baroclinic, basic state variables. It will be shown that the source of ageostrophy in geostrophic coordinates is primarily the divergence term in the vorticity equation and that it is strongly asymmetric in Y .

The ageostrophic term in the model equations include the terms on the right-hand side of (8) and higher-order terms in the vertical boundary conditions. Many of these terms in (8) vanish at second order, leaving
order, leaving

$$\mathcal{L}(\hat{\phi}_1) = DV + GC + VC + BV \quad (27)$$

where

$$\begin{aligned} DV = & -\varepsilon(2f_{1Z}\hat{\phi}_{OZ} + f_1\hat{\phi}_{OZZ}) - \varepsilon a_3 c_o s \hat{\phi}_{OZ} + \varepsilon s \hat{\phi}_o (f_1 U_{OZZ} + 2f_{1Z} U_{OZ}) \\ & + \varepsilon^2 (\psi_{OZZ}\hat{\phi}_{OZZ} + \psi_{OZZZ}\hat{\phi}_{OZ} + s \hat{\phi}_o (\psi_{OZZ} U_{OZZ} + \psi_{OZZZ} U_{OZ})) \\ & - \beta Y \varepsilon (\hat{\phi}_{OZZ} + a_6 \hat{\phi}_{OZ}) + \beta^2 Y S \hat{\phi}_o - a_4 c_o s (a_5 Y \hat{\phi}_o - \hat{\phi}_{OZ}) \\ & + a_6 \varepsilon ((a_3 - f_{1Z}) \hat{\phi}_o - f_1 \hat{\phi}_{OZ} + \varepsilon \psi_{OZZ} \hat{\phi}_{OZ}) - g_1 \varepsilon \hat{\phi}_{OZ} \\ & - a_6 \varepsilon s \hat{\phi}_o ((a_3 - f_{1Z}) U_o - f_1 U_{OZ} + \varepsilon U_{OZ} \psi_{OZZ}) + g_1 \varepsilon U_{OZ} s \hat{\phi}_o, \end{aligned}$$

$$GC = -\beta S U_o \hat{\phi}_{oY} + \varepsilon \alpha^2 (f_1 - \beta Y) \hat{\phi}_o,$$

$$VC = -\beta S U_o \hat{\phi}_{oY},$$

$$BV = \beta \hat{\phi}_{oY},$$

$$s = (U_o - c_o)^{-1} \quad \text{and} \quad a_7 = a_6 + \mu g_1(z) + O(\mu^2).$$

The term DV comes from the divergence term in the vorticity equation. This term can be subdivided. The terms in DV containing the factors a_4 , a_6 or g_1 occur because the model fluid is compressible, that is, if incompressibility had been assumed, these terms would not appear in DV. So, these terms can be referred to as compressible divergence terms (CDV) and the remaining terms in DV as incompressible divergence terms (IDV). The geostrophic correction term, GC, results divergence terms (CDV) and the remaining terms in DV as incompressible divergence terms (IDV). The geostrophic correction term, GC, results from using the pressure as a streamfunction to lowest-order. These

terms appear because ρ_s and H are functions of Z and $\beta \neq 0$. The VC term comes from the $O(\mu)$ part of η_3 in geostrophic coordinates. The BV term arises from the transformation of the βv term in the vorticity equation and makes a much smaller contribution than the other terms. The vertical boundary conditions are heterogeneous.

$$\begin{aligned} \mathbb{D}(\hat{\phi}_1) = \text{BT} \equiv & C_0 \beta Y S \hat{\phi}_{0Z} - f_1 S \hat{\phi}_{0Z} \\ & + \hat{\phi}_0 \left[(a_3 - f_{1Z}) + S(U_{0Z} f_1 - U_0 (a_3 - f_{1Z})) \right] \quad \text{at } Z = 0, 1. \end{aligned} \quad (28)$$

The terms in BT mainly come from the compressibility of the static state through the $O(\mu)$ part of (5a).

Growth rate and phase speed spectra for each of the second-order ageostrophic terms are presented in Fig. 24 for both $\beta = 0$ and $\beta = 1$. For the middle waves, the total effect of the ageostrophic terms is to reduce both the growth rate and phase speed and it varies only slightly with wavenumber. The individual components have greater variation with α . The terms VC and BV are odd functions of Y , so from (13) they do not contribute to C_1 . The two components of DV generally oppose each other, but the complete DV term reduces the growth rate and phase speed, as does the BT term. The GC term also reduces the phase speed. For the shorter of the middle waves, the GC term increases the growth rate. For the longer of the middle waves, the growth rate is slightly decreased for $\beta = 1$ and nearly unchanged for $\beta = 0$ by the GC term.

These results may be compared with the conclusions from a study for $\beta = 0$ by the GC term.

These results may be compared with the conclusions from a study by Derome and Dolph (1970). They examined some higher-order in μ modifications of one of Eady's (1949) solutions. However, they

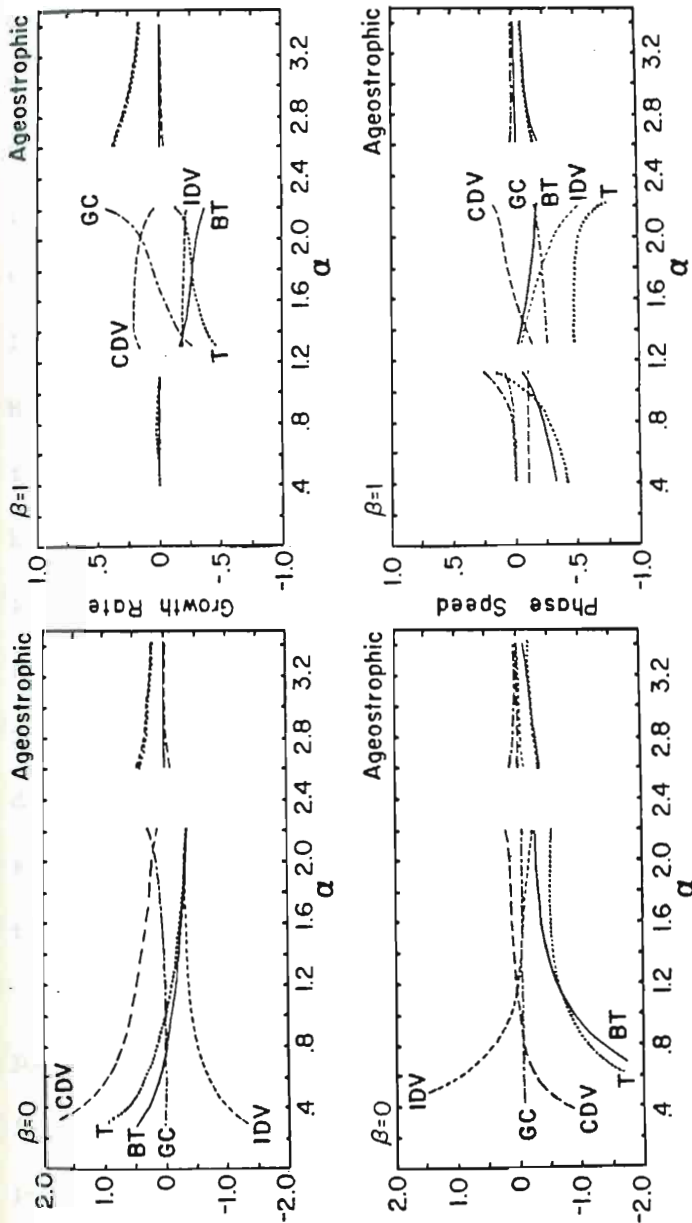


Fig. 24 Second-order growth rate and phase speed spectra for the ageostrophic terms in (27) and (28) for $\beta = 0$ and $\beta = 1$. The upper pair of diagrams show the growth rate spectra; the lower pair show the phase speed spectra. Note that the range of the vertical axes in the figures where $\beta = 0$ is twice that for $\beta = 1$. The terms represented by the different types of lines are: CDV by the long dashed lines, IDV by the shorter dashed lines, GC by the dot-dashed lines, BT by the solid lines and their total by the dotted lines. The VC and BV terms are odd functions of α so they do not contribute to the complex phase speed. For the middle waves, the ageostrophic terms reduce the phase speed and growth rate. The compressible (CDV) and incompressible (IDV) parts of the divergence term (DV) generally oppose each other.

retained the assumptions of incompressibility and constant Coriolis parameter. They also chose a different mathematical formulation than that used in this study which, as they discuss, apparently creates an inconsistency between the boundary conditions. They found that to second order in μ the growth rate was decreased and the phase speed unchanged for the unstable waves in Eady's analysis. They also found that a poleward tilt with height was introduced into the solutions. This latter feature manifests itself in this model by the linear part of the coordinate transform (see Fig. 12) and was noted by Hoskins (1975). A crude comparison between their results and those from this study can be made by ignoring the GC, CDV and possibly the BT terms in the $\beta = 0$ complex phase speed. The BT term contribution is uncertain, since it arises largely from allowing compressibility in the problem, but not entirely. Keeping this in mind, the results for this model seem to agree with some of their calculations. The disagreement occurs for the propagation speed of the eddy. This study suggests that including compressibility in the problem may lead to a reduction of the phase speed by non-geostrophic effects.

The amplitude and phase of the sum of the ageostrophic terms are presented in Fig. 25 where $\beta = 1$ and $\alpha = 2.0$. The quantities depicted in Fig. 25 are not linear so the contributions by the individual components cannot be as easily separated as they could for the complex phase speed. The maximum amplitude is not appreciably changed by the ageostrophic terms, but meridional asymmetry is introduced. The magnitude poleward of the center is enhanced while that equatorward of the center is diminished. This change in amplitude also reduces the

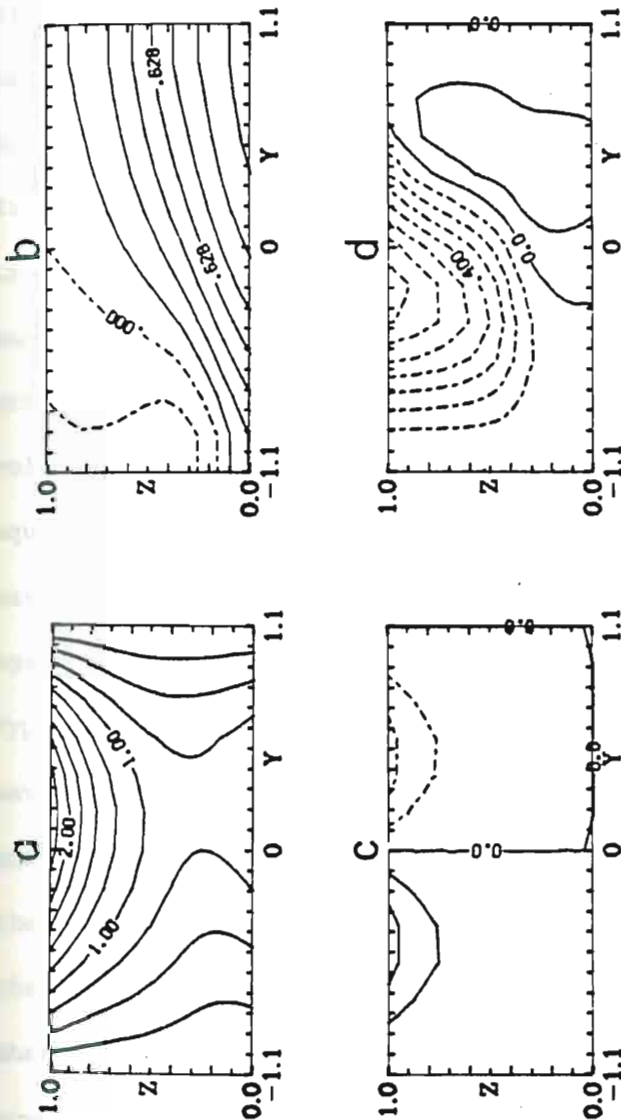


Fig. 25 Structure of the total ageostrophic solution for the lowest-order basic state, where $\alpha = 2.0$ and $\beta = 1$. Cross sections are presented of the: a) pressure modulus, b) pressure phase, c) barotropic energy conversion ($K_z + K_e$) and d) baroclinic energy conversion ($A_z + A_e$). The lowest-order contribution to the baroclinic conversion (see Fig. 8) has been removed in d, for clarity. The ageostrophic terms introduce meridional asymmetry into the solution. The amplitude is enhanced to the north of the center and diminished to the south. A strong southwest-northeast horizontal tilt is now present across the domain. Though the volume average of the barotropic conversion is zero, the zonal average is not. The ageostrophic terms transport zonal momentum to the north, tending to form a jet near $Y = .5$. These terms create a strong equatorward heat flux at high levels and a much weaker poleward flux near the surface. The volume-averaged baroclinic conversion is negative, thus explaining the reduction of the growth rate by the ageostrophic terms. The contour intervals in these plots are: .25 in a and c, .05 π in b and .1 in d.

meridional scale of the eddy. The latitudes of the eddy zonal velocity maxima are at $Y = Y_b$ and near $Y = -Y_b/2$. Since the latitude of the former is at the boundary and cannot shift poleward, it is not clear whether the scale reduction is actually due to the ageostrophic terms or is an artificial consequence of the boundary conditions. The term largely responsible for this change in the amplitude is the divergence (DV) term. The GC and BT terms are of secondary importance.¹⁰ The ϕ_1 's calculated from the VC and BV terms are much smaller. There are two major changes in the phase caused by the ageostrophic terms. At mid-levels the westward tilt with height of the solution is increased poleward of about $Y = .2$ and is decreased on the equatorward side. These changes introduce a strong southwest to northeast meridional tilt of the trough and ridge axes across the domain. Again, the DV term is largely responsible for these changes. This type of tilt is observed at lower and middle latitudes for cyclone waves in the atmosphere (e.g., Palmén and Newton, 1969). Saltzman and Tang (1972) were unable to reproduce these horizontal tilts in their 2-layer model, which included some non-geostrophic terms, unless they introduced horizontal shear into the basic flow. Their claim, that horizontal shear in the basic current is required to produce

¹⁰ Derome and Dolph (1970) describe the structure of their solution by displaying cross sections of the real and imaginary parts of the v and w fields. Assuming that $v = \phi_x$, we find that the general features in the imaginary part of ϕ_1 here, agree with those in the negative of their real part of v . However, the real part of ϕ_1 is similar in the lower region but of opposite sign above. See Appendix I for plots of the real and imaginary parts of the DV, GC, BT and total ageostrophic ϕ_1 's.

these tilts, seems to conflict with the results found by Derome and Dolph (1970), Hollingsworth (1975) and this study.

The barotropic ($\overline{K_Z \rightarrow K_E}$) and baroclinic ($\overline{A_Z \rightarrow A_E}$) energy conversions due to the ageostrophic terms are also shown in Fig. 25 where $\beta = 1$ and $\alpha = 2.0$. The lowest-order contribution has been removed from these plots and the lowest-order basic state wind U_0 was used in the calculation of these conversions. There is no horizontal shear in the basic state wind field used in the computation of the second-order ageostrophic solution. Therefore, the volume average of the barotropic energy conversion should be zero. But unlike the lowest-order solution, the zonal average of this conversion for the ageostrophic terms does not vanish at second order. Instead, there is a tendency to build up the mean zonal velocity poleward of the center and decrease it on the equatorward side, especially at high levels, though the volume average of the conversion is still zero. Therefore, the ageostrophic terms are forming a jet in the meridionally uniform basic state flow. Hollingsworth (1975) also found northward momentum transport produced by some non-geostrophic terms in a 2-layer model for a purely baroclinic zonal flow. The jet which would be formed lies poleward of the center, as does the axis of the eddy pressure maximum. The baroclinic conversion is also asymmetric. From Fig. 25d it is clear that the volume average of this conversion is negative, thereby explaining the decrease in the growth rate by the ageostrophic terms. The negative values are due to a strong equatorward energy flux, thereby explaining the decrease in the growth rate by the ageostrophic terms. The negative values are due to a strong equatorward heat flux in the upper half of the domain which is manifested by the eastward tilts of the trough and ridge equatorward of the center.

In the previous section it was shown that the strong horizontal shear of the jet stream can lead to an up-gradient, equatorward heat flux at high altitudes for a quasi-geostrophic eddy. From Fig. 25 it is clear that the non-geostrophic terms also can produce an up-gradient heat flux, primarily on the equatorial side of the wave. The low-level poleward heat flux cannot compensate the upper level equatorward flux in part because the value of $U_{\sigma z}$ is much smaller near the bottom than near the top (see (24)). As before, the DV term is primarily responsible for these effects.

In conclusion, the ageostrophic terms introduce a considerable amount of meridional asymmetry into the solution. While they don't affect the maximum amplitude of the solution appreciably, they do cause marked changes in the phase of the eddy that alter the energy conversions and result in reductions of the growth rate and phase speed. Finally, the ageostrophic terms introduce horizontal shear into the meridionally uniform mean zonal velocity field.

7. SYNOPTIC ASPECTS OF THE PRIMARY VARIABLES

In the previous sections the perturbation solutions have been discussed in nondimensional and therefore rather abstract terms. In this chapter the three-dimensional structures of the primary variables are briefly described in dimensional terms. The primary variables considered are pressure, temperature and velocity. The dimensionality is restored by using (3) and (2a), so for the pressure and temperature, the dimensional vertical variation can be largely determined by the static state.

The three-dimensional structure of the eddy pressure in Cartesian coordinates is illustrated in Fig. 26 for the quasi-geostrophic Surface Front case where $\beta = 1$ and $\alpha = 2.0$. The zonal average pressure has been removed and the three levels are the surface, 4 km and 8 km. As before, $T = 0$ so the exponential time amplitude factor in (11a) equals one. This figure exemplifies the features described earlier in connection with Figs. 19 and 20. The westward tilt with height of the trough and ridge axes is evident in this figure. The poleward tilt with height introduced by the coordinate transform is also evident. The barotropically unstable horizontal tilts are most prominent only at the middle level and almost nonexistent at the surface. Even though the nondimensional pressure modulus was largest at the top, the exponential decrease of ρ_s with height causes the dimensional eddy pressure to be largest at the bottom. However, the geopotential height of a

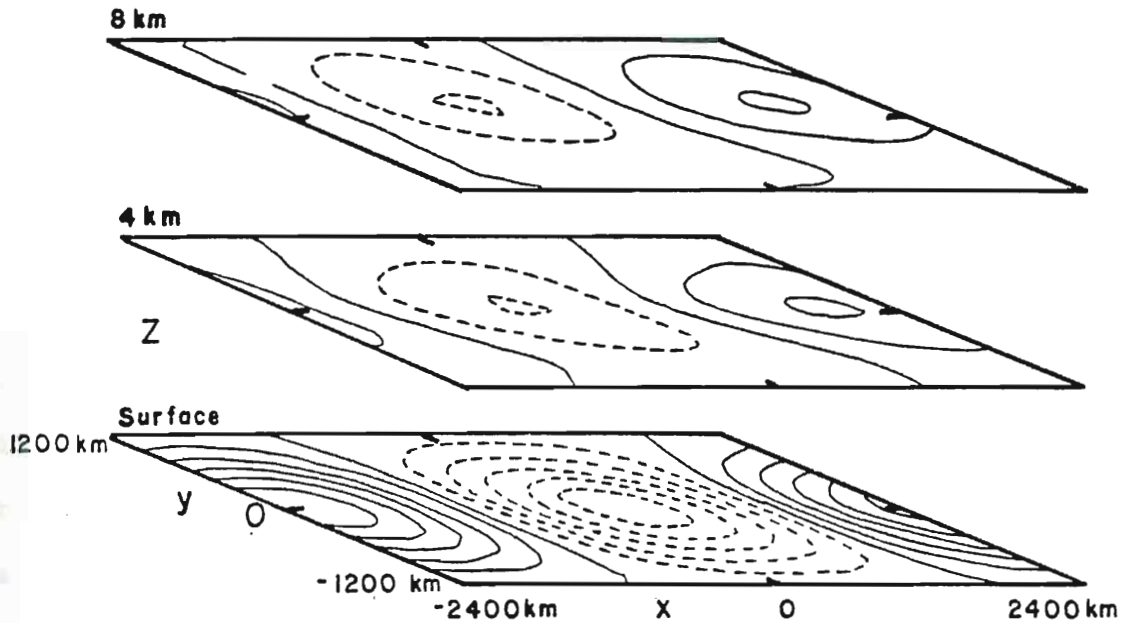


Fig. 26 The dimensional eddy pressure field at three levels for the quasi-geostrophic Surface Front case solution with $\alpha = 2.0$, $\underline{a} = 1.6$ and $\beta = 1$. The westward and poleward tilt with height of the trough and ridge axes can be seen in this figure. The barotropically unstable horizontal tilts are clearly visible only in the middle plot. The vertical length scale is 10 km. The contour interval is 2 mb.

pressure surface is more commonly used in meteorology. From the viewpoint of geopotential height deviations, the amplitude is largest at the top.

The relation between the total potential temperature and pressure fields at the surface is illustrated in Fig. 27. In addition, two meridional cross sections relating the potential temperature and zonal velocity fields are also presented. The solution depicted in Fig. 27 is the Surface Front case along with the ageostrophic terms; therefore it includes all second-order effects. The major visible difference between this solution and the quasi-geostrophic Surface Front case solution is a slight shift of the contours to the north. For example, the surface high and low pressure centers in the quasi-geostrophic solution lie along $Y = 0$. The coordinate transform causes the high pressure center to expand in horizontal area and the low center to contract. This change was noted by Hoskins (1975); it is a recognized ageostrophic effect (e.g., Saltzman and Tang, 1972) that is observed in the atmosphere. The upper plot shows the surface warm and cold fronts developed by the growing wave. Both fronts intensify as the eddy evolves. The maximum cross-frontal temperature gradient for the stage of development shown in Fig. 27 is twice the maximum gradient of the surface thermal front in the prescribed flow. The middle diagram is a cross section taken at about $x = -1600$ km and cuts across the cold front. The bottom diagram is chosen to intersect the warm front and is taken at about $x = 100$ km. These cross sections across the cold front. The bottom diagram is chosen to intersect the warm front and is taken at about $x = 100$ km. These cross sections indicate that the thermal fronts are quite shallow, as is typically observed during the early stages of mid-latitude wave-cyclone

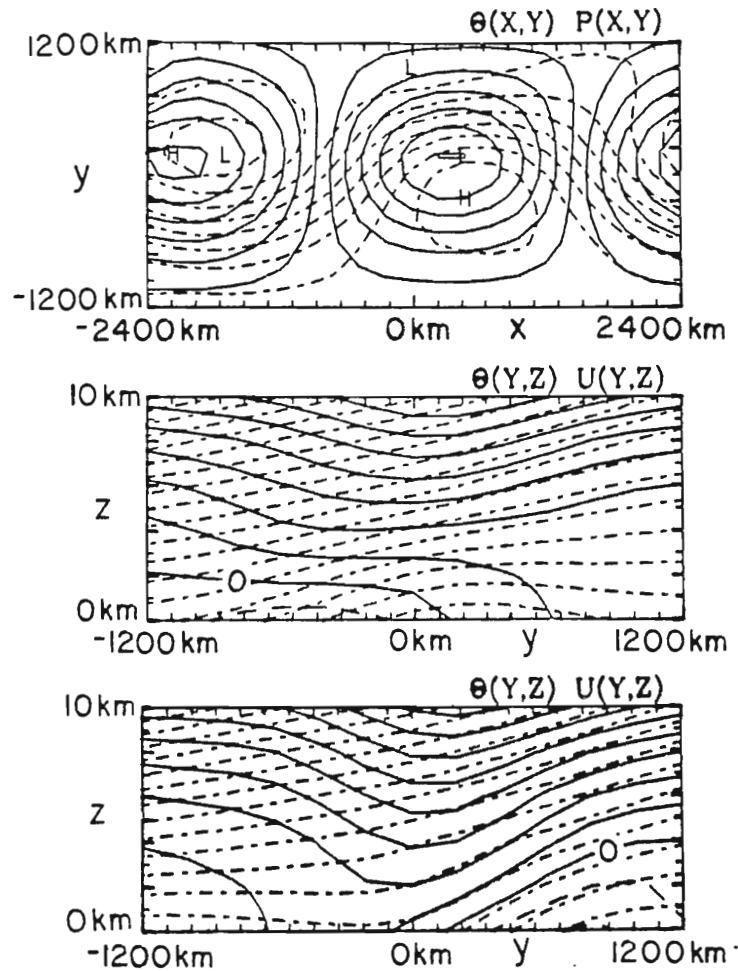


Fig. 27 The top contour plot relates the dimensional fields of pressure (solid lines) and potential temperature (dot-dashed lines) at the surface. The middle and bottom plots are cross sections, taken near $x = -1600$ km and $x = 100$ km, of the dimensional potential temperature (dot-dashed lines) and zonal velocity (solid and long dashed lines indicate westerly and easterly flow, respectively). This solution is for the Surface Front case including all ageostrophic effects, where $\alpha = 2.0$, $\underline{a} = 1.6$ and $\beta = 1$. The coordinate transform causes the high pressure region to be larger than the region of low pressure. The ageostrophic terms cause the surface high and low pressure centers to be north of $y = 0$. The temperature gradient across the front is twice that of the prescribed front. However, the thermal front the region of low pressure. The ageostrophic terms cause the surface high and low pressure centers to be north of $y = 0$. The temperature gradient across the front is twice that of the prescribed front. However, the thermal front remains shallow. The contour intervals are: 2° K and 2 mb in the top plot, and 4° K and 5 m/s in the lower two diagrams.

formation. However, in the atmosphere the cold front which develops to the west of the surface high often eventually extends through the depth of the troposphere. The extension of the front through the depth appears to be weak in this model, but the ageostrophic terms do tend to encourage this development. This is not surprising since ageostrophic effects are quite important for the generation of strong fronts and this model is primarily quasi-geostrophic with ageostrophic changes presumed to be of secondary importance. Yet the poleward tilt with height of the zonal velocity maximum that was discussed earlier is also visible in these cross sections.

Two types of parcel trajectories are presented in Fig. 28 for the quasi-geostrophic Surface Front case. The "Eulerian" trajectories are determined relative to the fixed coordinates, whereas the "Lagrangian" trajectories are displayed relative to the moving wave. In other words, the Eulerian trajectories show the parcel paths seen by an observer standing on the surface, while the Lagrangian trajectories are seen by an observer moving with the wave. Hence, the surface high and low pressure centers (marked by H and L, respectively) move as indicated in the upper chart but are stationary in the lower diagram. These trajectories were computed while the storm was amplifying and show the movement over a period of one day. During this time, the exponential time factor in (11a) increases from .75 to about 1.2. The dashed arrows are the projection of the three-dimensional paths (given by the solid lines) upon the surface and are intended to aid in the interpretation of the trajectories. The lower plot can be favorably compared with an idealized trajectory diagram in Palmén and

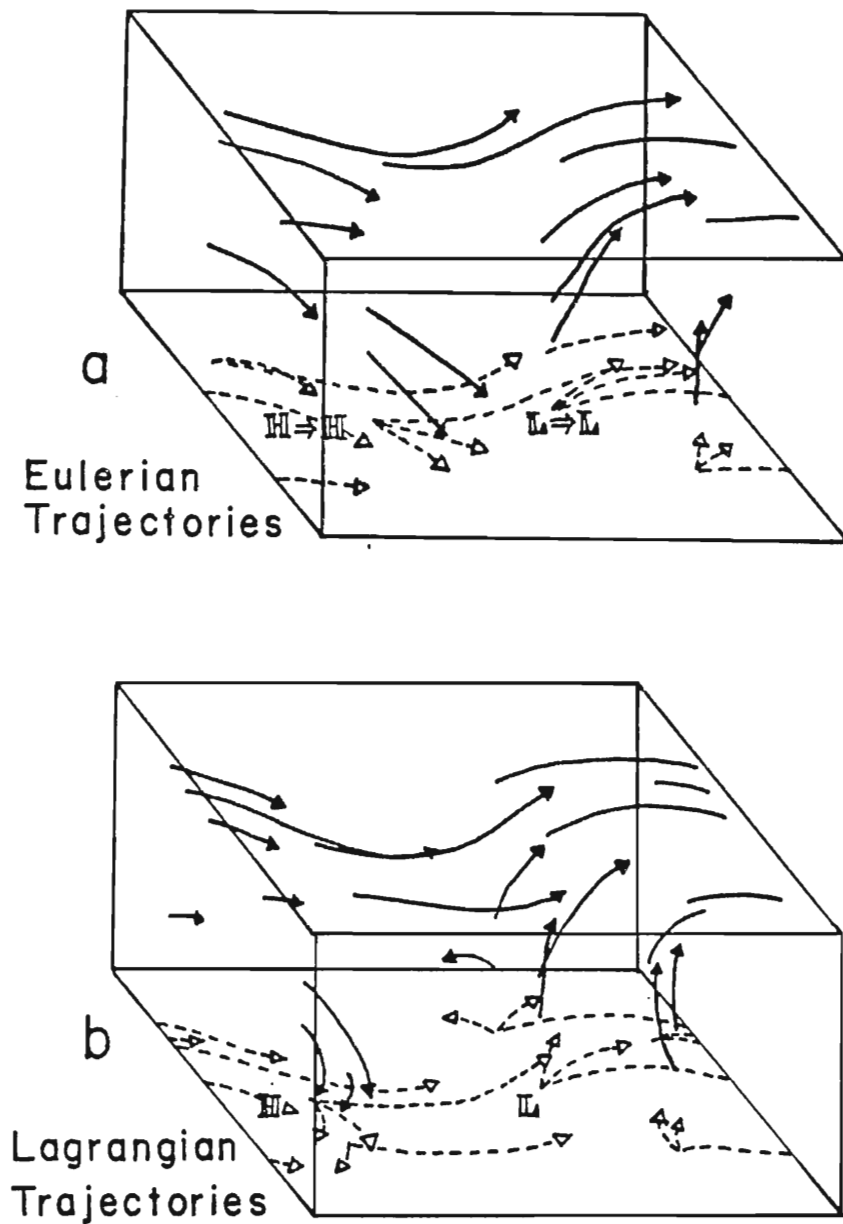


Fig. 28 Two depictions of the trajectories associated with the amplifying quasi-geostrophic Surface Front case solution for $\alpha = 2.0$, $\underline{a} = 1.6$ and $\beta = 1$. The arrows show the paths travelled by the parcels during one day. The "Eulerian" trajectories are determined relative to the Cartesian coordinates; the "Lagrangian" trajectories are calculated relative to the phase speed of the wave. The solid arrows are the three-dimensional trajectories; to aid interpretation of them, their projection onto the lower surface is indicated by the dashed arrows. See the text for further discussion.

Newton (1969, Fig. 10.20). Briefly, the upper-level flow is dominated by the strong zonal flow. There is rising motion east of the surface low and sinking motion west of it. The vertical velocities are largest near the fronts. The horizontal wind generally veers with height in the regions of warm air advection and backs with height in the regions of cold air advection (east of the surface low and high centers, respectively). All these features are observed in the atmosphere.

8. SUMMARY

This study has sought to elucidate the effects of a thermal front upon the stability, structure and energetics of an incipient wave-cyclone. The major findings are: 1) the maximum growth rate shifts to shorter waves when the prescribed thermal front decreases in meridional scale and increases in intensity, 2) the wave amplitude is increased in the vicinity of the front, 3) the meridional scale of the eddy is smaller when the scale of the prescribed front is smaller, 4) the barotropic and baroclinic instability mechanisms inhibit each other, 5) the ageostrophic terms reduce the growth rate and phase speed of the wave and 6) the ageostrophic terms tend to form a jet by transporting momentum poleward. The results of this study agree with several observed properties of the atmosphere.

An analytic model was used to isolate and examine these effects. The solutions of this model consist of perturbation series, where the Rossby number is the small expansion parameter. The Surface Front case (where the prescribed thermal front is confined near the bottom) for $\alpha = 2.0$ and $\beta = 1$ has been a paradigm of the solutions obtained from this model. The lowest-order quasi-geostrophic modifications were examined separately in the previous chapter. The solutions exhibit many well-known properties but also contain somewhat unexpected features. In this final chapter, these results will be summarized exhibit many well-known properties but also contain somewhat unexpected features. In this final chapter, these results will be summarized and further interpreted.

The analytic model employed in this study combines and extends the approaches in several previous studies by others. This model is adiabatic, frictionless, fully compressible and the Coriolis parameter varies linearly. A perturbation method outlined by McIntyre (1970) is used to formulate and solve this model. A nonlinear coordinate transformation (after Hoskins, 1976) is made which incorporates some ageostrophic effects. In the transform space the model is linear. In addition, some ageostrophic terms, neglected in the quasi-geostrophic equations, are retained after scaling the primitive equations. Even so, there are still many approximations in this model. Those assumptions which influence the interpretation of the model solutions are analyzed at the end of Chapter 2. The results discussed by Green (1960) are germane to the lowest-order solutions presented here. The higher-order terms in the perturbation series solutions respond to the basic state thermal front and to the ageostrophic terms. Three cases were examined which were distinguished by the vertical structure of the thermal front. A fourth case was also examined where the second-order basic state current was independent of height (so no front was present). All four cases had the same meridional variation.

Growth rate and phase speed spectra were determined for the four quasi-geostrophic cases and for the ageostrophic terms. Both long- and short-wave cut-offs were present in the lowest-order solution; the former is related to the nonzero β , both are related to the vanishing interior potential vorticity gradient. There was little difference the former is related to the nonzero β , both are related to the vanishing interior potential vorticity gradient. There was little difference between the growth rate spectra for the three frontal cases, even though the boundary and interior contributions to the growth rate

varied considerably between the three cases. Nearly all waves in the second-order quasi-geostrophic solutions were unstable, ostensibly due to the presence of a nonzero potential vorticity gradient at a critical level (see Bretherton, 1966a,b). In the cases where a thermal front was prescribed, as the intensity of that front was increased so was the growth rate, up to some asymptotic value. The wavelength of maximum instability shifted to shorter waves as the meridional scale of the front decreased, which seems to be consistent with Brown (1969a) and Simmons (1974). In contrast, Simmons and Hoskins (1976) concluded that the instability mechanism was rather insensitive to the choice of basic state when the prescribed meridional variation was larger than L , the Rossby radius of deformation. In this study, the growth rate is sensitive presumably because the meridional width of the frontal zone is close to L . This shift may explain much of the discrepancy between the most unstable wavelength, ~ 5700 km, of the lowest-order solution and the 3-4000 km wavelength of typical atmospheric wave-cyclones. The atmospheric cyclones usually form along a thermal front, which is not present in the lowest-order basic state. The growth rates are reduced when a purely barotropic wind field (which from classical arguments should lead to barotropic amplification) is added to the purely baroclinic lowest-order basic current. It is the U_{1YY} interior integral in (13) from (21) that generally reduces the growth rate for the prescribed flow profiles examined in this article. For the middle waves (with zonal wavelength between the long- and short-wave cut-prescribed flow profiles examined in this article. For the middle waves (with zonal wavelength between the long- and short-wave cut-offs), the phase speed is generally reduced by the presence of the horizontal shear. These negative values of the phase speed also arise

primarily from the interior integral. Hence, the positive potential vorticity gradient (as did the planetary vorticity gradient here) reduces the growth rate and phase speed. The ageostrophic terms tended to reduce both the growth rate and phase speed. The main source of these changes was the divergence term (through its second-order components) in the vorticity equation. The reduction of the growth rate agrees with Derome and Dolph (1970), but the reduction of the phase speed does not. Apparently, this disagreement arises because the model used here is fully compressible while theirs is not.

The discussion of the amplitude and phase of the solutions centered around those solutions obtained for a specific choice of the parameters. These solutions were considered to be representative of the results for the middle waves. Some features of the total solution, where $\alpha = 2.0$, $\beta = 1$, and $\underline{a} = 1.6$ for the Surface Front case with the ageostrophic terms included, are summarized in Fig. 29. The quantities in this figure include all the first- and second-order parts of the perturbation series solution. It was found that the amplitude of the wave was generally increased in the vicinity of the front, whether the front was confined near the surface or near the top. In turn, this changes the meridional scale of the wave. As the prescribed cross-frontal scale was reduced, the meridional scale of the wave decreased accordingly. The coordinate transform introduced two recognized non-geostrophic changes in the structure noted before by Hoskins (1975). First, because the mean zonal velocity increased with height, the geostrophic changes in the structure noted before by Hoskins (1975). First, because the mean zonal velocity increased with height, the transform introduced a poleward tilt with height of the trough and ridge axes. Second, the transform caused the horizontal areas of low

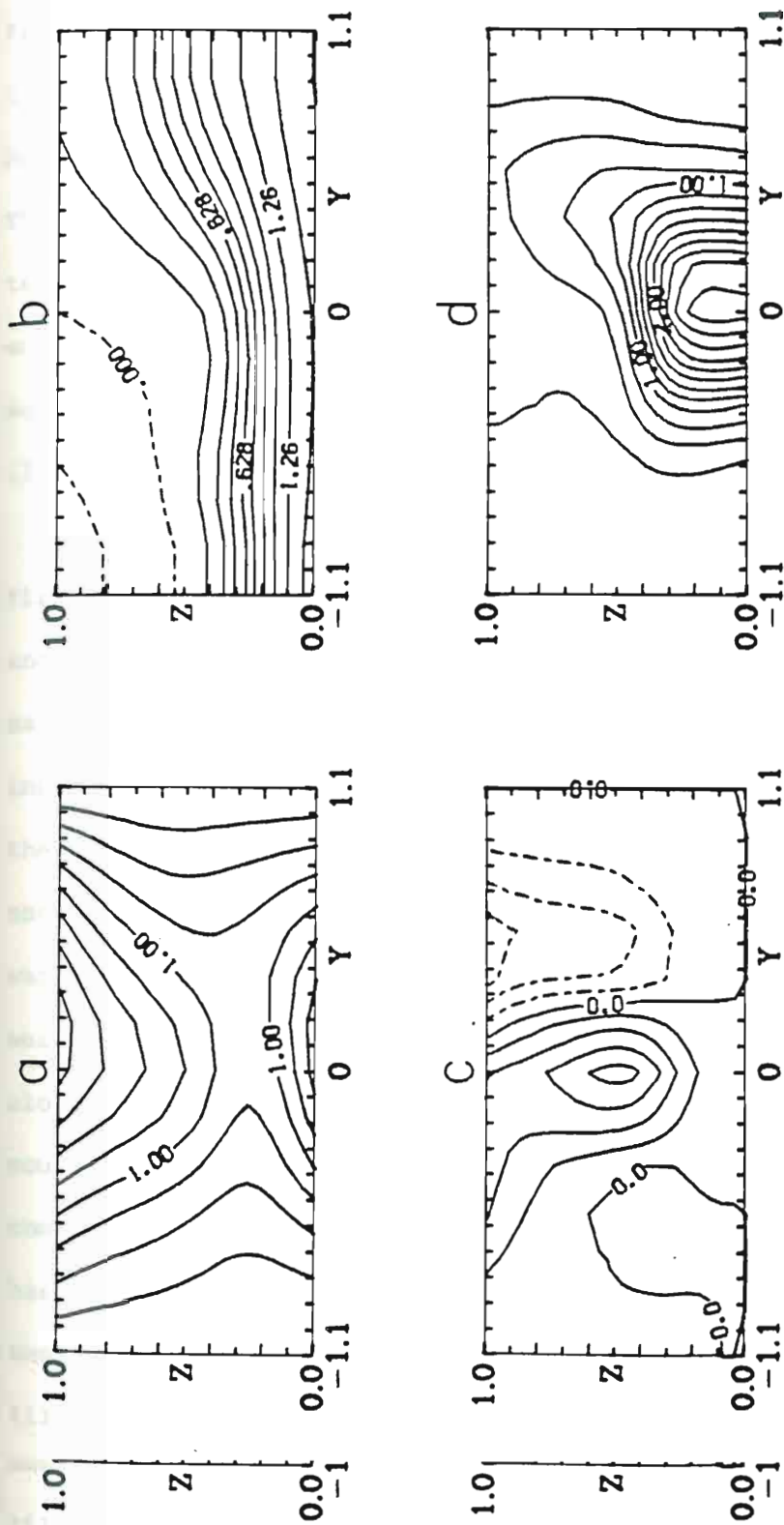


Fig. 29 The structure in geostrophic coordinates of the total Surface Front case solution including all ageostrophic terms, where $\alpha = 2.0$, $a = 1.6$ and $\beta = 1$. Cross sections are presented of: a) the pressure amplitude, b) the pressure phase, c) the barotropic energy conversion ($K_Z + K_E$) and d) the total barotropic energy conversion ($A_Z + A_E$). The meridional asymmetry is caused by the ageostrophic terms. This figure is discussed in more detail in the text. The contour intervals are $.05\pi$ in b, and $.25$ in a, c and d.

and high pressure to shrink and expand respectively. Both of these features are observed in the atmosphere. Without using a coordinate transform, the former ageostrophic effect was found by Derome and Dolph (1970) and the latter was obtained by Saltzman and Tang (1972). The ageostrophic terms, again primarily those from the divergence term, introduced meridional asymmetry into the solution. These terms enhanced the amplitude north of the center and diminished it to the south. The total perturbation pressure amplitude depicted in Fig. 29a illustrates some of these structural properties.

The thermal front altered the phase of the wave in two ways. First, the westward tilt with height was increased near the surface and decreased near the top. This latter effect became more prominent as the depth of the region of strong prescribed horizontal shear increased. Secondly, there was horizontal shear associated with the thermal front which was barotropically unstable. This produced horizontal tilts of the trough and ridge axes--southeast-northwest equatorward, and southwest-northeast poleward of the center. These tilts were generally greatest where the horizontal shear was greatest, except along the vertical boundaries. The non-geostrophic terms created a southwest-northeast tilt across the domain. Therefore the solution combining the Surface Front and ageostrophic effects, from Fig. 29b, has very little horizontal tilt south of the center (that is, the axes are nearly north-south aligned) and strong southwest-northeast tilt to the north. In addition, the westward tilt with height is axes are nearly north-south aligned) and strong southwest-northeast tilt to the north. In addition, the westward tilt with height is strongest in the lower half of the domain equatorward of the center.

The momentum flux calculated for this model compared favorably with the observed atmospheric distribution (e.g., Newell et al., 1972), when the ageostrophic terms were included.¹¹ The front produced a dipole pattern of the poleward momentum flux for the quasi-geostrophic eddy. The ageostrophic terms helped create a single, large region of positive momentum flux, and produced maximum values at the top of the domain.

Energy conversions were calculated for the four cases and for the ageostrophic terms. These conversions revealed the connection between the properties of the basic state and the stability and structure of the eddy. The role of the thermal front in the energy conversions was elaborated upon in Chapter 5. Briefly, the barotropic conversion ($\overline{K_Z} \rightarrow K_E$) conformed with one's expectations based upon classical potential vorticity arguments. The regions of positive barotropic conversion corresponded fairly well with the regions of positive q_y , the basic state potential vorticity gradient, even though q_y had vertical as well as meridional structure (compare Figs. 11 and 21). The regions did not correspond exactly because of the vertical dependence in the basic current. Specifically, the vertical boundary conditions reduced the momentum convergence in three of the cases and enhanced it slightly in the Upper Front case. Since these departures from pure barotropic instability theory arose from the baroclinic nature of the zonal flow, it followed that the presence of

¹¹The poleward heat flux and momentum flux for the Surface Front case, with baroclinic nature of the zonal flow, it followed that the presence of

¹¹The poleward heat flux and momentum flux for the Surface Front case, with and without the ageostrophic terms, are presented in Appendix I.

a baroclinically unstable flow inhibited the barotropic instability mechanism. This conclusion depended, in part, upon the questionable $w = 0$ boundary condition at the top, but that dependence actually reduced the inhibition. This conversion was weakest in the Upper Front case and strongest in the Barotropic case. The ageostrophic terms discussed in Chapter 6 responded to the lowest-order basic current which had only vertical variation. Though the volume-averaged barotropic conversion by the ageostrophic terms was zero, the zonal average did not vanish. The non-geostrophic barotropic conversion was asymmetric and largest at the top. These terms tended to create a jet in the basic state flow poleward of the meridional center. This result seems to be consistent with a study by Hollingsworth (1975) using a 2-layer model. The combined ageostrophic and Surface Front barotropic conversion is shown in Fig. 29c (compare with Figs. 21c and 25c). The large positive conversion in the middle is due to the horizontal shear associated with the thermal front. The negative conversion to the north is due to both the vertical boundary conditions (the baroclinic inhibition) and the ageostrophic terms. In contrast, the conversion for $Y < -.4$ is weak because the vertical boundary terms and ageostrophic terms oppose each other. Like the explicit ageostrophic terms, the nonlinear coordinate transform added positive conversion south of the center and negative conversion to the north when the wave had finite amplitude. This distribution is opposite to that created by the transform when the wave amplitude is infinitesimal when the wave had finite amplitude. This distribution is opposite to that created by the transform when the wave amplitude is infinitesimally small.

The lowest-order baroclinic conversion $(\overline{A_Z \rightarrow A_E})$ was largest at the top. The second-order poleward heat flux was largest and positive in the vicinity of the front. The baroclinic conversion created by the front was small in the Upper Front case and largest in the Surface Front case. However, the reduction of the westward tilt of the trough and ridge axes near the top reduced the baroclinic conversion at high levels. This reduction was a consequence of the barotropically unstable aspect of the basic current. This effect is a function of the vertical integral of q_y , so it is largest in the Barotropic case and least in the Upper Front case. Therefore, after examination of the quasi-geostrophic energy conversions $(\overline{K_Z \rightarrow K_E})$ and $(\overline{A_Z \rightarrow A_E})$, it was concluded that the baroclinic and barotropic instability mechanisms tend to inhibit each other. A mathematical explanation of this conclusion can be gleaned from Charney and Stern (1962) or Held (1975). In the Barotropic case, the second-order changes to the volume average baroclinic conversion were negative and exceeded the positive barotropic conversion, thus explaining the reduction of the growth rates. The thermal fronts increased the growth rates because the front introduced additional vertical shear and thus additional baroclinic instability. The combined ageostrophic and Surface Front baroclinic conversion $(\overline{A_Z \rightarrow A_E})$ is shown in Fig. 29d (compare with Figs. 8, 22c and 25d). The large positive conversion near the center bottom is due to the surface thermal front in the basic state. The asymmetric terms introduced a strong conversion near the center bottom is due to the surface thermal front in the basic state. The asymmetric terms introduced a strong equatorward heat flux at high levels south of the center and a smaller poleward heat flux near the surface north of the center.

The coordinate transformation appeared to have little effect upon the baroclinic conversion aside from introducing a poleward tilt with height.

One way of interpreting the results of this study is that they resolve some questions regarding the solutions obtained by Eady (1949). One question was addressed earlier; namely, Why is the most unstable wavelength in Eady's model much longer than the typical wavelength of atmospheric wave-cyclones? The answer was that even the presence of a weak front with small cross-frontal scale shifts the most unstable wavelength to shorter waves. Another question that one might consider is: Why are his calculated growth rates so good? Eady's problem only incorporates the baroclinic instability mechanism, and the basic current he chooses is simple, but not wildly unrepresentative of the atmosphere. A simplistic argument might be made that, because strong horizontal shear associated with the jet stream and in situ processes like latent heat release occur in the atmosphere, perhaps the growth rates would be much too large if all the major mechanisms were included in a model. One way to reduce the growth rate is to include the planetary vorticity gradient, another way is to include ageostrophic terms. Diabatic processes were not considered in this study, but Johnson (1970) has summarized some observational studies of their role. For example, it seems that latent heating may become important only after the cyclone reaches a mature stage. Brown (1969b) found that a simulation of small-scale latent heating may become important only after the cyclone reaches a mature stage. Brown (1969b) found that a simulation of small-scale eddy momentum and heat diffusion processes reduced the growth rate. The barotropic instability mechanism was considered in this study,

and while it introduced some tendency for growth, the simultaneous operation of the baroclinic and barotropic instability mechanisms tended to inhibit each other. The reason why these two processes do not linearly add together can be simply stated: the most efficient structures for the two processes of energy conversion are different. Since the structure of the wave lies somewhere between these two when both processes operate together, both conversion processes are not operated as efficiently as either can be when it operates alone.

In the experiments discussed in this study, the baroclinic and barotropic instability mechanisms tended to inhibit each other. A more general way of stating this conclusion is that the baroclinic and barotropic instability mechanisms are not independent. The results of this study complement the discussions of (26) and (25) by Charney and Stern (1962) and Held (1975), respectively. In one sense, those relations show that the two instability mechanisms compete for the basic state forcing. This study also complements the recent work by Lindzen et al., (1979) which reveals an underlying connection between the mechanisms, a connection suspected by Kuo thirty years earlier. Finally, this study demonstrates that the connection between baroclinic and barotropic instability must be recognized in order to properly analyze problems where both mechanisms can operate.

APPENDIX A

Total Adjoint Operator

We wish to find the adjoint operator for a total differential operator which includes the operator valid in the interior of the domain and the operator(s) valid along the boundaries. Let $\mathcal{L}^{(1)}$ designate that total operator

$$\mathcal{L}^{(1)} u = \begin{cases} Lu & \text{interior} \\ B_i u & \text{along each } i \text{ boundary} \end{cases}$$

Let L be a second-order partial differential equation of the form

$$L = \frac{\partial^2}{\partial Z^2} + d \frac{\partial}{\partial Z} + e + f \frac{\partial^2}{\partial Y^2}$$

in a rectangular Y, Z domain S .

Let $B_i = 0$ along the $Y = \text{constant}$ boundaries

and $B_i = -\frac{\partial}{\partial Z} + c$ along the $Z = \text{constant}$ boundaries, B .

For convenience, we choose c, d, e and f to be complex constants.

Let us use angle brackets to denote the inner product for the total operator and curved brackets for the inner product of each component operator, thus:

component operator, thus:

$$\langle u, v \rangle = (u, v)_S + (u, v)_B$$

The adjoint operator, denoted by $\mathcal{L}^{(2)}$, must satisfy

$$\langle \mathcal{L}^{(1)} u, v \rangle = \langle u, \mathcal{L}^{(2)} v \rangle$$

for any arbitrary u and v .

From the definition of the inner product, we can write

$$\langle \mathcal{L}^{(1)} u, v \rangle = \int v \overline{L u} dS + \int v (-\overline{u}_Z + \overline{c u}) dB$$

where the overbar indicates the conjugate. (Recall that the first term of the inner product is conjugated in the integrand.) Integrate by parts twice with respect to Y and Z , and use the Dirichlet boundary conditions ($u = 0$) along the $Y = \text{constant}$ boundaries. One obtains

$$\langle \mathcal{L}^{(1)} u, v \rangle = \int (\overline{u}_Z v - \overline{u} (v_Z - \overline{d} v)) dB + \int \overline{u} L^* v dS + \int v (-\overline{u}_Z + \overline{c u}) dB$$

where L^* is the conjugate adjoint of L , that is¹

$$L^* = \frac{\partial^2}{\partial Z^2} - \overline{d} \frac{\partial}{\partial Z} + \overline{e} + \overline{f} \frac{\partial^2}{\partial Y^2}$$

A term in the first integral cancels one in the third leaving

¹ Recall that the real operator $P\phi'' + Q\phi' + R\phi = 0$ has the adjoint $P\psi'' + (2P' - Q)\psi' + (P'' - Q' + R)\psi = 0$, where the primes denote

¹ Recall that the real operator $P\phi'' + Q\phi' + R\phi = 0$ has the adjoint $P\psi'' + (2P' - Q)\psi' + (P'' - Q' + R)\psi = 0$, where the primes denote differentiation. This formula, of course, is reproduced by the integration by parts.

$$\langle \mathcal{L}^{(1)}_{u,v} \rangle = \int \bar{u} L^* v dS + \int \bar{u} (-v_Z - \bar{d}v + \bar{c}v) dB \equiv \langle u, \mathcal{L}^{(2)}_v \rangle$$

We can immediately see what $\mathcal{L}^{(2)}$ must be:

For

$$\mathcal{L}^{(1)}_u = \begin{cases} Lu & \text{in } S \\ -u_Z + cu & \text{along } B \\ 0 & \text{along } Y = \text{constant boundaries,} \end{cases}$$

$$\langle \mathcal{L}^{(1)}_{u,v} \rangle = \langle u, \mathcal{L}^{(2)}_v \rangle \text{ if}$$

$$\mathcal{L}^{(2)}_v = \begin{cases} L^* v & \text{in } S \\ -v_Z + \bar{d}v + \bar{c}v & \text{along } B \text{ (} Z = \text{constant boundaries)} \\ 0 & \text{along } Y = \text{constant boundaries.} \end{cases}$$

In my specific application, if a nontrivial homogeneous solution for $\mathcal{L}^{(1)}$ exists, then $\mathcal{L}^{(2)}$ also has a nontrivial homogeneous solution. This may be true in general. $\mathcal{L}^{(2)}$ also allows us to write the orthogonality condition (13) as a prescription for c in terms of known quantities.

APPENDIX B

Numerical Determination of ϕ_1

The second term in the asymptotic series of the perturbation pressure is obtained by direct numerical solution of the heterogeneous Poisson equation. Since matrices and finite differences are used instead of continuous differential operators, some special care must be taken to make the problem completely consistent in terms of matrix operations. In other words, a formulation which is appropriate and consistent for the continuous equations is not necessarily so for its discrete analog. Thus, before one can solve for $\hat{\phi}_1$, both the matrix of coefficients (call it M) representing the total homogeneous operator and the forcing function matrix (call it F) must be carefully defined.

The homogeneous system of equations has a nontrivial solution; it is just the first term in the asymptotic series. This was accomplished by a special choice of the free constant, c_0 . Since a homogeneous solution exists, the corresponding coefficient matrix must be singular. But, while the analytically determined c_0 is a good guess, there is no guarantee that it will cause the coefficient matrix (determined by finite differences) to be singular to machine accuracy. So, an iterative procedure is used to find the appropriate c_0 for the coefficient matrix M using the analytic c_0 as a first guess. The analytic c_0 may make M singular to 10^{-4} or 10^{-5} but this error could be corrected by an iterative procedure. The coefficient matrix M using the analytic c_0 as a first guess. The analytic c_0 may make M singular to 10^{-4} or 10^{-5} , but this error could

be greatly magnified in the calculation of $\hat{\phi}_1$. So, it is important to find the c_0 which makes the matrix singular to machine accuracy, $< 3 \times 10^{-16}$. As a check, we should expect the change in c_0 to be small, and in practice it has been $\sim .01\%$.

Since the homogeneous form of the equation has a nontrivial solution, the heterogeneous terms must be orthogonal to the solution of the conjugate of the adjoint system of equations. We know the analytic form of the adjoint operator (see Appendix A). The matrix equivalent of the adjoint operator is the conjugate transpose of the matrix M , call it M^* . It would be wrong, in general, to form M^* from the continuous adjoint operator in the same fashion as the coefficient matrix M was formed from the homogeneous operator. In fact, the conjugate transpose matrix M^* may not correspond to any continuous differential operator. Therefore, once the problem has been placed in matrix form, all manipulations should be performed in matrix form to guarantee consistency.

In the continuous problem, the second-order orthogonality condition for the heterogeneous terms was satisfied by the precise choice of c_1 . In the matrix formulation we must insure that the forcing terms be orthogonal in a matrix sense. We have two choices: 1) we can iterate to find a new c_1 or 2) we can "project" the forcing function as a whole. In this study the second method was chosen. The following projection of the forcing function is made:

ing projection of the forcing function is made:

$$\hat{F} = F - \left[\frac{\phi_r^* F}{\phi_r^* \phi_r} \right] \phi_r \quad (B1)$$

where ϕ_r is the normalized right eigenvector of M and therefore corresponds to the solution of the homogeneous adjoint system of equations (i.e., $M^* \phi_r = 0$). The star signifies the conjugate transpose. The matrix F incorporates the forcing terms from the interior (F_1) and those from the boundary conditions (B_1). As a check, we should expect the correction to F to be small and in practice it is: for a 47×47 matrix, F was altered by .1% or less. The method of iterating c_1 is unsatisfactory because the forcing function matrix is not very sensitive to the value of c_1 in this problem. The procedure yielded iterated values for c_1 that were significantly different from the analytic values. Thus, the use of the iterated c_1 may imply that a significantly different problem is being solved. However, it was found that the broad features of the solution $\hat{\phi}_1$ were not altered by quite different choices for c_1 .

There are also two choices for defining the forcing function. We can formulate it from the analytic expressions for ϕ_0 or we can use the left eigenvector of M . Both approaches were tried and essentially no difference was found in the results. This means that the third-order forcing function could be calculated using the $\hat{\phi}_1$ matrix, and so forth for the higher orders. The analytic expressions for $\hat{\phi}_0$ were used in all the second-order calculations shown here.

The matrix equation
for $\hat{\phi}_0$ were used in all the second-order calculations shown here.

The matrix equation

$$\phi_1 = M^{-1} \hat{F} \quad (B2)$$

is used to compute ϕ_1 . Since M is singular, one might anticipate that calculating its inverse would be difficult. This was not the case. The heterogeneous solution was unaffected (to at least three digits) whether M was singular to 10^{-4} or 10^{-15} , for example. However, the projection (B1) is imperfect because ϕ_r^* could only be computed to 12 digits of accuracy. Thus, the homogeneous solution, multiplied by an arbitrary complex constant, is still present in the answer after calculation of (B2). The homogeneous solution is removed by projecting the answer:

$$\hat{\phi}_1 = \phi_1 - \frac{\phi_\ell^* \phi_1}{\phi_\ell^* \phi_\ell} \phi_\ell \quad (\text{B3})$$

where the heterogeneous solution $\hat{\phi}_1$ is the second term in the asymptotic series for the perturbation pressure and ϕ_ℓ is the left eigenvector.

APPENDIX C

The Geostrophic Correction Terms

The geostrophic correction terms appearing in (8) and (20) arise because the relations

$$u_g = -P_y \text{ and } v_g = P_x \quad (C1)$$

were used to define the geostrophic velocities used in the equations. While these relations (C1) are valid at the $O(1)$ level, there are $O(\mu)$, and higher, terms that arise from three sources. These sources are: 1) the scale height H is a function of Z , 2) the Coriolis parameter can vary; $\beta \neq 0$ and 3) the variation of the density in the perturbation and basic state. The terms arising from these sources are not contained in u_a and v_a but are explicitly written out in (8) and (20). This partition allows us to assume that the primary components of u_a and v_a arise from cyclostrophic balance, eliminating from (20) the u_a and v_a terms in (8).

Sources 1) and 2) manifest themselves in the advecting velocities in the semi-geostrophic coordinates as the f_1 and β terms, respectively. Sources 1) and 2) also contribute to the vorticity equation forcing function with the term

$$\mu \left\{ \left[d_2(u_g(f_1 - \beta y)) \right]_y - \left[d_2(v_g(f_1 - \beta y)) \right]_x \right\}$$

$$\mu \left\{ \left[d_2(u_g(f_1 - \beta y)) \right]_y - \left[d_2(v_g(f_1 - \beta y)) \right]_x \right\}$$

which can be written in geostrophic coordinates as

$$\mu \left\{ \beta \left[\Phi_{XY} \Phi_Y + 2\Phi_{XX} \Phi_X + \Phi_{YY} \Phi_X \right] - (f_1 - \beta Y) D_2 (\Phi_{XX} + \Phi_{YY}) \right\}.$$

Source 3) is manifest in the

$$-a_4 \mu \left[(u\rho)_x + (v\rho)_y \right] \tag{C2}$$

term in the vorticity equation forcing function (see Appendix E).

APPENDIX D

The Orthogonality Condition

Examine the orthogonality condition

$$\iint_S \phi^* \mathcal{L}(\hat{\phi}_1) dYdZ = \iint_S \phi^* F_1 dYdZ, \quad (D1)$$

where S represents the Y and Z domain and ϕ^* is the conjugate of the homogeneous solution to the total adjoint operator (see Appendix A). The X and T dependence has been factored from the orthogonality relation. For this problem, the total adjoint operator is

$$\left. \begin{aligned} L^* &= \epsilon \frac{\partial^2}{\partial Z^2} - a_6 \epsilon \frac{\partial}{\partial Z} - k^2 + \frac{\partial^2}{\partial Y^2} && \text{in } S \\ &0 && \text{at } Y = \pm Y_b \\ \frac{\partial}{\partial Z} - a_6 - \frac{U_{oZ}}{u_o - \bar{C}_o} &&& \text{at } Z = 0, 1 \end{aligned} \right\} (D2)$$

The overbar indicates the complex conjugate. Nontrivial homogeneous solutions exist both for the total operator (they are merely the first-order results of Section 4) and for the total adjoint operator (D2).

From (D2) we find

$$\phi^* = e^{a_6 Z} \hat{\phi}_0.$$

$$\phi^* = e^{a_6 Z} \hat{\phi}_0.$$

Integrating (D1) by parts, twice, one obtains

$$\int \left[\phi^* \hat{\phi}_{1Z} - \hat{\phi}_1 (\phi_Z^* + a_6 \phi^*) \right]_{Z=0}^{Z=1} dY + \int_0^1 \hat{\phi}_1 L^* (\phi^*) dY dZ = \iint_S \phi^* F_1 dY dZ$$

Using (D2) and $L^* (\phi^*) = 0$,

$$\int \left[\phi^* \left(\hat{\phi}_{1Z} - \frac{u_{0Z} \hat{\phi}_1}{u_0 - c_0} \right) \right]_{Z=0}^{Z=1} dY = \iint_S \phi^* F_1 dY dZ. \quad (D3)$$

The unknown $\hat{\phi}_1$ can be eliminated from the left-hand side of (D3) by using (12b). The heterogeneous terms in (12b) include a term involving c_1 .

$$c_1 \int \left[\frac{\phi^* \hat{\phi}_{0Z}}{u_0 - c_0} \right]_{Z=0}^{Z=1} dY + \int \phi^* B_1^* dY = \iint_S \phi^* F_1 dY dZ, \quad (D4)$$

where

$$B_1^* = \left\{ \psi_{1Y} \hat{\phi}_{0Z} - \hat{\phi}_0 \psi_{1YZ} + c_0 \beta Y \hat{\phi}_{0Z} + 2f_{10} u_{0Z} \hat{\phi}_0 - \hat{\phi}_0 u_0 (a_3 - f_{1Z}) - f_{10} \hat{\phi}_{0Z} u_0 \right\} / (u_0 - c_0) + (a_3 - f_{1Z}) \hat{\phi}_0 - f_{10} \hat{\phi}_{0Z}.$$

The orthogonality condition can now be arranged in the form (13) as a definition of c_1

$$c_1 = \left\{ \left[\frac{u_{0Z}}{u_0 - c_0} \int \phi^* \hat{\phi}_0 dY \right]_{Z=0}^{Z=1} \right\}^{-1} \left\{ \iint_S \phi^* F_1 dY dZ - \int \phi^* B_1^* dY \right\}.$$

APPENDIX E

Vertical Component Vorticity Equation Derivation

Define

$$\eta_3 = \xi_3 + \mu\sigma_3$$

where

$$\xi_3 = v_{gx} - u_{gy} \quad \text{and} \quad \sigma_3 = \frac{\partial(u_g, v_g)}{\partial(x, y)} = u_{gx}v_{gy} - u_{gy}v_{gx}$$

Using (5) and combining terms, the ξ_3 equation is obtained.

$$\begin{aligned} d_2(\xi_3) &= (d_2(v_g))_x - (d_2(u_g))_y - u_x v_{gx} - v_x v_{gy} + u_y u_{gx} + v_y u_{gy} \\ d_2(\xi_3) &= (1 + \mu\beta y)(w_z + a_7 w + a_4 \mu d_2 \rho) - \beta v - \mu w_x v_{gz} - \mu w v_{gxz} \\ &\quad + \mu w_y u_{gz} + \mu w u_{gyz} - u_x v_{gx} - v_x v_{gy} + u_y u_{gx} + v_y u_{gy} \\ &\quad - a_4 \mu [u \rho_x + v \rho_y] - \mu (d_2(v_a))_x + \mu (d_2(u_a))_y \\ &\quad - \mu [d_2(v_g(f_1 - \beta y))]_x + \mu [d_2(u_g(f_1 - \beta y))]_y \end{aligned}$$

A geostrophic correction term (C2) can be combined with the divergence term. Truncating at the $O(\mu)$ level:

$$\begin{aligned} d_2(\xi_3) &= \mu(\xi \cdot \nabla w) - \beta v + a_6 \mu w \xi_3 + (1 + \mu\beta y)(w_z - a_7 w) + a_4 \mu \rho_t \\ &\quad - \mu w \xi_{3z} - \mu \left\{ [d_2(v_a)]_x - [d_2(u_a)]_y \right\} - \mu [d_2(v_g(f_1 - \beta y))]_x \\ &\quad - \mu w \xi_{3z} - \mu \left\{ [d_2(v_a)]_x - [d_2(u_a)]_y \right\} - \mu [d_2(v_g(f_1 - \beta y))]_x \end{aligned}$$

$$+ \mu \left[d_2(u_g(f_1 - \beta y)) \right]_y - \frac{\partial(u, u_g)}{\partial(x, y)} - \frac{\partial(v, v_g)}{\partial(x, y)}. \quad (E1)$$

The last two terms in (E1) are eliminated by the σ_3 equation.

$$\begin{aligned} \mu d_2(\sigma_3) = & \frac{\partial(\mu d_2(u_g), v_g)}{\partial(x, y)} + \frac{\partial(u_g, \mu d_2(v_g))}{\partial(x, y)} - \mu \left\{ u_{gx} \frac{\partial(u, v_g)}{\partial(x, y)} \right. \\ & \left. + u_{gy} \frac{\partial(v, v_g)}{\partial(x, y)} + v_{gx} \frac{\partial(u_g, u)}{\partial(x, y)} + v_{gy} \frac{(u_g, v)}{(x, y)} \right\} \end{aligned}$$

Use (5d) and (5e) and truncate at the $O(\mu)$ level to obtain

$$\begin{aligned} \mu d_2(\sigma_3) = & [v_x v_{gy} - v_{gx} v_y + u_{gy} u_x - u_{gx} u_y](1 + \mu \beta y) - \mu \beta v v_{gx} \\ & - \mu \beta u u_{gx} - \mu \left[u_x \frac{\partial(u_g, v_g)}{\partial(x, y)} + v_y \frac{\partial(u_g, v_g)}{\partial(x, y)} \right] \end{aligned}$$

This can be reduced to

$$\begin{aligned} \mu d_2(\sigma_3) = & \frac{\partial(v, v_g)}{\partial(x, y)} + \frac{\partial(u, u_g)}{\partial(x, y)} - \mu \beta [v v_{gx} + u u_{gx}] \\ & + \mu \beta y \left[\frac{\partial(v, v_g)}{\partial(x, y)} + \frac{\partial(u, u_g)}{\partial(x, y)} \right] \end{aligned} \quad (E2)$$

Combine (E1) and (E2) to obtain (6):

$$\begin{aligned} d_2(\eta_3) = & \mu(\xi \cdot \nabla w) - \beta v + a_6 \mu w \xi_3 + (1 + \mu \beta y)(w_z + a_7 w) - \mu w \xi_{3z} \\ & + a_4 \mu \rho_t - \mu [d_2(v_a)]_x + \mu [d_2(u_a)]_y - \mu [d_2(v_g(f_1 - \beta y))]_x \\ & + \mu [d_2(u_g(f_1 - \beta y))]_y - \mu \beta [v v_{gx} + u u_{gx}] \end{aligned} \quad (E3)$$

$$+ \mu [d_2(u_g(f_1 - \beta y))]_y - \mu \beta [v v_{gx} + u u_{gx}] \quad (E3)$$

Transform (E3) into geostrophic coordinates (7a) term by term.

The following relations are useful

$$\begin{aligned} \frac{\partial}{\partial t} &= \frac{\partial}{\partial T} + Q \frac{\partial}{\partial X} + N \frac{\partial}{\partial Y}, \quad \frac{\partial}{\partial x} = (1 + I) \frac{\partial}{\partial X} + J \frac{\partial}{\partial Y} \\ \frac{\partial}{\partial y} &= J \frac{\partial}{\partial X} + (1 + K) \frac{\partial}{\partial Y}, \quad \frac{\partial}{\partial z} = M \frac{\partial}{\partial X} + B \frac{\partial}{\partial Y} + \frac{\partial}{\partial Z} \end{aligned} \quad (E4)$$

where

$$\begin{aligned} Q &= \mu \Phi_{XT}, \quad N = \mu \Phi_{YT}, \quad I = \mu \Phi_{XX}, \quad J = \mu \Phi_{XY}, \\ K &= \mu \Phi_{YY}, \quad M = \mu \Phi_{XZ}, \quad B = \mu \Phi_{YZ}. \end{aligned}$$

Truncate each term at $O(\mu)$ and use (7c):²

$$d_2(\xi_3) = D_2 \left[\Phi_{XX} + \Phi_{YY} + \mu(\Phi_{XX})^2 + \mu(\Phi_{XY})^2 + \mu(\Phi_{YY})^2 \right] \quad (E5)$$

$$\mu d_2(\sigma_3) = \mu D_2 \left[\Phi_{YY} \Phi_{XX} - (\Phi_{XY})^2 \right] \quad (E6)$$

$$w_z + \mu(\xi \cdot \nabla w) = w_z + \mu(\Phi_{XX} + \Phi_{YY}) w_z \quad (E7)$$

since from (5a) and (5c), w involves only derivatives of P . It is understood that the w_z on the right-hand side of (E6) is a function of Φ .

$$-\beta v = -\beta v_g (1 - \mu \beta Y + \mu f_1) - \mu \beta D_2(u_g) = -D_2(\beta Y + \mu \beta u_g) \quad (E8)$$

$$a_6 \mu w \xi_3 = a_6 \mu w (\Phi_{XX} + \Phi_{YY}) \quad (E9)$$

$$\mu \beta Y (w_z + a_6 w) = \mu \beta Y (w_z + a_6 w) \quad (E10)$$

²Note that the total derivative (following a parcel) of any quantity

²Note that the total derivative (following a parcel) of any quantity in geostrophic coordinates equals the total derivative of that quantity in Cartesian coordinates.

Recall that from (5a)

$$\theta = \phi_Z - \mu\phi(a_3 - f_{1Z}) + \mu f_1 \phi_Z + O(\mu^2)$$

So,

$$a_7 w = -a_7 \epsilon D_2(\phi_Z) - a_6 \mu \epsilon D_2(f_1 \phi_Z - (a_3 - f_{1Z})\phi) + a_6 \mu \epsilon^2 \phi_{ZZ} D_2(\phi_Z) \quad (E11)$$

$$-w \xi_{3z} = -\mu w (\phi_{XXZ} + \phi_{YYZ}) \quad (E12)$$

$$a_4 \mu \rho_t = a_4 \mu (a_5 \alpha \phi - \phi_Z)_T \quad (E13)$$

$$-\mu \beta [v v_{gx} + u u_{gx}] = -\mu \beta [\phi_X \phi_{XX} - \phi_Y \phi_{XY}] \quad (E14)$$

and

$$\begin{aligned} -\mu [d_2(v_g(f_1 - \beta y))]_x + \mu [d_2(u_g(f_1 - \beta y))]_y = \\ -\mu (f_1 - \beta y) D_2(\phi_{XX} + \phi_{YY}) + \mu \beta [\phi_{XY} \phi_Y + 2\phi_{XX} \phi_Y + \phi_{YY} \phi_X] \end{aligned} \quad (E15)$$

This leaves the ageostrophic velocity term. If we assume that ageostrophic velocities are primarily due to cyclostrophic balance, then this term will not enter into the calculation of the first- and second-order solutions. The transform of this term is indicated symbolically in (8) as

$$-\mu \left\{ [d_2(v_a)]_x - [d_2(u_a)]_y \right\} = \mu D(v_a, u_a) \quad (E16)$$

Relations (E5) - (E16) are substituted in (E3) and rearranged so that only the $O(\mu)$ terms (other than those from the definition of D_2) appear on the right-hand side. By combining and transforming that only the $O(\mu)$ terms (other than those from the definition of D_2) appear on the right-hand side. By combining and transforming (5a) and (5c), w is expressed in terms of ϕ .

$$w = -\epsilon D_2(\Phi_Z) + \mu \epsilon \left\{ (a_3 - f_{1Z}) \Phi_T - f_1 D_2(\Phi_Z) + \epsilon \Phi_{ZZ} D_2(\Phi_Z) \right\} \quad (E17)$$

and

$$w_Z = -\epsilon D_2(\Phi_{ZZ}) - \epsilon \mu \left\{ (a_3 - 2f_{1Z}) \Phi_{ZT} + (\epsilon \Phi_{ZZ} - f_1) D_2(\Phi_{ZZ}) \right. \\ \left. + \epsilon \Phi_{ZZZ} D_2(\Phi_Z) - 2f_{1Z} (u_g \Phi_{ZX} + v_g \Phi_{ZY}) \right\} \quad (E18)$$

Relations (E17) and (E18) are substituted for w and w_Z to obtain (8). The relation (E17) is used for the boundary conditions $w = 0$ at $Z = 0, 1$.

APPENDIX F

The Static State

The prescription of the static state is important because the vertical variations of P , θ , T and ρ are dominated by the variations of the static state variables (3). There is some flexibility in how we choose the static state, despite a half-dozen restrictions imposed to make the problem solvable. In this report, a particular static state which closely models the USSA will be employed.

Much of the flexibility mentioned above arises from the realization that small changes in the static state density field can cause large changes in the static stability, κ . One can obtain analytically solvable lowest-order versions of (8) for various variations of κ , from cases where κ increases slightly with height to cases where it decreases dramatically with height. From the definition (2b) of ϵ , it is clear that the problem can be significantly altered by markedly different choices of κ .

The particular static state used here is patterned after the USSA. It is assumed that the USSA is representative of the typical average atmospheric conditions present during incipient wave-cyclone development. This state is contrasted with an isothermal state, where κ is constant but about three times larger, in Fig. 1.

The specific choice of ρ_s is
where κ is constant but about three times larger, in Fig. 1.

The specific choice of ρ_s is

$$\rho_s(z) = 1.1 e^{-z/D} + .134(1 - \frac{.9}{D} z) + O(\mu^2) \quad (F1)$$

where $D = 10$ km is the height of the domain. From the hydrostatic relation

$$P_s(z) = g \left[1.1 e^{-z/D} - \frac{.134}{D} (z - \frac{.45}{D} z^2) + O(\mu^2) \right] + \text{constant}. \quad (F2)$$

The $\theta_s(z)$ distribution can be obtained from a state equation. We will not need to know what the $O(\mu^2)$ parts of (F1) and (F2) are to solve the vorticity equation at the level we will truncate it. The constant in (F2) is chosen so that $P_s(0) = 1013$ mb. The static stability for this example is

$$\kappa = .14$$

and is independent of height.

The pressure scale height computed from (F1) and (F2), as for the USSA, is not constant but decreases with height.

$$\frac{P_s(z)}{\rho_s(z)g} = H \cdot (1 + \mu f_1(z) + \mu^2 f_2(z) \dots), \quad (F3)$$

where

$$H = \frac{P_s(0)}{\rho_s(0)g} \quad \text{and} \quad f_1 = \frac{-1.1}{D} z$$

$$H = \frac{P_s(0)}{\rho_s(0)g} \quad \text{and} \quad f_1 = \frac{-1.1}{D} z$$

is a reasonable choice for f_1 . The f_i are all assumed to vanish at the bottom. The higher-order corrections (f_i for $i > 1$) are not

needed here either. However, f_1 will appear in the hydrostatic relation (5a) and the horizontal momentum equations (5d) and (5e).

APPENDIX G

Scaling

The scaling arguments for P , ρ and θ developed below were generously provided by Dr. J. Pedlosky.

Assume the following relations hold:

$$P = P_s(z) \cdot (1 + \hat{P}'')$$

$$\rho = \rho_s(z) \cdot (1 + \hat{\rho}'')$$

$$\theta = \theta_s(z) \cdot (1 + \hat{\theta}'')$$

where the primes denote nondimensional quantities and \hat{P} , $\hat{\rho}$ and $\hat{\theta}$ are the as yet undetermined nondimensional scaling factors. Note that the static state variables satisfy

$$(P_s)_z = -\rho_s g$$

and

$$c_p \ln \theta_s = c_v \ln P_s - c_p \ln \rho_s. \quad (G1)$$

Let us anticipate that the horizontal pressure gradient will be of the order of the Coriolis acceleration; that is, the perturbation is in approximate geostrophic balance.

--- in approximate geostrophic balance ---

$$\frac{\hat{P}_s(z)}{L} (P')_{y'} = O(f_o V u' \rho_s). \quad (G2)$$

Assuming that u' and P' are $O(1)$, we use (G2) to define

$$\hat{P} = f_o V L \frac{\rho_s}{P_s} \approx \frac{V}{f_o L} \frac{f_o^2 L^2}{gH} = \mu \nu \kappa \epsilon. \quad (G3)$$

For the purposes of the scaling, the lowest order definition of H is adequate in (G3).

To obtain the density scaling factor, we anticipate that in the vertical direction the buoyancy force due to density departures $(\rho - \rho_s)$ caused by the motion field will be of the same order as the vertical pressure gradient. That is, we expect approximate hydrostatic balance for the eddy. Thus

$$\rho_s \hat{\rho} \rho' g = O\left[\frac{(P_s \hat{P} P')}{D} z\right] = \left[\frac{(\rho_s f_o V L)}{D} P'\right]_{z'}$$

using (G2). Again let P' and ρ' be $O(1)$ to get

$$\hat{\rho} = \frac{f_o V L}{gD} = \frac{V}{f_o L} \frac{f_o^2 L^2}{gD} = \mu \kappa \epsilon. \quad (G4)$$

Since \hat{P} , $\hat{\rho}$ and $\hat{\theta}$ are expected to be small, it follows from (1)

that

$$\begin{aligned} c_p \ln(\theta_s (1 + \hat{\theta}\theta')) &= c_p \ln\theta_s + c_p \ln(1 + \hat{\theta}\theta') \\ &= c_p \ln\theta_s + c_p \hat{\theta}\theta' + O(\hat{\theta}^2) \\ c_p \ln(\theta_s (1 + \hat{\theta}\theta')) &= c_p \ln\theta_s + c_p \ln(1 + \hat{\theta}\theta') \\ &= c_p \ln\theta_s + c_p \hat{\theta}\theta' + O(\hat{\theta}^2) \\ &= c_v \ln P_s + c_v \hat{P} P' - c_p \ln \rho_s - c_p \hat{\rho} \rho' + O(\hat{P}^2, \hat{\rho}^2). \end{aligned}$$

Using (G1) we may write

$$\hat{\theta}\theta' = \gamma\hat{P}P' - \hat{\rho}\rho' + o(\hat{\theta}^2, \hat{P}^2, \hat{\rho}^2) \quad (G5)$$

and to keep $\theta' = O(1)$ it is convenient to choose

$$\hat{\theta} = \hat{\rho} = \mu\kappa\epsilon. \quad (G6)$$

APPENDIX H

Some Mathematical Details

I. A derivation of (5a):

We can write (G5) as

$$\theta = a_s \gamma P - \rho + O(\mu^2). \quad (H1)$$

Write the vertical momentum equation as

$$g + \frac{(P_s (1 + \mu \nu \kappa \epsilon P'))_z}{\rho_s (1 + \mu \kappa \epsilon \rho')} + O(\mu^2) = 0. \quad (H2)$$

Multiply by δ/vf_0 and recall that $(P_s)_z = \rho_s g$ (dimensional), so that

$$g \left(1 - \frac{1}{(1 + \mu \kappa \epsilon \rho')} \right) + \frac{\mu \nu \kappa \epsilon (P_s P')_z}{\rho_s (1 + \mu \kappa \epsilon \rho')} = 0$$

truncated at $O(\mu)$. Use the definition of the scale height (2d) to get

$$\frac{g \mu \kappa \epsilon \rho'}{1 + \mu \kappa \epsilon \rho'} + \frac{\mu \kappa \epsilon g (\rho_s P' (1 + \mu f_1 + \dots))_z'}{\rho_s (1 + \mu \kappa \epsilon \rho')}.$$

Note that $g \kappa \epsilon \mu = v f_0 / \delta$ and divide by $(1 + \mu \kappa \epsilon \rho')$ to obtain

$$\rho' + (P')_{z'} + P' a_7 + \frac{\mu}{\rho_s} (\rho_s P' f_1)_{z'} = 0. \quad (H3)$$

$$\rho' + (P')_{z'} + P' a_7 + \frac{\mu}{\rho_s} (\rho_s P' f_1)_{z'} = 0. \quad (H3)$$

Note that f_1 is nondimensional. Using (H1) and (G1) we can rearrange (H3).

$$(P')_{z'} = \theta' - a_5 \gamma P' + P' D \left[(\ln \theta'_s)_{z'} - \gamma (\ln P'_s)_{z'} \right] - \frac{\mu}{\rho_s} (P' \rho'_s f_1)_{z'}$$

$$(P')_{z'} = \theta' + P' \kappa - P' \left[a_5 \gamma - \frac{D \rho'_s g \gamma}{P'_s} + \mu f_{1z'} + \mu P' f_1 (\ln \rho'_s)_{z'} \right] - \mu f_1 P'_{z'}$$

$$(P')_{z'} = \theta' + P' \left[\mu a_3 - \mu f_{1z'} + \mu f_1 \kappa \right] - \mu f_1 P'_{z'} + O(\mu^2)$$

Truncating at $O(\mu)$ we retrieve (5a)

$$(P')_{z'} = \theta' + \mu P' (a_3 - f_{1z'}) - \mu f_1 P'_{z'}$$

II. A derivation of (25) and (26)

This derivation is sketched in the article by Held (1975) and is repeated here for the convenience of the reader.

Let q' denote the total perturbation series of eddy potential vorticity; then the linearized quasi-geostrophic potential vorticity equation can be written

$$(q')_T = -U(q')_X - \mu v'(q_{1Y}), \quad (H4)$$

where $v' = \phi'_x$. Multiply by q' and average over X

$$\frac{1}{2} \overline{(q')^2}_T = -\mu \overline{v' q' (q_{1Y})}. \quad (H5)$$

Assume a solution to (H4) of the form $q' = \hat{q} \exp(ik(X - CT))$.

Assume a solution to (H4) of the form

$$q' = \text{Re} \left\{ \hat{q} \exp(ik(X - CT)) \right\}. \quad (H6)$$

Then substituting into (H4) (see pages 168-169, Charney and Stern, 1962, for more details), one gets

$$\overline{v'q'} = - \frac{kc_i}{2} \frac{|\hat{q}|^2}{\mu q_{1Y}} \exp(2kc_i T). \quad (H7)$$

Multiply q' (defined as equal to $\int_{\Delta}(\phi)$) by $\rho_s v'$ and average over X .

This can be written as

$$\rho_s \overline{v'q'} = -M + (h)_Z,$$

where M is defined by (25) and h by (26). To obtain (25) we integrate over the depth of the fluid. To obtain (26) we integrate from the surface to a height Z . The derivation of (26) is only slightly different from that for (25) so only the derivation of (25) need be shown.

Integrate over the depth of the fluid and use (H7):

$$\int_0^1 M dZ = \frac{kc_i}{2} \exp(2kc_i T) \int_0^1 \rho_s \frac{|\hat{q}|^2}{\mu q_{1Y}} dZ + h \Big|_0^1. \quad (H8)$$

Multiply the boundary conditions at $Z = 0, 1$ by $\rho_s \phi_Z$ and average over X

$$\frac{\rho_s}{2} \overline{(\phi_Z)^2} = \rho_s \overline{v' \phi_Z U_Z},$$

which is similar in form to (H5) thus

$$\overline{v' \phi} = \frac{kc_i}{2} \frac{\rho_s |\hat{\phi}_Z|^2}{\mu q_{1Y}} \exp(2kc_i T) \quad \text{at } Z = 0, 1.$$

$$\rho_s \overline{v' \phi_Z} = \frac{kc_i}{2} \frac{\rho_s |\hat{\phi}_Z|^2}{U_Z} \exp(2kc_i T) \quad \text{at } Z = 0, 1.$$

Substitute into (H8)

$$\int_0^1 M dz = \frac{kc_i}{2} \exp(2kc_i T) \left\{ \int_0^1 \frac{\rho_s |\hat{q}|^2}{\mu q_{1Y}} dz + \frac{\rho_s |\hat{\phi}_z|^2}{U_z} \Big|_0^1 \right\}. \quad (H9)$$

Return to (H4) and substitute in (H6) giving

$$(U - C)\hat{q} = -\hat{\phi} q_{1Y}. \quad (H10)$$

Also write the vertical boundary conditions as

$$(U - C)\hat{\phi}_z = -\hat{\phi} U_z \quad \text{at } z = 0, 1. \quad (H11)$$

Substitute (H10) and (H11) into (H9) to obtain (25):

$$\int_0^1 M dz = \frac{kc_i}{2} \exp(2kc_i T) \left\{ \int_0^1 \frac{\rho_s \mu |\hat{\phi}|^2}{|U - C|^2} q_{1Y} dz + \frac{\rho_s |\hat{\phi}|^2}{|U - C|^2} U_z \Big|_0^1 \right\}.$$

which is similar in form to (8b) in Held (1975).

APPENDIX I

Further Figures

The purpose of this appendix is to present some figures which expand upon the discussion in the main text. The figures were deemed inappropriate for the main text and are included here for the benefit of those readers who may wish to see more details.

The first set of plots (Fig. I-1) shows the growth rate and phase speed spectra for each of the four quasi-geostrophic cases obtained from the vertical boundary terms in (13) only. The contour interval of .1 is the same in each of these diagrams.

The second set of plots (Fig. I-2) shows the three energy conversions in a format similar to that in Fig. 23, but for the other three quasi-geostrophic cases. In each triplet, the contour intervals are .1 in the top diagram and .25 in the middle and bottom diagrams. These cross sections are in Cartesian coordinates.

The third set of plots (Fig. I-3) shows the real (left) and imaginary (right) parts of the eddy pressure ϕ_1 calculated for the three most important ageostrophic terms in (27) and (28) and the total for all the terms. The intent is to facilitate comparison with a solution of Derome and Dolph (1970). These cross sections are in geostrophic coordinates. The contour interval varies in the figures.

The plots composing Fig. I-4 show the changes in the poleward heat coordinates. The contour interval varies in the figures.

The plots composing Fig. I-4 show the changes in the poleward heat flux and momentum flux, for the Surface Front case, caused by the

ageostrophic terms. Again, $\alpha = 2.0$, $\underline{a} = 1.6$ and $\beta = 1$. In particular, the ageostrophic terms greatly improve the comparison between these ageostrophic terms greatly improve the comparison between these theoretical and observed atmospheric distributions of the momentum flux. In the atmosphere, a single, large region of positive momentum flux, with maximum value near the tropopause is often observed in middle latitudes (e.g., Newell et al., 1972). The ageostrophic terms have less effect upon the poleward heat flux.

The group of diagrams in Fig. I-5 may be compared with the solution discussed by McIntyre (1970), and they are presented to check the method of solution used here. Fig. I-5a compares quite favorably with Fig. 5 in McIntyre (1970). The poleward heat flux is $\overline{v'\theta'}$ and the momentum convergence is $-\overline{(u'v')_y}$. The comparison is not exact for several reasons, among them: 1) we define m differently, so we use different values for α , 2) we define the horizontal shape of the domain differently and 3) we sum 11 terms in the series while I only use the first two. Similar basic state profiles were used; in my results $\alpha = 2.0$, $\beta = 0$ and $a_7 = 0$. Fig. I-5b shows the baroclinic $(\overline{A_Z \rightarrow A_E})$ and barotropic $(\overline{K_Z \rightarrow K_E})$ energy conversions (not computed by McIntyre, 1970). The potential vorticity gradient for this basic state ($U = Z + .4\cos^2(mY)$) is positive between $\pm .55$, and negative elsewhere.

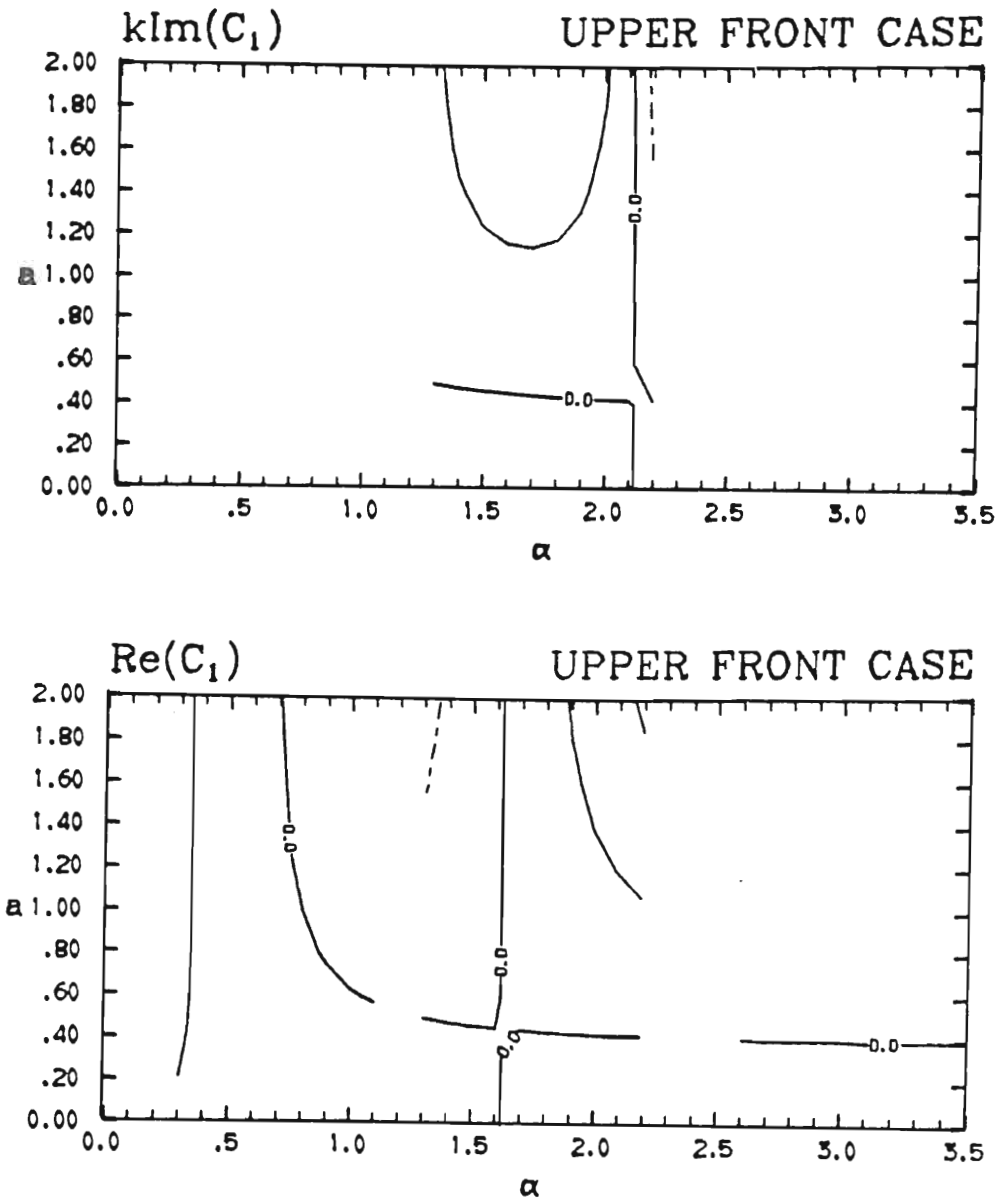


Fig. I-1a. Growth rate (upper diagram) and phase speed (lower diagram) spectra for the Upper Front case obtained by using only the vertical boundary terms in (13). The contour

Fig. I-1a. Growth rate (upper diagram) and phase speed (lower diagram) spectra for the Upper Front case obtained by using only the vertical boundary terms in (13). The contour interval is .1.

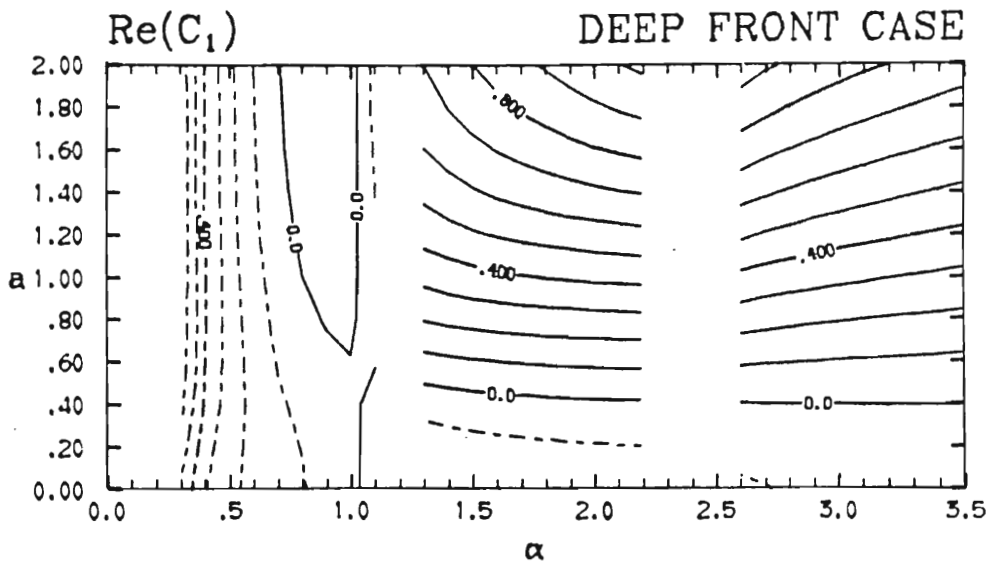
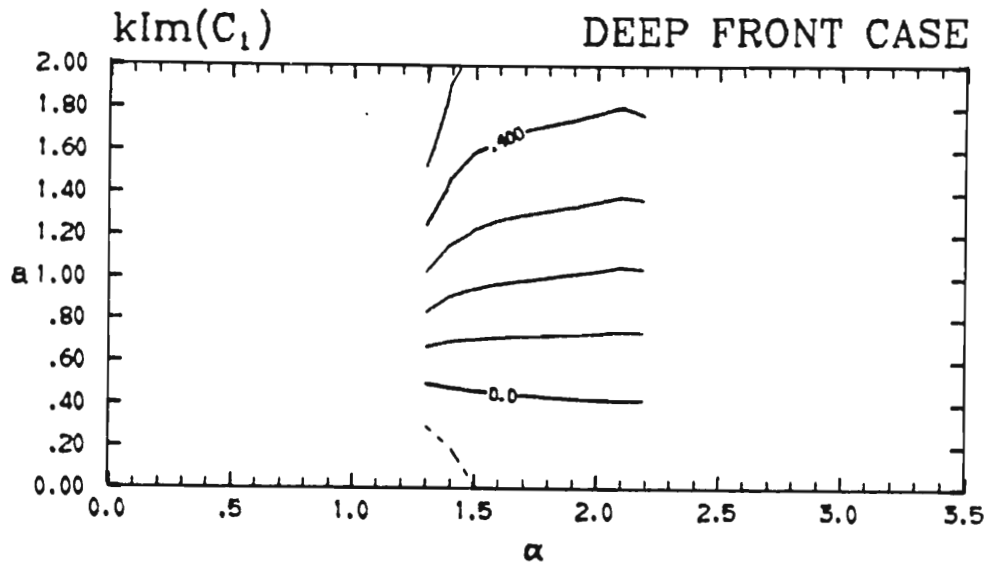


Fig. I-1b. Same as Fig. I-1a except for the Deep Front case.

Fig. I-1b. Same as Fig. I-1a except for the Deep Front case.

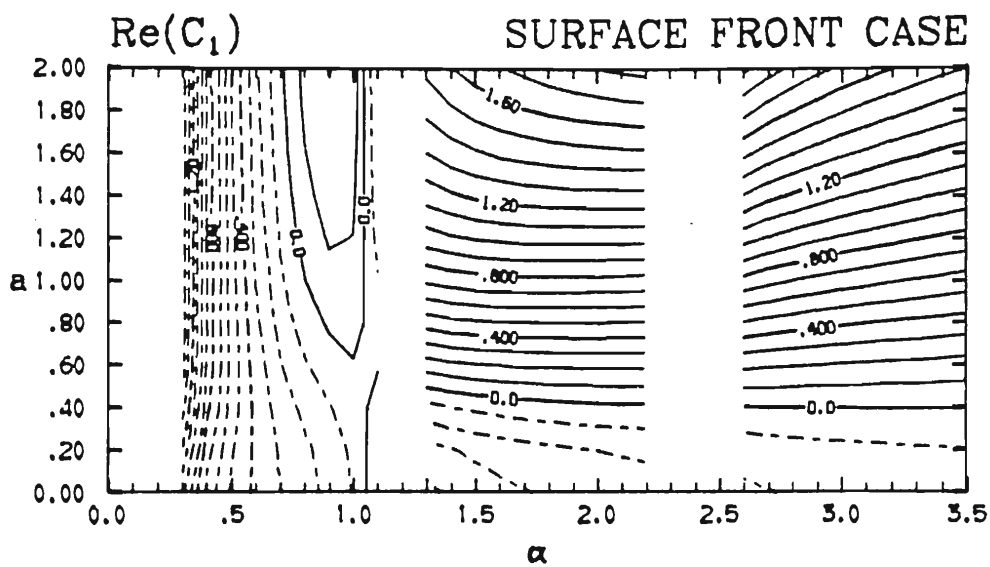
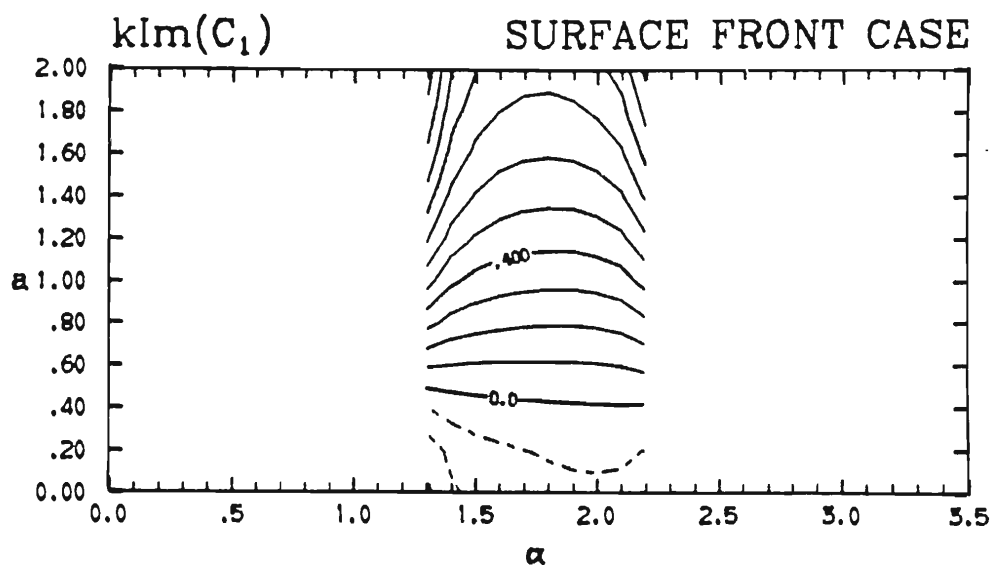


Fig. I-1c. Same as Fig. I-1a except for the Surface Front case.

Fig. I-1c. Same as Fig. I-1a except for the Surface Front case.

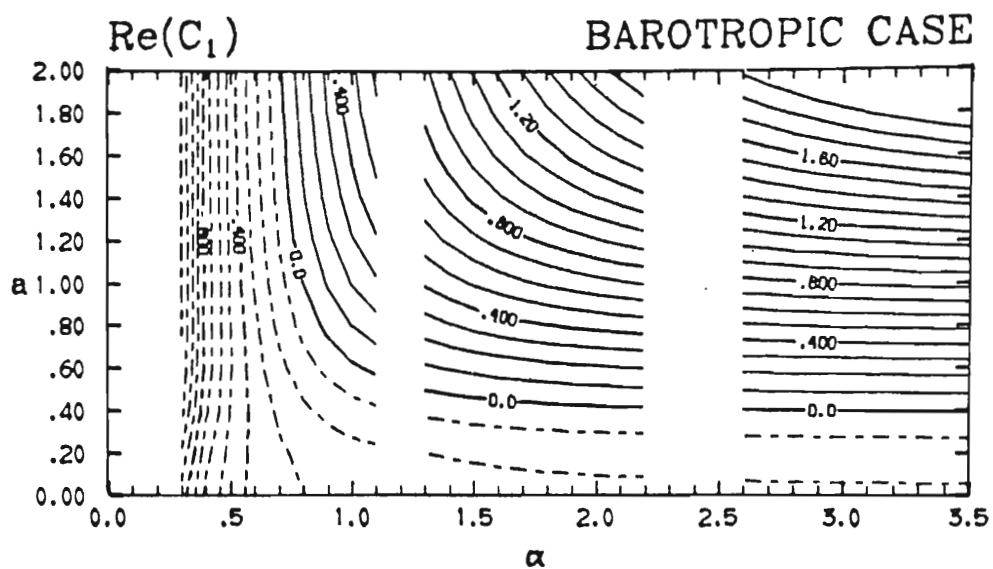
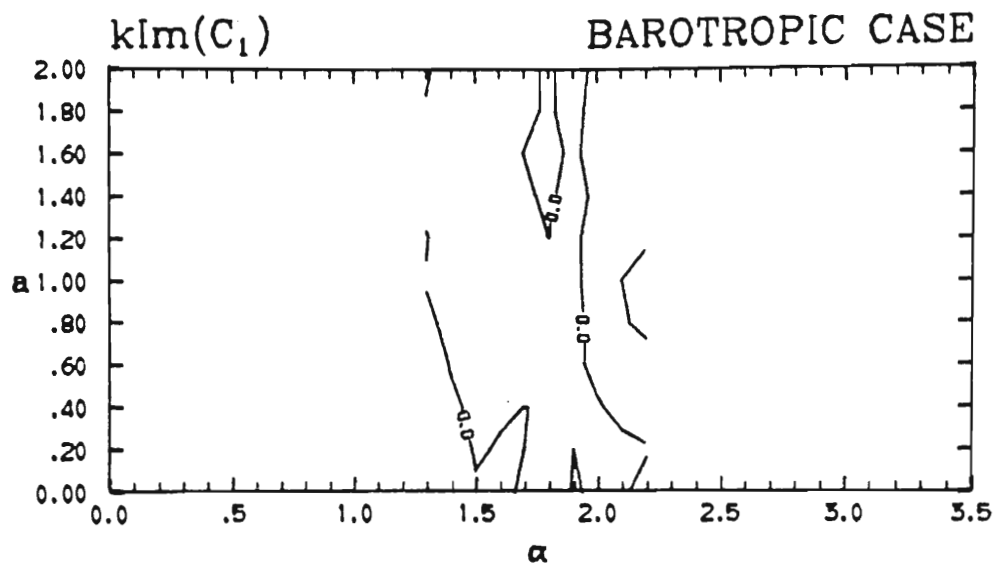


Fig. I-1d. Same as Fig. I-1a except for the Barotropic case.

Fig. I-1d. Same as Fig. I-1a except for the Barotropic case.

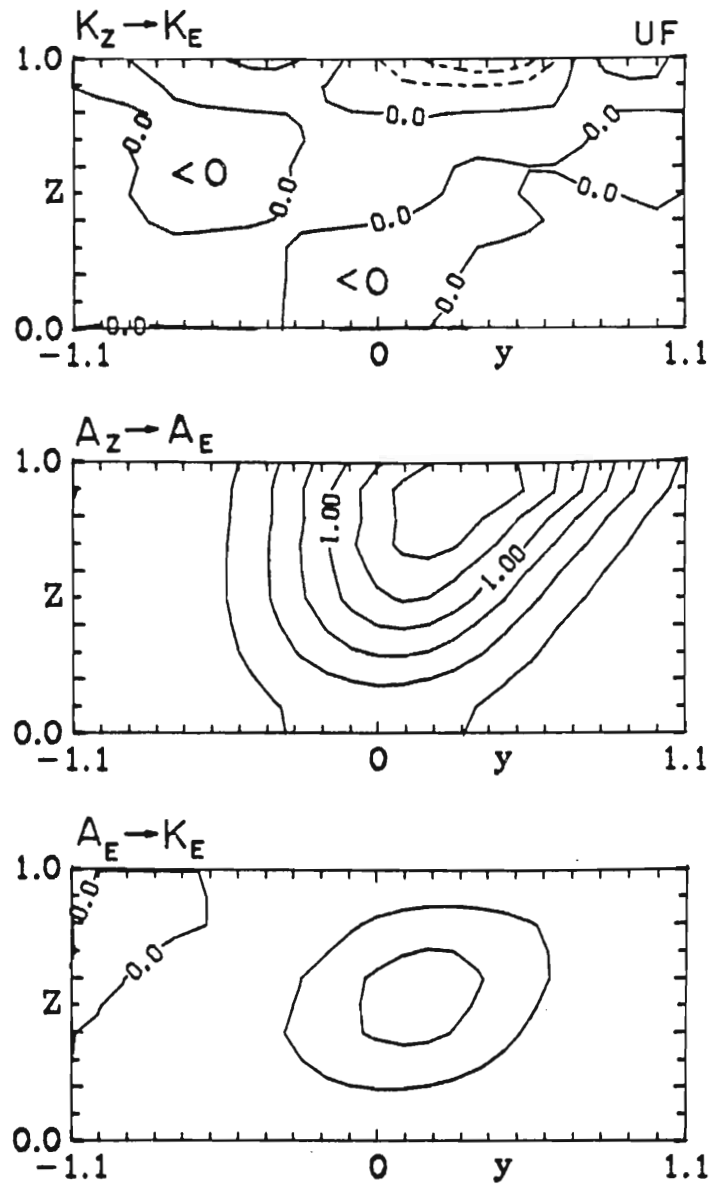


Fig. I-2a. Same as Fig. 23 except for the Upper Front case.

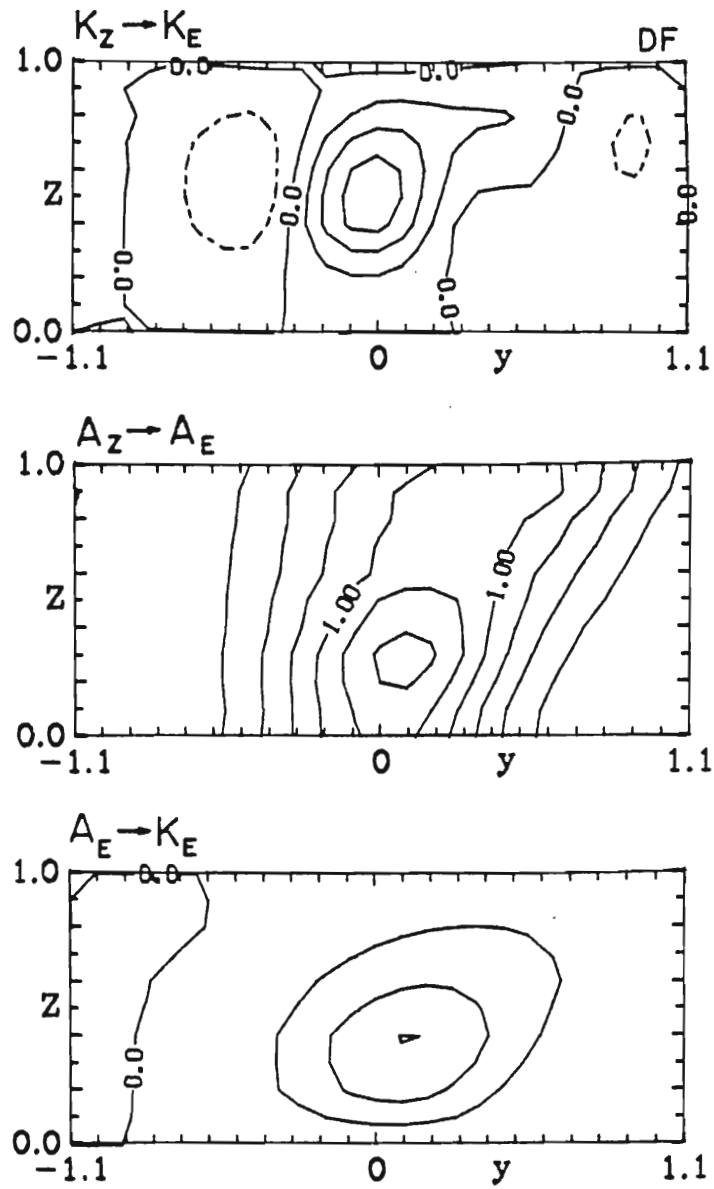


Fig. I-2b. Same as Fig. 23 except for the Deep Front case.

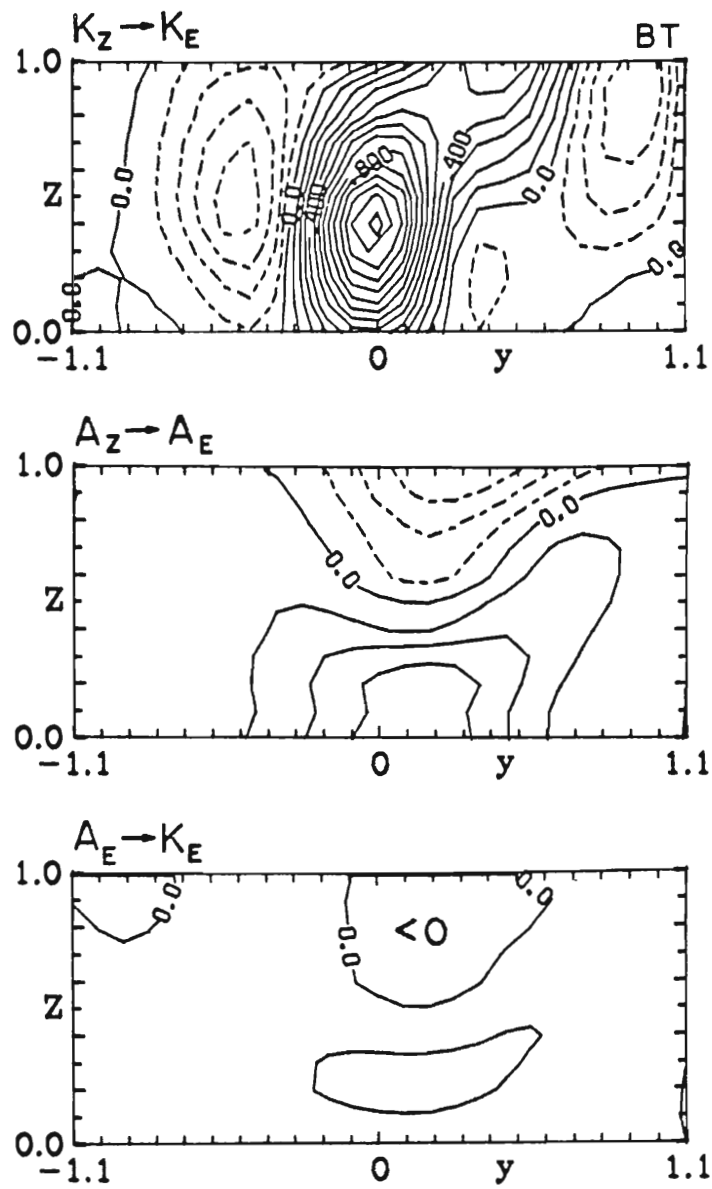


Fig. I-2c. Same as Fig. 23 except for the Barotropic case.

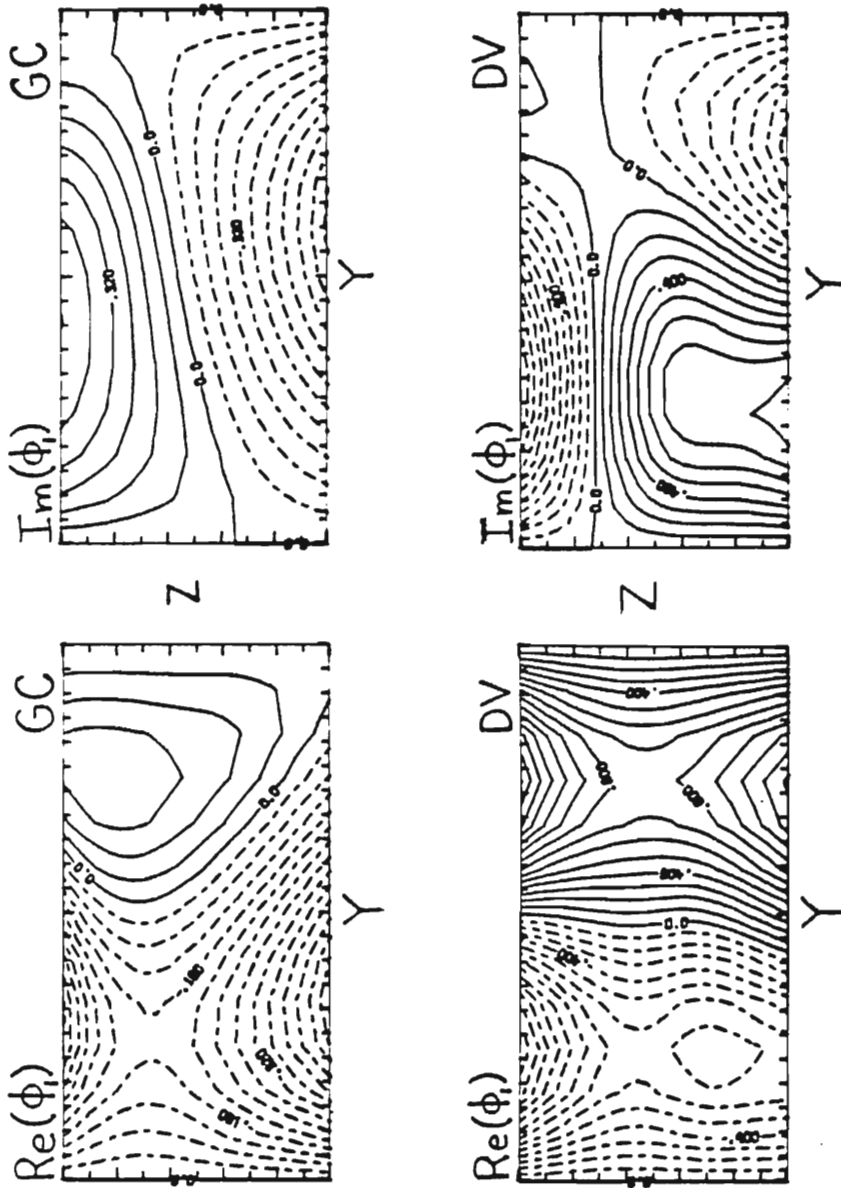


Fig. I-3a. The real part (left) and imaginary part (right) of ϕ_1 calculated for the ageostrophic terms in (27) labeled GC (upper pair) and DV (lower pair). The contour intervals in the upper pair of plots are .04 (left) and .08 (right). The contour interval in the lower pair is .1. Dashed contours indicate negative values.

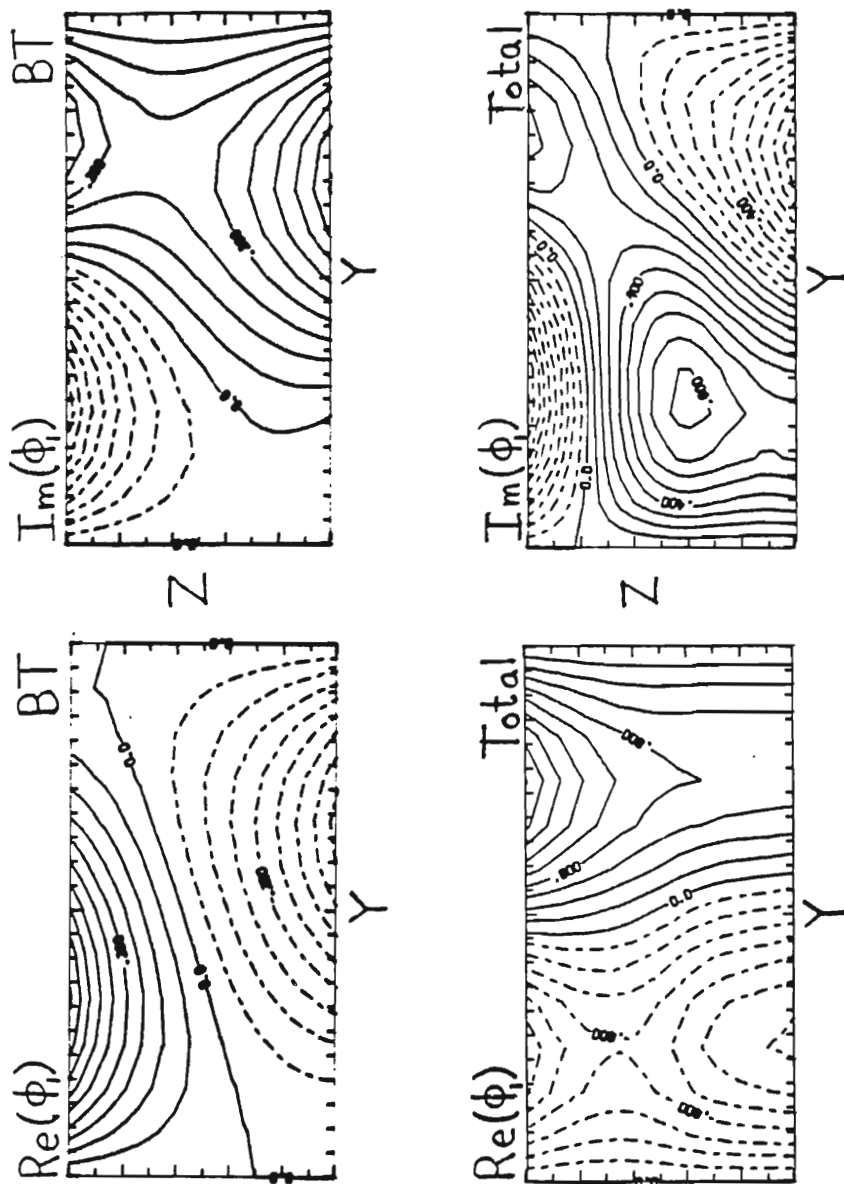
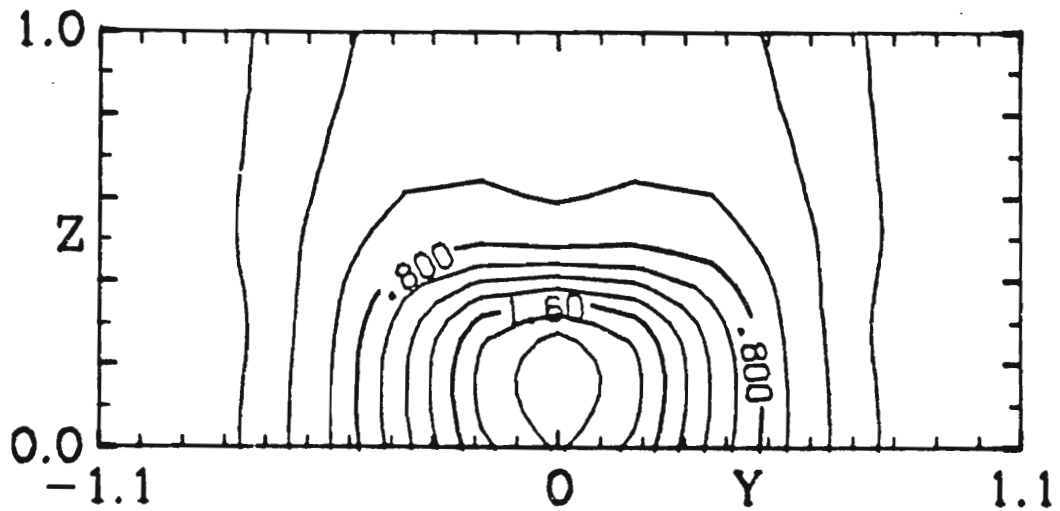


Fig. I-3b. Similar to Fig. I-3a except for the BT terms in (28) (upper pair) and the total ageostrophic ϕ_1 (lower pair). The contour interval for the upper pair of plots is .07, that for the lower pair is .1.

POLEWARD HEAT FLUX



MOMENTUM FLUX

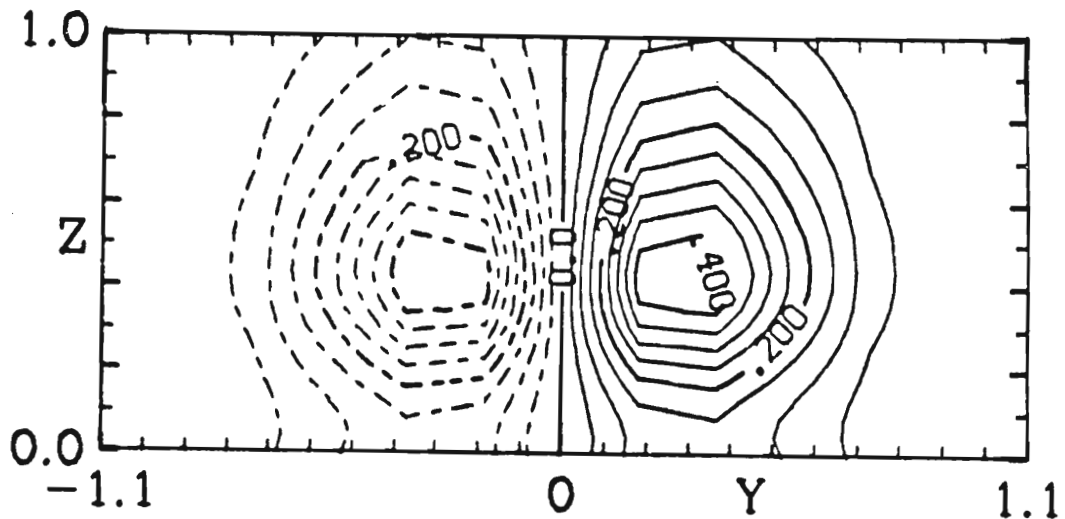
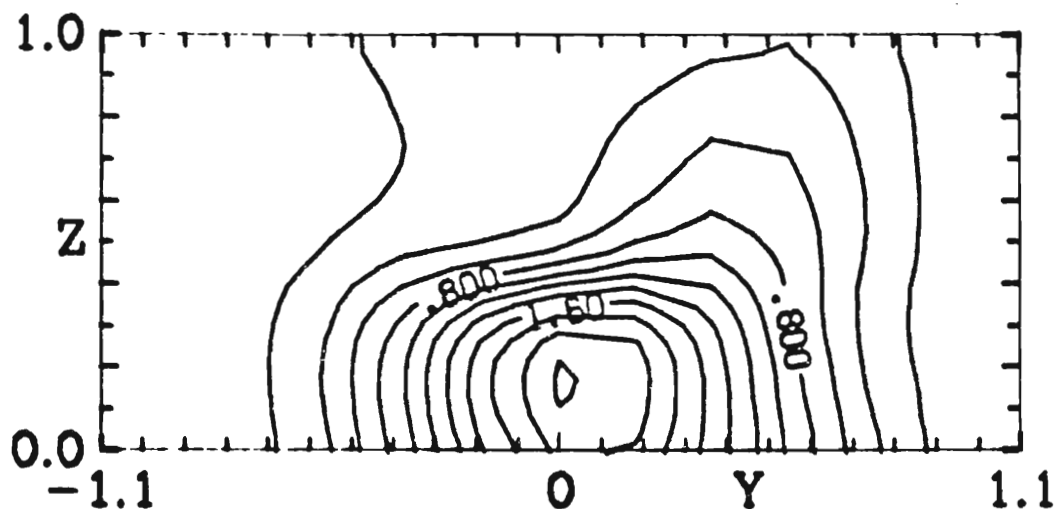


Fig. I-4a Quasi-geostrophic poleward heat flux and momentum flux for the Surface Front case, $\alpha = 2.0$, $\underline{a} = 1.6$ and $\beta = 1$. The contour intervals are .2 in the upper diagram and .05 in the lower.

POLEWARD HEAT FLUX



MOMENTUM FLUX

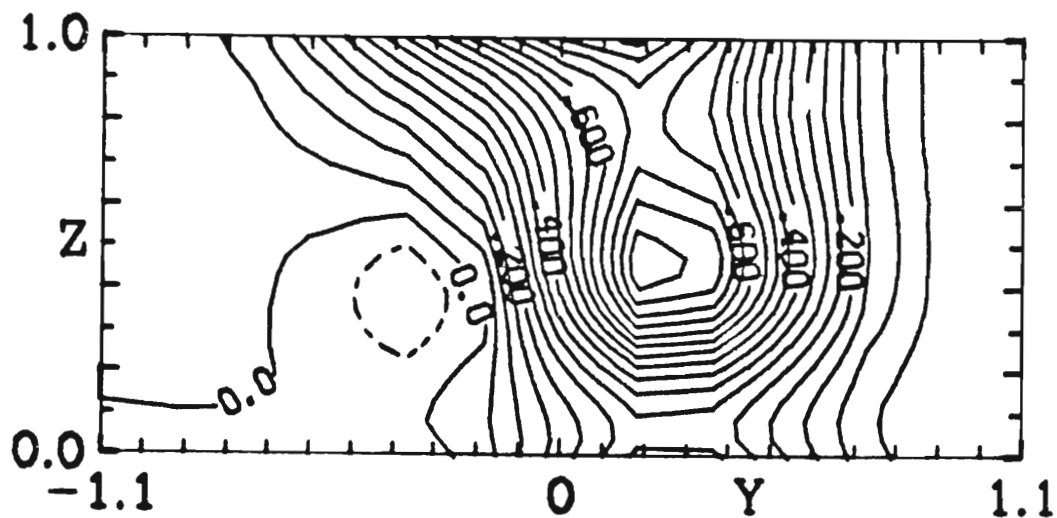


Fig. I-4b Same as Fig. I-4a, except that the contributions by the ageostrophic terms have been included. Same respective contour intervals as in Fig. I-4a.

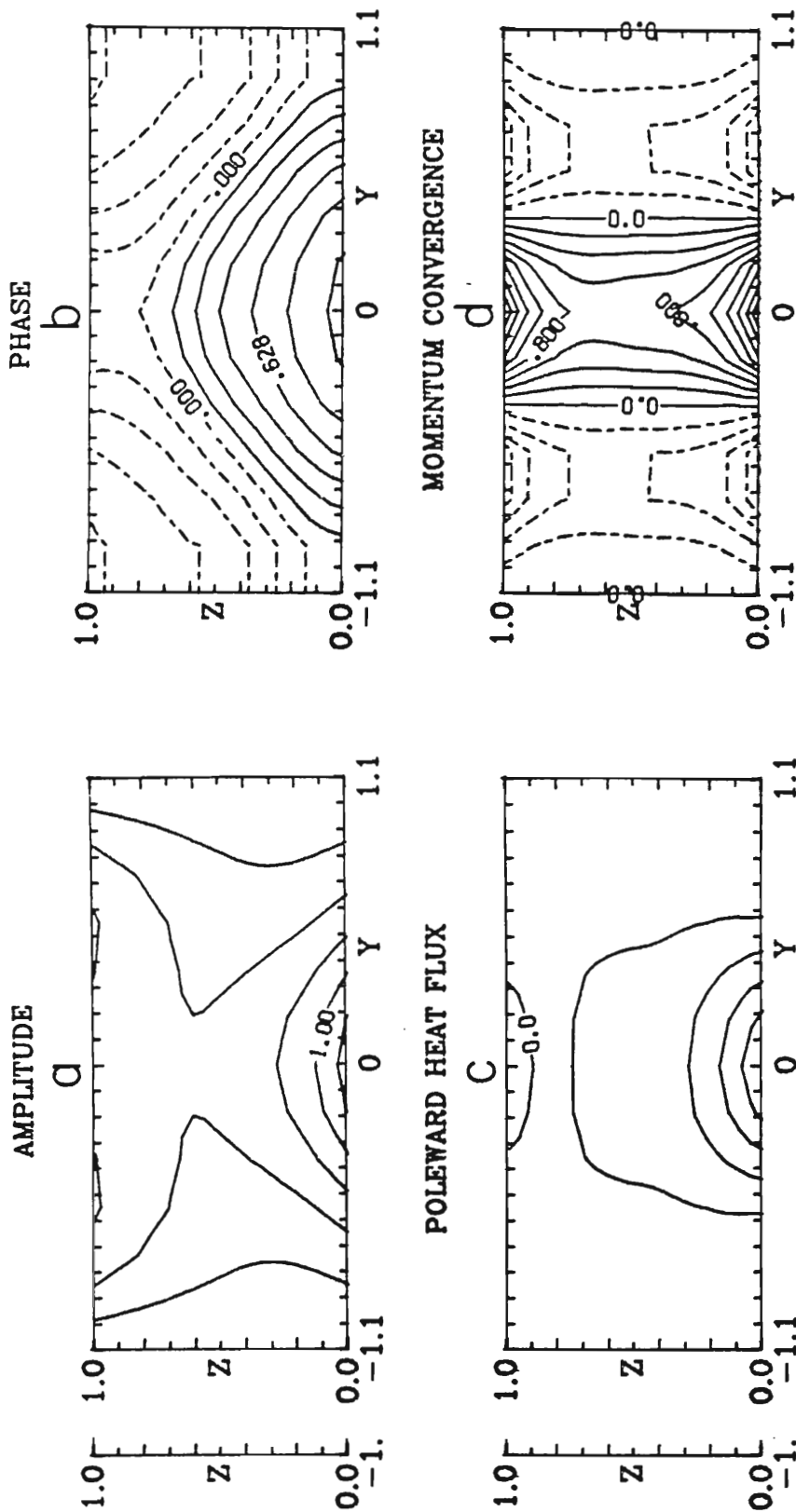
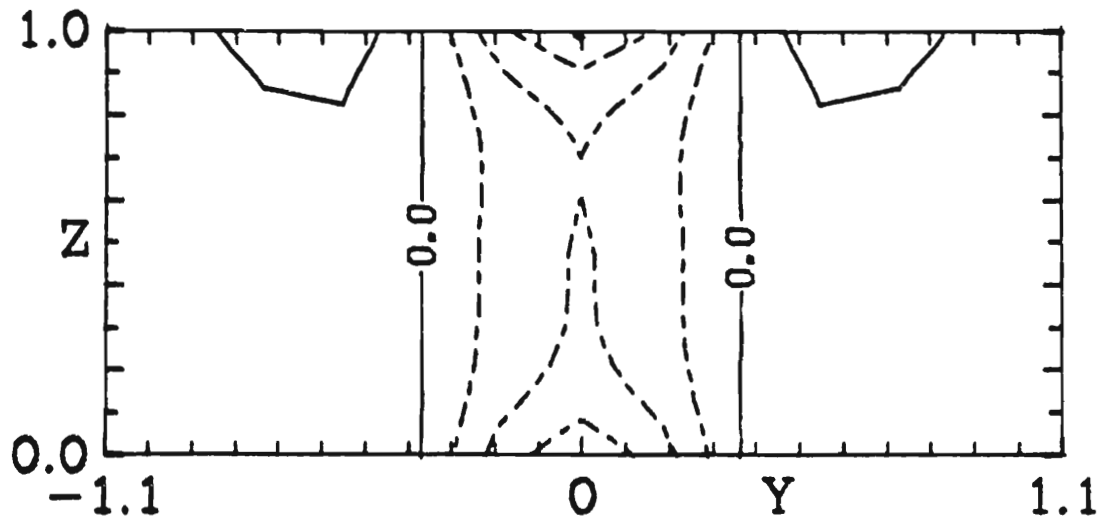


Fig. I-5a I-5a This figure is similar in format to Fig. 5 in McIntyre (1970). The agreement is good, despite
c differences in the model formulations. The contour intervals are .25 in a, .05 π in b, and .2
i in c and d.

BAROTROPIC CONVERSION



BAROCLINIC CONVERSION

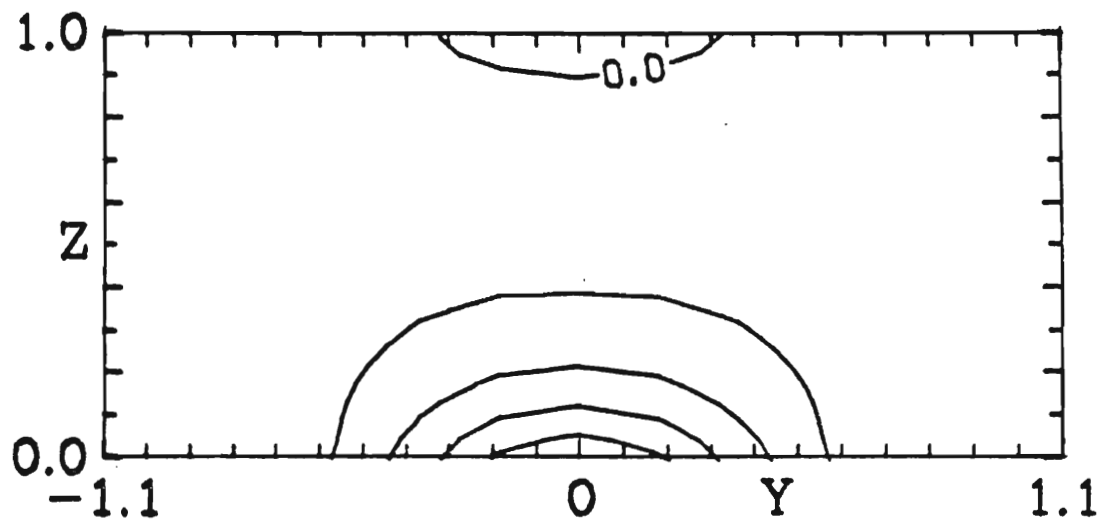


Fig. I-5b The corresponding baroclinic ($\overline{A_z \rightarrow A_z}$) and barotropic

Fig. I-5b The corresponding baroclinic ($\overline{A_z \rightarrow A_z}$) and barotropic ($\overline{K_z \rightarrow K_z}$) energy conversions for the solution presented in Fig. I-5a. The contour interval is .25.

REFERENCES

- Arakawa, A., 1962: Non-geostrophic effects in the baroclinic prognostic equations. Proc. Intern. Symp. Numerical Weather Prediction, Tokyo, 1960, Meteor. Soc. Japan, 161-175.
- Arnason, G., 1963: The stability of nongeostrophic perturbations in a baroclinic zonal flow. Tellus, 15, 205-229.
- Bretherton, F. P., 1966a: Critical layer instability in baroclinic flows. Quart. J. Roy. Met. Soc., 92, 325-334.
- _____, 1966b: Baroclinic instability and the short wavelength cut-off in terms of potential vorticity. Quart. J. Roy. Met. Soc., 92, 335-345.
- Brown, J. A., 1969a: A numerical investigation of hydrodynamic instability and energy conversions in the quasi-geostrophic atmosphere: Part I. J. Atmos. Sci., 26, 352-365.
- _____, 1969b: A numerical investigation of hydrodynamic instability and energy conversions in the quasi-geostrophic atmosphere: Part II. J. Atmos. Sci., 26, 366-375.
- Charney, J. G., 1947: The dynamics of long waves in a baroclinic westerly current. J. Meteor., 4, 135-162.
- _____, 1974: Planetary fluid dynamics. In Dynamic Meteorology, P. Morel, ed., Reidel, Boston, 99-351. (see section 9)
- _____ and M. E. Stern, 1962: On the stability of internal baroclinic jets in a rotating atmosphere. J. Atmos. Sci., 19, 154-172.
- _____ and M. E. Stern, 1962: On the stability of internal baroclinic jets in a rotating atmosphere. J. Atmos. Sci., 19, 154-172.

- Derome, J., and C. L. Dolph, 1970: Three-dimensional non-geostrophic disturbances in a baroclinic zonal flow. Geo. Fluid Dyn., 1, 91-122.
- Drazin, P. G., 1970: Non-linear baroclinic instability of a continuous zonal flow. Quart. J. Roy. Met. Soc., 96, 667-676.
- _____, 1972: Non-linear baroclinic instability of a continuous zonal flow of viscous fluid. J. Fluid Mech., 55, 577-587.
- Eady, E. T., 1949: Long waves and cyclone waves. Tellus, 1, #3, 33-52.
- Fjørtoft, R., 1951: Stability properties of large-scale atmospheric disturbances. In Compendium of Meteorology, T. F. Malone, ed., American Meteorological Society, Boston, 454-463.
- Gent, P. R., 1975: Baroclinic instability of a slowly varying zonal flow: Part 2. J. Atmos. Sci., 32, 2094-2102.
- Green, J. S. A., 1960: A problem in baroclinic stability. Quart. J. Roy. Met. Soc., 86, 237-251.
- _____, 1970: Transfer properties of large-scale eddies and the general circulation of the atmosphere. Quart. J. Roy. Met. Soc., 96, 157-185.
- Held, I. M., 1975: Momentum transport by quasi-geostrophic eddies. J. Atmos. Sci., 32, 1444-1497.
- Hinkelmann, K., 1959: Ein numerisches experiment mit der primitiven gleichungen. In The Atmosphere and the Sea in Motion, B. Bolin, ed., Rockefeller Press, New York, 486-500.
- gleichungen. In The Atmosphere and the Sea in Motion, B. Bolin, ed., Rockefeller Press, New York, 486-500.

- Hollingsworth, A., 1975: Baroclinic instability of a simple flow on a sphere. Quart. J. Roy. Met. Soc., 101, 495-528.
- _____, A. J. Simmons, and B. J. Hoskins, 1976: The effect of spherical geometry on momentum transports in simple baroclinic flows. Quart. J. Roy. Met. Soc., 102, 901-911.
- Holton, J. R., 1972: An Introduction to Dynamic Meteorology, Academic Press, New York, 319 pp. (Chapter 10).
- Hoskins, B. J., 1975: The geostrophic momentum approximation and the semi-geostrophic equations. J. Atmos. Sci., 32, 233-242.
- _____, 1976: Baroclinic waves and frontogenesis, Part I: Introduction and Eady waves. Quart. J. Roy. Met. Soc., 102, 103-122.
- Johnson, D. R., 1970: The available potential energy of storms. J. Atmos. Sci., 27, 727-741.
- Kuo, H.-L., 1949: Dynamic instability of two-dimensional nondivergent flow in a barotropic atmosphere. J. Meteor., 6, 105-122.
- Lindzen, R.S., B. Farrell and K.-K. Tung, 1979: The concept of wave over-reflection and its application to baroclinic instability. Submitted to J. Atmos. Sci.
- Loesch, A.Z., 1974: Resonant interactions between unstable and neutral baroclinic waves: Part I. J. Atmos. Sci., 31, 1177-1201. Part II: 1202-1217.
- _____, and A. Domaracki, 1977: Dynamics of N resonantly interacting baroclinic waves. J. Atmos. Sci., 34, 22-35.
- Mak, M., 1977: On the nongeostrophic baroclinic instability problem. baroclinic waves. J. Atmos. Sci., 34, 22-35.
- Mak, M., 1977: On the nongeostrophic baroclinic instability problem. J. Atmos. Sci., 34, 991-1006.

- McIntyre, M. E., 1970: On the nonseparable baroclinic parallel flow instability problem. J. Fluid. Mech., 40, 273-306.
- Moura, A. D. and P. H. Stone, 1976: The effect of spherical geometry on baroclinic instability. J. Atmos. Sci., 33, 602-616.
- Newell, R. E., J. W. Kidson, D. G. Vincent and G. J. Boer, 1972: The General Circulation of the Tropical Atmosphere, Volume 1. M.I.T. Press, Cambridge, 258 pp. (Chapters 3 and 4.).
- Palmén, E. H. and C. W. Newton, 1969: Atmospheric Circulation Systems, Academic Press, New York, 603 pp. (Chapters 9 and 11).
- Pedlosky, J., 1964a: The stability of currents in the atmosphere and ocean: Part I. J. Atmos. Sci., 21, 201-219.
- _____, 1964b: The stability of currents in the atmosphere and ocean: Part II. J. Atmos. Sci., 21, 342-353.
- _____, 1965: On the stability of baroclinic flows as a functional of the velocity profile. J. Atmos. Sci., 22, 137-145.
- _____, 1970: Finite-amplitude baroclinic waves. J. Atmos. Sci., 27, 15-30.
- _____, 1971: Finite-amplitude baroclinic waves with small dissipation. J. Atmos. Sci., 28, 587-597.
- Phillips, N. A., 1951: A simple three-dimensional model for the study of large-scale extratropical flow patterns. J. Meteor., 8, 381-394.
- _____, 1964: An overlooked aspect of the baroclinic stability problem. Tellus, 16, 268-270.
- _____, 1964: An overlooked aspect of the baroclinic stability problem. Tellus, 16, 268-270.

- Rossby, C.-G. and Collaborators, 1939: Relation between variations in the intensity of the zonal circulation and the displacement of the semi-permanent centers of action. J. Marine Res., 2, 38-55.
- Saltzman, B. and C. M. Tang, 1972: Analytical study of the evolution of an amplifying baroclinic wave. J. Atmos. Sci., 29, 427-444.
- _____ and _____, 1974: Mid-tropospheric frontogenesis in an amplifying baroclinic wave. J. Atmos. Sci., 31, 835-839.
- _____ and _____, 1975: Analytical study of the evolution of an amplifying baroclinic wave: Part II, Vertical motions and transport properties. J. Atmos. Sci., 32, 243-259.
- Simmons, A. J., 1974: The meridional scale of baroclinic waves. J. Atmos. Sci., 31, 1515-1525.
- _____ and B. J. Hoskins, 1976: Baroclinic instability on the sphere: Normal modes of the primitive and quasi-geostrophic equations. J. Atmos. Sci., 33, 1454-1477.
- _____ and _____, 1977: Baroclinic instability on the sphere: solutions with a more realistic tropopause. J. Atmos. Sci., 34, 581-588.
- Simons, T. J., 1972: The nonlinear dynamics of cyclone waves. J. Atmos. Sci., 29, 38-52.
- Song, R. T., 1971: A numerical study of the three-dimensional structure and energetics of unstable disturbances in zonal currents: Part I. J. Atmos. Sci., 28, 549-564. Part II: 565-586.
- _____ and _____, 1971: A numerical study of the three-dimensional structure and energetics of unstable disturbances in zonal currents: Part I. J. Atmos. Sci., 28, 549-564. Part II: 565-586.
- Stone, P. H., 1966: On non-geostrophic baroclinic stability. J. Atmos. Sci., 23, 390-400.

- _____, 1969: The meridional structure of baroclinic waves. J. Atmos. Sci., 26, 376-389.
- _____, 1970: On non-geostrophic baroclinic stability: Part II. J. Atmos. Sci., 27, 721-726.
- _____, 1972: On non-geostrophic baroclinic stability: Part III, The momentum and heat transports. J. Atmos. Sci., 29, 419-426.
- Tokioka, T., 1970: Non-geostrophic and non-hydrostatic stability of a baroclinic fluid. J. Met. Soc. Japan, 48, 503-520.
- U.S. Committee on Extension to the Standard Atmosphere, 1976: U.S. Standard Atmosphere, 1976, U.S. Govt. Print. Off., Washington, D.C., 227 pp.